Peoples Democratic Republic of Algeria
وزارة التعليم العالي والبحث العلمي
Ministry of Higher Education and Scientific Research

University 20 Août 1955 - Skikda
Faculty of Technology
Department of Mechanics

جامعة 20 أوت 1955 - سكيكدة
كلية العلوم
قسم الميكانيك

Ref : D012126032D

Thesis

Presented to obtain a

Doctoral Degree (LMD) in Mechanics

Option: ***Renewable Energies***

Theme:

Hydrodynamic Flow of a Nanofluid in an Entropy-Optimized Porous Medium

Presented by: **Abderrahmane MEZAACHE**

Graduated on: September 13, 2026

In front of the jury:

Dr	Azzedine Bedjaoui	M.C.A	University 20 August 1955 - Skikda	President
Pr	Fateh Mebarek-Oudina	Professor	University 20 August 1955 - Skikda	Supervisor
Pr	Ould Lahoucine Cherif	Professor	University 08 May 1945 - Guelma	Examiner
Pr	Abderrezak Merabet	Professor	University Constantine 1 - Constantine	Examiner
Dr	Farid Berrahil	M.C.A	University Abdelhafid Boussouf - Mila	Examiner
Dr	Bachir Bouchehit	M.C.A	University 20 August 1955 - Skikda	Examiner

Academic Year: 2025/2026

Acknowledgements

I would like to express my sincere and deepest gratitude to my doctoral thesis supervisor, Prof. Fateh Mebarek-Oudina, University 20 August 1955 – Skikda, for his invaluable guidance, insightful advice, continuous support, and encouragement throughout my doctoral studies and the preparation of this thesis.

I am also deeply grateful to Dr. Azzedine Bedjaoui, Associate Professor (M.C.A), University 20 August 1955 – Skikda, and President of the thesis jury, for his careful examination of this work, as well as for his valuable comments and constructive suggestions.

My sincere thanks are extended to Prof. Ould Lahoucine Cherif, University 08 May 1945 – Guelma, for accepting to serve as an examiner of this thesis and for his time, careful evaluation, and valuable scientific comments.

I would also like to express my sincere appreciation to Prof. Abderrezak Merabet, University Constantine 1 – Constantine, for his participation as an examiner and for his careful assessment of this work and constructive recommendations.

I am equally grateful to Dr. Farid Berrahil, Associate Professor (M.C.A), University Abdelhafid Boussouf – Mila, for accepting to examine this thesis and for his valuable remarks, suggestions, and contribution to the evaluation of this work.

My sincere thanks also go to Dr. Bachir Bouchehit, Associate Professor (M.C.A), University 20 August 1955 – Skikda, for his participation as an examiner, as well as for his careful reading of the thesis and constructive comments.

I would also like to express my appreciation to my friends and colleagues at the University 20 August 1955 – Skikda and University Constantine 1 – Constantine for their encouragement, collaboration, and supportive academic environment throughout my doctoral studies.

Finally, I am deeply grateful to all those who have contributed, directly or indirectly, to the completion of this thesis and to the successful accomplishment of my doctoral journey.

إهداء

إلى أخواتي وإلى أسرتي الكريمة، الذين كانوا على الدوام سندًا وعونًا لي في مختلف مراحل الحياة، في السراء والضراء.
.لقد كان دعمكم المتواصل ومحبتكم الصادقة مصدر قوة وإلهام، أسهما في تحقيق هذا الإنجاز

.أهدي هذا العمل إليكم جميعًا، تعبيرًا عن بالغ الامتنان وعظيم التقدير لما أحطتموني به من رعاية وصبر وتشجيع

.تقبلوا فائق احترامي واعتزازي، مع خالص الشكر ودوام المحبة

عبد الرحمان

Hydrodynamic Flow of a Nanofluid in an Entropy-Optimized Porous Medium

Abstract

Wavy walls, fins, porous materials, and nanofluids are widely employed as passive enhancement techniques to improve the efficiency and thermal performance of heat exchangers and heat sink systems. The present study investigates the thermal characteristics of nanofluid flow within a wavy channel partially filled with porous material. Two porous material structures commonly used in thermal engineering, packed granular media and porous foam, are numerically simulated and comparatively analyzed. The channel geometry consists of three sections, with a porous layer partially occupying the intermediate corrugated section. The physical model is based on a two-dimensional, laminar Darcy–Brinkman–Forchheimer formulation for nanofluid flow, coupled with a local thermal equilibrium (LTE) model for heat transfer that incorporates the viscous dissipation effect.

Numerical solutions are obtained using the ANSYS Fluent software, employing the finite volume method on appropriately generated computational meshes. The numerical results are validated against available theoretical, numerical, and experimental studies. Simulations are conducted for silver–water nanofluid flow in a wavy channel partially filled with a copper porous material. The coupled effects of the porous layer thickness (δ) and the Reynolds number (Re) on the Nusselt number, entropy generation, friction factor, and performance evaluation criterion are systematically analyzed.

The results demonstrate that both the porous insertion thickness and the porous material structure have a significant impact on the hydrodynamic and thermal performance of the channel. This influence is more pronounced for packed granular materials than for porous foam. For instance, at $Re = 400$ and within the porous thickness range of $\delta = 0.2–0.5$, the packed granular material yields increases of 43.04–134.64% in the Nusselt number and 97.68–437.06% in entropy generation compared with the clear channel. In contrast, the corresponding enhancements for metal foam are more moderate, reaching 36.19–94.53% for the Nusselt number and 70.83–197.90% for entropy generation.

Furthermore, as an extension of this work, a numerical investigation of heat transfer and entropy generation was carried out for a convergent–divergent plate channel heat exchanger. The results indicate that the shrinkage thickness parameter significantly enhances both heat transfer and entropy generation. At $Re = 500$, compared with a straight channel, a convergent–divergent channel with a shrinkage thickness parameter of 0.8 exhibits increases of 82.7% in the average Nusselt number and 212.6% in the average entropy generation.

Accordingly, substantial improvements in heat transfer performance in wavy porous channels can be achieved through the combined effects of the Reynolds number and porous layer thickness. This study therefore aims to provide a comprehensive reference for the thermal–hydraulic performance of straight and wavy porous-duct heat exchangers.

Keywords

Straight channel; wavy channel; heat exchanger; porous medium; entropy generation; thermal performance; convergent–divergent channel.

Écoulement Hydrodynamique d'un Nanofluide dans un Milieu Poreux Optimisé sur le Plan Entropique

Résumé

Les parois ondulées, les ailettes, les matériaux poreux et les nanofluides constituent des techniques passives largement utilisées pour améliorer l'efficacité et les performances des échangeurs de chaleur et des systèmes de dissipation thermique. La présente étude analyse les caractéristiques thermiques de l'écoulement d'un nanofluide à l'intérieur d'un canal ondulé partiellement rempli de matériau poreux. Deux structures distinctes de matériaux poreux, couramment employées en génie thermique, à savoir les matériaux poreux granulaires compactés et les matériaux poreux de type mousse, sont simulées et comparées. La géométrie du canal se compose de trois sections, dont la section intermédiaire est partiellement occupée par une couche poreuse. La modélisation physique repose sur une formulation bidimensionnelle laminaire de Darcy–Brinkman–Forchheimer pour l'écoulement du nanofluide, ainsi que sur le modèle d'équilibre thermique local pour l'équation de l'énergie, incluant le terme de dissipation visqueuse.

Les solutions numériques sont obtenues à l'aide du logiciel ANSYS Fluent, basé sur la méthode des volumes finis, avec des géométries discrétisées par des maillages adaptés. Les résultats numériques sont validés par comparaison avec des études théoriques, numériques et expérimentales issues de la littérature. Les simulations portent sur l'écoulement d'un nanofluide argent/eau dans un canal ondulé partiellement rempli d'un matériau poreux en cuivre. Les effets couplés de l'épaisseur de la couche poreuse (δ) et du nombre de Reynolds (Re) sur le nombre de Nusselt, la génération d'entropie, le facteur de frottement et le coefficient de performance sont analysés de manière détaillée.

Il est démontré que l'épaisseur de la couche poreuse insérée ainsi que la structure du matériau poreux influencent de manière significative les performances hydrodynamiques et thermiques du canal. Cet effet est plus prononcé lors de l'utilisation de matériaux granulaires compacts que de matériaux poreux de type mousse. À titre illustratif, pour $Re = 400$ et dans la plage $\delta \in [0{,}2–0{,}5]$, par comparaison avec un canal clair, l'utilisation d'un matériau granulaire compact entraîne une augmentation du nombre de Nusselt comprise entre 43,04 % et 134,64 %**,** tandis que la génération d'entropie augmente de 97,68 % à 437,06 %**.** En revanche, cette augmentation demeure moins marquée pour la mousse métallique, avec des gains du nombre de Nusselt variant de 36,19 % à 94,53 % et une augmentation de l'entropie comprise entre 70,83 % et 197,90 %**.**

D'autre part, en extension de ce travail, une exploration numérique du transfert de chaleur et de la génération d'entropie a été menée sur un échangeur de chaleur à plaques convergentes-divergentes. Il est démontré que le paramètre de contraction accroît de manière significative le transfert de chaleur ainsi que la génération d'entropie. Pour $Re = 500$, par comparaison avec un canal droit, un canal convergent-divergent présentant un paramètre de contraction égal à 0,8 enregistre une augmentation de 82,7% du nombre de Nusselt moyen et de 212,6% de l'entropie moyenne.

En conséquence, des améliorations notables du transfert de chaleur dans les canaux ondulés poreux peuvent être obtenues grâce à l'effet combiné du nombre de Reynolds de l'écoulement et de l'épaisseur de la couche poreuse. Par ailleurs, cette étude vise à fournir une référence approfondie sur les échangeurs de chaleur à conduits poreux, qu'ils soient droits ou ondulés.

Mots-clés :
Canal droit ; canal ondulé ; échangeur de chaleur ; milieu poreux ; génération d'entropie ; performance thermique ; canal convergent-divergent.

التدفق الهيدروديناميكي لسائل نانوي في وسط مسامي مُحسَّن إنتروبيًا

الملخص

تُستخدم الجدران المتموجة، والزعانف، والمواد المسامية، والسوائل النانوية بوصفها تقنيات سلبية فعّالة لتعزيز كفاءة وأداء الأنظمة الحرارية. تتناول هذه الدراسة الخصائص الحرارية لتدفق سائل نانوي داخل قناة متموجة مملوءة جزئيًا بمادة مسامية. وقد تمت محاكاة ومقارنة بنيتين مميزتين من المواد المسامية الشائعة في الهندسة الحرارية، هما المواد المسامية الحبيبية المعبأة والمواد المسامية من نوع الرغوة. تتكوّن هندسة القناة من ثلاثة أقسام، حيث يشغل القسم الأوسط من القناة المتموجة طبقة مسامية جزئية. وتعتمد النمذجة الفيزيائية على صيغة دارسي–برينكمان–فورشيمر ثنائية الأبعاد لوصف تدفق السائل النانوي، إضافةً إلى نموذج التوازن الحراري الموضعي لمعادلة الطاقة، مع تضمين تأثير التبديد اللزج.

تم الحصول على الحلول العددية باستخدام برنامج ANSYS Fluent المعتمد على طريقة الحجم المحدود، مع استخدام شبكات عددية ملائمة لتمثيل الأشكال الهندسية. وقد جرى التحقق من صحة النتائج العددية من خلال مقارنتها بدراسات نظرية وعددية وتجريبية منشورة. أُجريت المحاكاة لتدفق سائل نانوي فضة/ماء داخل قناة متموجة مملوءة جزئيًا بمادة مسامية من النحاس. وتم تحليل التأثيرات المقترنة لكل من سمك الطبقة المسامية (δ) وعدد رينولدز للتدفق (Re) على عدد نوسلت، وتوليد الإنتروبيا، وعامل الاحتكاك، ومعايير تقييم الأداء.

وقد أظهرت النتائج أن سمك الإدراج المسامي وبنية المادة المسامية يؤثران بصورة ملحوظة في الأداء الهيدروديناميكي والحراري للقناة المسامية، حيث يكون هذا التأثير أكثر وضوحًا عند استخدام المواد الحبيبية المعبأة مقارنة بالمواد المسامية من نوع الرغوة. وعلى سبيل المثال، عند $Re = 400$ وضمن المجال $\delta \in [0.2–0.5]$ ، وبالمقارنة مع القناة الخالية من المادة المسامية، تؤدي المادة الحبيبية المعبأة إلى زيادة في عدد نوسلت تتراوح بين 43.04 ٪و134.64٪، بينما ترتفع الإنتروبيا بنسبة تتراوح بين97.68 ٪ و 437.06٪ .في المقابل، تكون هذه الزيادات أقل حدة عند استخدام الرغوة المعدنية، إذ تتراوح زيادة عدد نوسلت بين 36.19 ٪ و94.53٪، وزيادة الإنتروبيا بين 70.83 ٪ و 197.90٪.

علاوةً على ذلك، وكامتدادٍ لهذا العمل، أُجريت دراسة عددية لانتقال الحرارة وتوليد الإنتروبيا في مبادل حراري ذي قنوات صفيحية متقاربة–متباعدة. وقد أظهرت النتائج أن معامل الانكماش يزيد بصورة ملحوظة من انتقال الحرارة وتوليد الإنتروبيا. فعند $Re = 500$، وبالمقارنة مع القناة المستقيمة، يحقق المبادل الحراري ذو القناة المتقاربة–المتباعدة ومعامل انكماش مقداره 0.8 زيادةً في متوسط عدد نوسلت بنسبة 82.7٪، وارتفاعًا في متوسط توليد الإنتروبيا بنسبة 212.6٪.

وبناءً على ذلك، يمكن تحقيق تحسينات ملحوظة في نقل الحرارة داخل القنوات المسامية المتموجة من خلال التأثير المشترك لعدد رينولدز للتدفق وسمك الطبقة المسامية. إضافةً إلى ذلك، يهدف هذا البحث إلى توفير مرجع معمّق حول المبادلات الحرارية ذات القنوات المسامية المستقيمة والمتموجة.

الكلمات المفتاحية

القناة المستقيمة؛ القناة المتموجة؛ المبادل الحراري؛ الوسط المسامي؛ توليد الإنتروبيا؛ الأداء الحراري؛ القناة المتقاربة–المتباعدة.

List of Figures

Chapter 1

Figure 1.1. Straight channel filled with porous media, illustrating a tube configuration with a double-layer porous medium [16].

Figure 1.2. Straight tube partially filled with porous media, illustrating a horizontal pipe with a porous insert [57].

Figure 1.3. Schematic of the clear (non-porous) wavy tube as studied in [69].

Figure 1.4. Schematic of the porous wavy-channel heat exchanger configuration [84].

Figure 1.5. Annular-tube heat exchanger filled with a bidisperse porous medium [30].

Figure 1.6. Figure 1.6. Wavy-wall geometries, showing a schematic of the combined model structure with different amplitudes [89].

Chapter 2

Figure 2.1 Schematic diagram of a sinusoidal wavy-plate channel filled with nanofluid (clear medium): physical configuration 1

Figure 2.2 Schematic diagram of a sinusoidal wavy-plate channel partially filled with a packed granular porous medium: physical configuration 2

Figure 2.3 Schematic diagram of a sinusoidal wavy-plate channel heat exchanger partially filled with a metal-foam porous medium: physical configuration 3

Figure 2.4 Examples of granular materials in nature and industry [134].

Figure 2.5 Metal foam structure representation showing cubic volumes used for CFD computations [138,139].

Chapter 3

Figure 3.1 Mesh generation in the clear region and near the walls ($\delta = 0$)

Figure 3.2 Mesh generation in the clear and porous domains, near the walls, and at the nanofluid–porous medium interfaces ($\delta = 0.4$)

Figure 3.3 Mesh independence study for the clear channel

Figure 3.4 Mesh independence study for the porous channel ($\delta = 0.4$)

Figure 3.5 Comparison of the present results with literature data for local Nusselt numbers: (a) wavy non-porous channel [62], $Re = 500$, $\alpha = 0.2$

Figure 3.6 Comparison of the present results with literature data for local Nusselt numbers: (b) wavy porous channel [79], $Re = 300$, $Da = 10^{-4}$, $\alpha = 0.15$, $\delta = 0.3$

Figure 3.7 Present numerical results of the dimensionless velocity distribution for different dimensionless porous medium thicknesses

Figure 3.8 Analytical solution of Torabi et al. [41] for the dimensionless velocity distribution at different dimensionless porous medium thicknesses

Figure 3.9 Comparison of the present numerical results with the experimental data of Jiang and Ren [22] for the local heat transfer coefficient: water, straight porous channel, $d_p = 0.428$ mm, $\varepsilon = 0.365$, $k_p = 75.35$ W·m^{-1}·K^{-1}

Chapter 4 (A)

Figure 4.1A. Effect of δ on velocity vectors at $Re = 500$ and $\varphi = 5\%$.

Figure 4.2A. Effect of δ on streamlines at $Re = 500$ and $\varphi = 5\%$.

Figure 4.3A. Effect of δ on velocity magnitude at $Re = 500$ and $\varphi = 5\%$.

Figure 4.4A. Effect of δ on isotherms at $Re = 500$ and $\varphi = 5\%$.

Figure 4.5A. Effect of porous insert thickness on local Nusselt number.

Figure 4.6A. Effect of porous insert thickness on local entropy generation.

Figure 4.7A. Effect of porous insert thickness on the average Nusselt number.

Figure 4.8A. Effect of porous insert thickness on the average entropy generation.

Figure 4.9A. Effect of Reynolds number on the average Nusselt number for clear and porous channels at $\delta = 0.4$ and $\varphi = 5\%$.

Figure 4.10A. Effect of Re on the rate of change of the average Nusselt number at φ = 5%.

Figure 4.11A. Effect of the Reynolds number on the average entropy of clear and porous channels ($\varphi = 5\%$).

Figure 4.12A. Effect of the Reynolds number on the rate of change of the average entropy, $\varphi = 5\%$.

Figure 4.13A. Effect of the porosity φ on the mean Nusselt number of a clear channel for $\delta = 0.4$ and $Re = 400$.

Figure 4.14A. Effect of the porosity φ on the mean Nusselt number of a porous channel for Re=400.

Figure 4.15A. Effect of the volume fraction on the mean entropy of a clear channel for $Re = 400$.

Figure 4.16A. Effect of the volume fraction on the mean entropy of a porous channel for $Re = 400$.

Chapter 4 (B)

Figure 4.1B. Velocity vectors for $Re = 400$ and $\varphi = 5\%$.

Figure 4.2B. Streamlines for $Re = 400$ and $\varphi = 5\%$.

Figure 4.3B. Effect of δ on the velocity magnitude for $Re = 400$ and $\varphi = 5\%$.

Figure 4.4B. Effect of δ on the isotherms for $Re = 400$ and $\varphi = 5\%$.

Figure 4.5B. Effect of δ on the local Nusselt number for $Re = 400$.

Figure 4.6B. Effect of δ on the local entropy for $Re = 400$.

Figure 4.7B. Effect of δ on the average Nusselt number for $Re = 400$ and $\varphi = 5\%$.

Figure 4.8B. Effect of δ on the average entropy for $Re = 400$ and $\varphi = 5\%$.

Figure 4.9B. Effect of δ on the average friction factor for $Re = 400$ and $\varphi = 5\%$.

Figure 4.10B. Effect of the Reynolds number on the velocity magnitude.

Figure 4.11B. Effect of the Reynolds number on the isotherms.

Figure 4.12B. Effect of the Reynolds number on the average Nusselt number for $\delta = 0.5$ and $\varphi = 5\%$.

Figure 4.13B. Effect of the Reynolds number on the average entropy for $\delta = 0.5$ and $\varphi = 5\%$.

Figure 4.14B. Effect of the Reynolds number on the average friction factor for $\delta = 0.5$ and $\varphi = 5\%$.

Figure 4.15. Effect of the Reynolds number on the performance evaluation criteria.

Figure 4.16B. Effect of δ on the performance evaluation criteria.

Figure 4.17B. Effect of δ on the relative gap of the performance evaluation criteria.

Figure 4.18B. Effect of the Reynolds number on the relative gap of the performance evaluation criteria.

Chapter 4 (C)

Figure 4.1C Schematic of the studied convergent–divergent plate channel heat exchanger (Physical Configuration 4)

Figure 4.2C (a) Convergent–divergent heated section for different values of the shrinkage thickness parameter ($\delta_s = 0$, 0.2, and 0.4)

Figure 4.2C (b) Convergent–divergent heated section for different values of the shrinkage thickness parameter ($\delta_s = 0.6$, 0.8, and 1.0)

Figure 4.3C Effect of the shrinkage thickness parameter on velocity vectors at $Re = 400$

Figure 4.4C Effect of the shrinkage thickness parameter on streamlines at $Re = 400$

Figure 4.5C Effect of the shrinkage thickness parameter on velocity magnitude at Re = 400

Figure 4.6C Effect of the shrinkage thickness parameter on isotherms at Re = 400

Figure 4.7C Effect of the shrinkage thickness parameter on the local Nusselt number for different Reynolds numbers: (a) $Re = 200$, (b) $Re = 500$

Figure 4.8C Effect of the shrinkage thickness parameter on local entropy for different Reynolds numbers: (a) $Re = 200$, (b) $Re = 500$

Figure 4.9C Effect of the shrinkage thickness parameter on the average Nusselt number for different Reynolds numbers

Figure 4.10C Effect of the shrinkage thickness parameter on the average entropy for different Reynolds numbers

Figure 4.11C Effect of Reynolds number on the average Nusselt number for straight and convergent–divergent channels across different geometrical cases

Figure 4.12C Effect of Reynolds number on the rate of change of the average Nusselt number for different geometrical cases

Figure 4.13C Effect of Reynolds number on the average entropy for straight and convergent–divergent channels across different geometrical cases

Figure 4.14C Effect of Reynolds number on the rate of change of average entropy for different geometrical cases

List of Tables

Chapter 1

Table 1.1. Analytical solutions for straight ducts filled with a porous medium.

Table 1.2. Numerical solutions for straight ducts filled with a porous medium: single-fluid case.

Table 1.3. Numerical solutions for straight ducts filled with a porous medium: nanofluid and hybrid nanofluid cases.

Table 1.4. Analytical solutions for straight ducts partially filled with porous material.

Table 1.5. Numerical solutions for straight ducts partially filled with porous material (DPFPM): nanofluid case.

Table 1.6. Numerical solutions for straight ducts partially filled with porous material (DPFPM): single-fluid channel case.

Table 1.7. Summary of primary numerical studies on clear wavy ducts: single-fluid case.

Table 1.8. Summary of numerical studies on clear wavy ducts: nanofluid case.

Table 1.9. Summary of literature studies on porous wavy ducts.

Chapter 2

Table 2.1 Experimental Permeability Values of Foam Materials

Chapter 3

Table 3.1 Mean Nusselt number for different grid sizes

Chapter 4 (A)

Table 4.1A. Simulation data for the corrugated plate channel.

Table 4.2A. Effect of δ on $\Delta\overline{Nu}/\overline{Nu}$ (%) and $\Delta\bar{S}/\bar{S}$ (%), with $Re = 200$ and $\varphi = 5\%$; the clear PCC is used as reference.

Table 4.3A. Effect of Re on $\Delta\overline{Nu}/\overline{Nu}$ (%) and $\Delta\bar{S}/\bar{S}$ (%) for $\delta = 0.4$ and $\varphi = 5\%$, using the clear PCC channel as reference.

Table 4.4A. Effect of φ on $\Delta\overline{Nu}/\overline{Nu}$ (%) and $\Delta\bar{S}/\bar{S}$ (%) at $Re = 400$ for both porous and clear PCC channels.

Chapter 4 (B)

Table 4.1B. Characteristics of the wavy-channel heat exchanger used in numerical simulations

Table 4.2B. Physical properties of the materials used [50, 82]

Table 4.3B. Characteristics of the porous material used

Table 4.4B. Effect of δ on $\Delta\overline{Nu}/\overline{Nu}$, $\Delta\bar{S}/\bar{S}$, and $\Delta\bar{f}/\bar{f}$ for $Re = 400$, $\varphi = 5\%$, using the clear wavy channel as reference

Table 4.5B. Effect of Re on $\Delta\overline{Nu}/\overline{Nu}$, $\Delta\bar{S}/\bar{S}$, and $\Delta\bar{f}/\bar{f}$ for $\delta = 0.5$, $\varphi = 5\%$, using the clear wavy channel as reference

Table 4.6B. Effect of δ and Re on the PEC, using the clear wavy channel as reference

Chapter 4 (C)

Table 4.1C: Simulation data for the studied plate convergent–divergent channel heat exchanger

Table 4.2C: Effect of shrinkage thickness parameter on $\Delta\overline{Nu}/\overline{Nu}$ (%) for different Reynolds numbers, using straight channel as Reference

Table 4.3C: Effect of shrinkage thickness parameter on $\Delta\bar{S}/\bar{S}$ (%) for different Reynolds numbers, using straight channel as reference

Table 4.4C Effect of Reynolds number on $\Delta\overline{Nu}/\overline{Nu}$ (%) for different geometrical configurations, with the straight channel as the reference.

Table 4.5C Effect of Reynolds number on $\Delta\bar{S}/\bar{S}$ (%) for different geometrical cases, with the straight channel as the reference.

Contents

Acknowledgements i

إهداء ii

Abstract iii

Résumé iv

ملخص v

List of Figures vi

List of Tables xi

Contents xiii

Nomenclature xvi

General Introduction 1

Chapter 1: A literature Review of Wavy and Straight Duct Porous Heat Exchangers 5

1.1 Introduction 6

1.2 Porous straight ducts 6

1.2.1 Straight ducts filled with porous medium 6

1.2.1.1 Analytical solution 6

1.2.1.2 Numerical solution 8

1.2.2. Straight ducts partially filled with porous medium 10

1.2.2.1 Analytical solution 10

1.2.2.2 Numerical solution 11

1.3 Wavy ducts 14

1.3.1. Clear wavy ducts 14

I.3.2. Porous wavy ducts 16

1.4 Porous heat exchanger 18

1.5 Wavy wall configurations and parameters 19

1.6 Conclusion 21

Chapter 2: Physical Model and Mathematical Formulation 23

2.1 Introduction 24

2.2 Physical problem 24

2.3 Mathematical formulation 26

2.3.1 Conservation equations 26

2.3.2 Boundary conditions 28

2.3.3 Physical properties 29
2.3.4 Physical parameters 30
2.3.4.1 Entropy 30
2.3.4.2 Nusselt number 30
2.3.4.3 Performance evaluation creteria 31
2.4 Porous medium coefficients 31
2.4.1 Packed granular porous medium 31
2.4.2 Foam porous medium 33
2.4.2.1 Experimental evaluation of permeability 34
2.4.2.2 Evaluation from correlations 35
2.4.2.2.1 Modified Ergun correlation 35
2.4.2.2.2 Calmidi correlation 35
2.4.2.2.3 Theoretical models for the evaluation of K 36
2.5 Conclusion 36
Chapter 3: Numerical Solution and Validations 37
3.1 Introduction 38
3.2 Numerical procedure of solving 38
3.3 Mesh generation 38
3.4 Numerical solution-Mesh independency 39
3.5 Numerical validations 41
3.6 Conclusion 45
Chapter 4(A): Heat Transfer in a Wavy Channel–Porous Packed Granular Medium 46
4.1A Introduction 47
4.2A Effect of porous layer thickness on velocity vectors and streamlines 47
4.3A Effect of porous layer thickness on velocity magnitude and isotherms 49
4.4A Effect of porous layer thickness on Nu and S 51
4.5A Effect of Reynolds number on $\overline{Nu}$ and $\bar{S}$ 54
4.6A Effect of nanoparticle volume fraction on $\overline{Nu}$ and $\bar{S}$ 56
4.7A Conclusion 59
Chapter 4(B): Heat Transfer in a Wavy Channel–Porous Metal Foam 60
4.1B Introduction 61
4.2B Effect of porous layer thickness on velocity vectors and streamlines 62
4.3B Effect of porous layer thickness on velocity magnitude and isotherms 64

4.4B Porous layer thickness impact on Nusselt number and entropy 65
4.5B Effect of Reynolds number on velocity magnitude and isotherms 70
4.6B Impact of Reynolds number on $\overline{Nu}$, $\bar{S}$, and $\bar{f}$ 76
4.7B Effect of porous layer thickness and Reynolds number on the PEC 76
4.8B Conclusion 82
Chapter 4(C) : Heat Tansfer in a Wavy Channel–Convergent-Divergent Channel 84
4.1C Introduction 85
4.2C Physical model of convergent-divergent channel heat exchanger 85
4.3C Simulated geometric cases for convergent-divergent channel 86
4.4C Effect of shrinkage thickness parameter on velocity vectors and streamlines 89
4.5C Effect of shrinkage thickness parameter on velocity magnitude and isotherms 90
4.6C Effect of shrinkage thickness parameter on local Nusselt number and entropy 90
4.7C Effect of shrinkage thickness parameter on average Nusselt number and entropy 96
4.8C Effect of Reynolds number on average Nusselt number and entropy 99
4.9C Conclusion 104
General Conclusion 105
References 112

Nomenclature

Latin characters

A	wave amplitude (m)
b	wavelength (m)
c	specific thermal capacity ($J.kg^{-1}.K^{-1}$)
C_F	Forchheimer coefficient (-)
C_2	inertial coefficient (m^{-1})
d	particle diameter of porous medium (m)
D	channel hydraulic diameter (m)
d_c	width of cubic representative cell (m)
d_f	fiber diameter (m)
D_p	cross-sectional pore size (m)
d_{po}	pore diameter (m)
f	friction factor (-)
h	local heat transfer coefficient ($W.m^{-2}.K^{-1}$)
H_c	height of the channel (m)
H_p	porous insert thickness (m)
H_t	height of the throat (m)
k	thermal conductivity ($W.m^{-1}.K^{-1}$)
K	permeability (m^2)
L	channel length (m)
Nu	Nusselt number (-)
p	pressure (Pa)
Pr	Prandtl number (-)
q	heat flux density ($W.m^{-2}$)
r	radial coordinate (m)
Re	Reynolds number (-)
S	volumetric entropy generation rate ($W \cdot m^{-3} \cdot K^{-1}$)
T	temperature (K)
u	longitudinal velocity component ($m.s^{-1}$)
v	transverse velocity component ($m.s^{-1}$)

$\vec{v}$	velocity vector ($m.s^{-1}$)
x	axial Cartesian coordinate (m)
x_1	inlet position of the wavy section (m)
x_2	exit position of the wavy section (m)
y	transverse Cartesian coordinate (m)

Greek symbols

∇	gradient operator
α	dimensionless wave amplitude (-)
φ	nanoparticles volume fraction (-)
Φ	particle's sphericity (-)
ϕ	viscous dissipation function ($W \cdot m^{-3}$)
ε	porosity (-)
σ	constant in the Ergun correlation (-)
λ	dimensionless wavelength (-)
λ'	dimensionless parameter in equation (2.5)
δ	dimensionless porous insert thickness (-)
δ_s	shrinkage thickness parameter (-)
ρ	mass density ($kg \cdot m^{-3}$)
μ	viscosity (Pa.s)
β	thermal expansion coefficient (K^{-1})
ω	pore density (PPI)
χ	tortuosity (-)

Subscripts

b	bottom wall
f	base fluid
h	heat
i	interface
in	inlet condition
np	nanoparticle
p	porous medium
s	straight channel

t	top wall
v	viscous
w	wall
1, 2	clear, porous region

Abbreviations

bvp4c	finite difference code
CPL	centered porous layer
CVCGM	control-volume collocated grid method
Da-Br-Fo	Darcy-Brinkman-Forchheimer
DPFPM	Duct partially filled porous material
FDF	fully developed flow
FDM	finite difference method
FEM	finite element method
FPM	filled with porous material
FVM	finite volume method
GM	granular material
HNF	hybrid nanofluid
HTF	Heat transfer fluid
HWC	horizontal wavy Channel
LMC	laminar mixed convection
LBM	Lattice Boltzmann method
LFC	laminar forced convection
LPM	local porous matrix
LTE	local thermal equilibrium
LTNE	local thermal non-equilibrium
MCHS	microchannel heat sink
MHD	magnetohydrodynamic
MSBNF	molten salt-based nanofluid
NF	nanofluid
PEC	performance evaluation criteria
PFPM	partially filled with porous material
PLAW	porous layer attached to the wall

PM	porous medium
PRAW	porous ribs attached to the wall
PSPAW	porous square pillars attached to the wall
PPI	pores per inch
RKM	Runge-Kutta method
RWC	radial wavy channel
SADIM	spline alternating direction implicit method
MLPM	multi-layered porous media
TFC	turbulent forced convection
2PMM	two-phase mixture model
1PMM	one-phase mixture model
VVM	vorticity-velocity method

General Introduction

Heat exchangers play a crucial role in ensuring the thermal protection of industrial systems and production processes. Their applications span electronic cooling devices, solar collectors, thermal storage systems, chemical reactors, food processing, and HVAC systems. As such, heat exchangers are a key factor in assessing both the economic viability and energy efficiency of thermal systems [1–2].

Advances in industrial technology have driven the need for high-performance, highly efficient heat exchangers. Consequently, the performance and optimization of thermal systems have become critical concerns across numerous industrial applications [3–5], particularly in the context of microtube and microchannel heat exchangers, whose adoption is rapidly increasing [6–7].

Research aimed at optimizing heat transfer mechanisms within channels is of paramount importance, particularly with the advent of nanotechnology, which offers new opportunities to enhance the thermal properties of fluids. Heat transfer improvements can be achieved through various passive techniques, including the addition of nanoparticles to the base fluid, the use of fins and twisted tapes [8–9], the incorporation of a porous medium within the channel [10], and the implementation of wavy wall configurations [11]. These passive methods can be applied individually or in combination. The integration of porous media, corrugated channel designs, and nanofluidic enhancements creates a sophisticated system with considerable potential for significantly improving heat transfer efficiency.

Research on passive techniques involving the insertion of porous media into channels can be classified into straight and wavy porous ducts. While porous straight channels, fully or partially filled, have been extensively investigated, studies on porous wavy channels remain limited and have focused primarily on specific porous insertions within the channel.

The literature indicates that wavy porous channels have received comparatively less attention. Several aspects of the physical problem remain insufficiently explored, particularly the channel geometry, the localization of the porous layer within the channel, and the nanofluid flow regime. Accurate modeling should account for both the physical and structural parameters of the porous medium. The structural properties are essential for evaluating the porous medium permeability, or the Darcy number, using appropriate correlations. Our review shows that two correlations based on structural properties are commonly employed: the Modified Ergun correlation and the Calmidi correlation, corresponding to packed granular porous media and porous foams, respectively. Moreover, unlike experimental studies, where permeability is a primary parameter to determine, most numerical

and analytical investigations select the permeability or Darcy number range without specifying the underlying porous medium structure.

Furthermore, to the best of the author's knowledge, no numerical studies have addressed the thermal and hydrodynamic performance of wavy channels partially or fully filled with a porous medium while explicitly considering the structural characteristics of foam materials, particularly pore diameter, fiber diameter, and pore density (PPI). The use of foam-specific structural parameters has so far been limited to studies on straight channels. Additionally, it is worth noting that structural parameters characterizing packed granular porous media, such as particle diameter and porous medium thickness, have been applied in some studies on wavy channels.

The objectives of this study are fourfold. First, a literature review is conducted on the assessment of permeability in porous media based on structural parameters. Second, the heat transfer characteristics of laminar nanofluid flow in a wavy channel heat exchanger are systematically investigated for different scenarios: a clear channel, a channel partially filled with packed granular porous material, and a channel partially filled with foam porous material. Third, the effects of porous layer thickness and flow Reynolds number on channel heat transfer, entropy generation, friction factor, and the performance evaluation criterion (PEC) are analyzed. Fourth, a comparative analysis is performed to evaluate the thermal efficiency of the system among the different channel configurations.

This research aims to advance the understanding of efficient heat exchange systems through detailed numerical simulations, with findings that could have significant implications for applications such as advanced cooling technologies and energy-efficient industrial operations.

The thesis is organized into six chapters:

Chapter 1 presents a literature review of porous heat exchangers in straight and wavy ducts. First, research works on heat transfer and flow in porous ducts are classified according to physical and geometrical parameters, physical modeling, and numerical approaches. This classification covers both straight and wavy porous ducts. Subsequently, an overview of porous exchanger applications is provided, and commonly used wavy wall configurations and their defining parameters are discussed.

Chapter 2 introduces a comprehensive physical model and mathematical formulation for analyzing heat transfer, fluid flow, and entropy generation in a porous wavy channel heat exchanger. The physical modeling is based on the Darcy–Brinkman–Forchheimer formulation

combined with a local thermal equilibrium (LTE) approach. The three physical cases under study, clear medium, packed granular medium, and metal foam medium, are presented. Additionally, the chapter investigates the method for evaluating porous medium coefficients based on the geometrical and physical parameters of the porous structure, specifically for packed granular and foam porous media.

Chapter 3 presents the numerical solutions and validation procedures. The study successfully investigates fluid flow and heat transfer in clear and porous channels **using** ANSYS Fluent 2020 R1**.** Structured meshes combined with second-order discretization schemes ensure high numerical accuracy, particularly near the channel walls and at the fluid–porous interfaces. The numerical methodology is validated against published numerical and experimental data, demonstrating strong agreement for both wavy and porous channel configurations.

Chapter 4 presents the results obtained in this study, covering three investigated physical cases.

Case A examines heat transfer in a wavy channel partially filled with a porous packed granular medium. The influence of porous medium thickness on the key hydrodynamic and thermal parameters governing nanofluid flow within the corrugated channel is analyzed. Six different corrugated-plate channel geometries are considered, corresponding to various values of the dimensionless porous medium thickness. The numerical simulations are conducted using water as the base fluid, CuO nanoparticles as the dispersed phase, and AISI 304 as the porous medium.

Case B investigates heat transfer in a wavy channel partially filled with a metal foam, with particular emphasis on the effects of porous layer thickness and Reynolds number on the key parameters governing nanofluid flow within the corrugated channel. The analyzed parameters include velocity vector contours, velocity magnitude, streamlines, isotherm contours, local and mean Nusselt numbers, entropy generation, relative Nusselt number and entropy, friction factor, and the performance evaluation criterion (PEC).

Case C explores heat transfer and entropy generation in a convergent–divergent plate heat exchanger channel. The influence of the shrinkage thickness parameter on the principal heat transfer characteristics of nanofluid flow within the convergent–divergent channel is examined. Five different geometrical configurations of the convergent–divergent channel are considered, corresponding to various values of the shrinkage thickness parameter.

CHAPTER 1:

A LITERATURE REVIEW OF WAVY AND STRAIGHT DUCT POROUS HEAT EXCHANGERS

1.1. Introduction

The present contribution focuses on the use of porous material insertions in straight and wavy channel heat exchangers to enhance thermal performance. The study addresses several key aspects: a comprehensive review and synthesis of recent theoretical, numerical, and experimental methodologies and findings; identification of the characteristic parameters governing heat transfer in porous channel heat exchangers; determination of the relevant geometrical parameters of wavy-wall heat exchangers; examination of porous medium structures; and specification of the adopted modeling approaches along with the simplifying assumptions employed.

The review is organized as follows. First, research works addressing heat transfer and fluid flow in porous ducts are classified according to physical and geometrical parameters, physical modeling, and numerical approaches. This classification covers porous straight ducts in Section 2 and porous wavy ducts in Section 3. An overview of the applications of porous heat exchangers is presented in Section 4. Section 5 introduces commonly used wavy-wall configurations and their associated parameters. Finally, conclusions are drawn, and recommendations for future research directions are discussed.

1.2. Porous Straight Ducts

Extensive investigations have been conducted on porous straight ducts, which may be either fully or partially filled with porous media. Analytical, numerical, and experimental studies have examined the characteristics of forced flow and heat transfer in such systems. These contributions are summarized below:

1.2.1. Straight Ducts Filled with Porous Medium

Figure 1.1. illustrates representative straight ducts filled with porous media that have been investigated in the literature. Table 1.1 summarizes the analytical approaches employed, whereas Tables 1.2 and 1.3 present the numerical solution methods.

1.2.1.1. Analytical Solution

Analytical solutions have been developed for fully developed laminar flow without considering the nanofluid approach, and are typically based on single-phase or two-phase mixture models. Both local thermal equilibrium (LTE) and local thermal non-equilibrium

(LTNE) approaches have been employed. The governing flow formulations include the Darcy (Da), Darcy–Brinkman (Da–Br), and Darcy–Brinkman–Forchheimer (Da–Br–Fo) models.

Table 1.1. Analytical solutions for straight ducts filled with a porous medium.

Reference	Geometry	Fluid	Energy equation	Flow formulation
Hashemi et al. [12]	micro-annulus	air	LTE	Da-Br
Makinde and Osalusi [13]	channel	-	-	Br
Ting et al. [14]	microchannel	water-Al_2O_3	LTNE	Da-Br
Lu et al. [15]	tube	-	LTNE	Da-Br
Yang et al. [16]	tube	-	LTNE	Da-Br
Bai et al. [17]	channel	air	LTE	Da-Br
Dehghan et al. [18]	tube	-	LTNE	Da-Br-Fo
Li et al. [19]	tube	air	LTNE	Da

Note: All studies assume laminar forced convection (LFC), fully developed flow (FDF), and do not consider nanofluid models.

Hashemi et al. [12] analyzed heat transfer in micro-annular ducts under various thermal boundary conditions. They derived analytical expressions for the temperature distribution and Nusselt number and examined the influence of the effective thermal conductivity of the porous medium. Makinde and Osalusi [13] investigated entropy generation in a channel subjected to a constant heat flux, showing that heat transfer irreversibility dominates over fluid-friction irreversibility. Moreover, viscous dissipation was found to have a negligible effect on entropy generation along the channel centerline. Ting et al. [14] studied nanofluid convection in porous microchannels, focusing on the thermal conductivity and viscosity of a water–Al_2O_3 nanofluid. The influence of the transverse synergy angle on flow characteristics was analyzed, and the results indicated that the Darcy number significantly affects convective performance. Lu et al. [15] examined heat transfer in a tube filled with metal foam and demonstrated that porosity and pore size are key parameters governing thermal performance. Yang et al. [16] investigated heat transfer in a tube filled with double-layer porous media. Using the LTNE model, they derived analytical expressions for velocity, temperature, and entropy generation, and showed that the Nusselt number exceeds that of a single-layer porous configuration. Bai et al. [17] analyzed heat transfer in channels filled with functionally graded metal foams and reported that porosity distribution strongly influences the thermal efficiency of the duct. Dehghan et al. [18] studied forced convection heat transfer in tube heat exchangers using the LTNE approach combined with the Darcy–Brinkman–Forchheimer model, highlighting the necessity of LTNE analysis under forced convection conditions. Finally, Li et al. [19] employed COMSOL Multiphysics to investigate forced convection heat transfer in a porous tube under the LTNE framework.

They derived analytical temperature solutions and identified the Péclet and Biot numbers as the dominant parameters affecting heat transfer.

1.2.1.2. Numerical Solution

Numerical solutions have been developed for the thermally and hydrodynamically developing flow region using either the local thermal equilibrium (LTE) or local thermal non-equilibrium (LTNE) approaches. The Darcy–Brinkman–Forchheimer formulation, combined with the finite volume method, is commonly employed. Studies have considered single-phase fluids, nanofluids, and hybrid nanofluids. Accordingly, the related references are classified into single-fluid studies (Table 1.2) and nanofluid-based studies (Table 1.3). For the latter group, the modeling approach may also incorporate two-phase mixture models.

Table 1.2. Numerical solutions for straight ducts filled with a porous medium: single-fluid case.

Reference	Geometry	Fluid	Fluid Flow	Porous energy equation	Numerical method
Hassan et al. [20]	Tube	air	TFC: k-ε model	LTE	FVM
Jiang and Lu [21]	Channel	water	TFC: k-ω model	LTE & LTNE	FVM
Jiang and Ren [22]	Channel	oil	LFC	LTNE	FDM
Peng et al. [23]	Tube	Water & air	LFC	LTE	FVM
Kamath et al. [24]	Channel	air	LMC	-	-

Note: Numerical & experimental studies [20, 23, 25]; fully developed flow (FDF) [23]; experimental work [24].

Jiang and Lu [21] numerically simulated fluid flow and heat transfer in a channel filled with a sintered porous plate using turbulent flow and LTNE models. Their results showed that the heat transfer coefficient increases with the mass flow rate, and the presence of LTNE effects was clearly identified. Jiang and Ren [22] numerically investigated the influence of oil thermophysical properties on laminar heat transfer in a porous channel under the LTNE framework. They reported that both the fluid temperature distribution and the heat transfer coefficient are strongly affected by the oil properties. Peng et al. [23] examined the influence of porous medium thermal conductivity on the thermal performance of a tube, considering different working fluids and porous materials. Their results indicated that neither the Nusselt number nor the performance evaluation criterion (PEC) exhibits a monotonic increase with thermal conductivity. Kamath et al. [24] experimentally investigated mixed convection in vertical channels incorporating metal foams and developed correlations for the Nusselt number and heat transfer enhancement ratio over a wide range of Richardson numbers (0.005–1032).

Table 1.3. Numerical solutions for straight ducts filled with a porous medium: nanofluid and hybrid nanofluid cases.

Reference	Geometry	Fluid	NF model	Fluid Flow	Porous momentum equation	Numerical method
Siavashi et al. [25]	Tube	Al_2O_3-water	2PMM	LFC	Da-Br-Fo	FVM
Aminian et al. [26]	Tube	Al_2O_3-CuO-water	2PMM	MHD-LFC	Da-Br-Fo	FVM
Alhajaj et al. [27]	Channel	Al_2O_3-water Al_2O_3-CuO-water	1PMM	LFC	Da-Br	FEM
Moghadasi et al. [28]	U-Ttube	Al_2O_3-CuO-water	2PMM	LFC	Da-Br-Fo	FVM

Note: Local thermal equilibrium (LTE), multi-layer porous medium (MLPM) [25], experimental work [27].

Siavashi et al. [25] focused on optimizing heat transfer enhancement in tube heat exchangers through the use of multilayer porous structures. Particle swarm optimization was employed to determine the optimal configuration of the porous layers. Aminian et al. [26] investigated magnetohydrodynamic (MHD) laminar forced convection of a CuO–Al_2O_3–water hybrid nanofluid in a porous tube heat exchanger. The Darcy–Brinkman–Forchheimer formulation combined with the two-phase mixture model was adopted, and the results demonstrated that increasing the Hartmann and Darcy numbers enhances the heat transfer coefficient. Moghadasi et al. [28] examined laminar heat transfer of an Al_2O_3–CuO–water hybrid nanofluid in a U-bend porous pipe, with particular emphasis on the effects of the Dean and Darcy numbers.

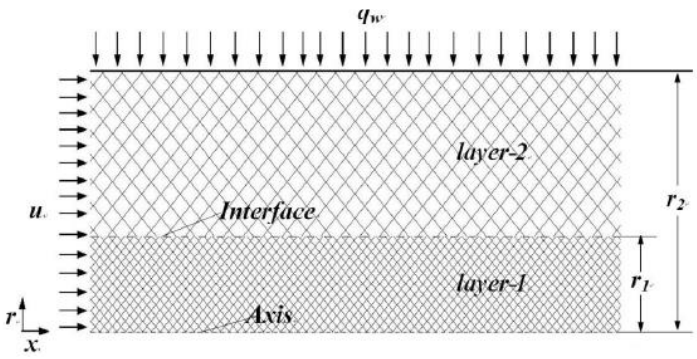


Figure 1.1. Straight channel filled with porous media, illustrating a tube configuration with a double-layer porous medium [16].

Their findings indicated that increasing the nanoparticle volume fraction improves the average Nusselt number, although at the expense of a higher pressure drop. Fiedler and Movahedi [29] investigated the application of A356 aluminum foam in shell-and-tube recuperators by casting the foam around a copper tube to enhance heat transfer between water streams at different temperatures. Their results demonstrated a substantial improvement in

thermal performance, attributed to the foam's large specific surface area and high effective thermal conductivity. Wang and Li [30] analytically examined convective heat transfer in an annular duct filled with a bidisperse porous medium using a two-velocity, two-temperature model under asymmetric heating conditions. Their findings indicate that bidispersity enhances heat transfer performance at lower effective thermal conductivity ratios compared with monodisperse porous media.

1.2.2. Straight Ducts Partially Filled with Porous Medium

The duct flow domain is modeled as two interacting regions: a clear fluid region and a porous medium region (Figure 1.2). Analytical studies have been conducted for laminar, fully developed flow under both LTE and LTNE conditions, employing the Darcy–Brinkman formulation. Various porous insertions, symmetrically arranged, were investigated, with particular emphasis on PLAW and CPL configurations (Table 1.4). Numerical solutions were primarily obtained for the developing flow region or across the entire duct domain (Tables 1.5 and 1.6).

1.2.2.1. Analytical Solution

Table 1.4. Analytical solutions for straight ducts partially filled with porous material.

Reference	Geometry	Fluid	Porous matrix	Porous Energy equation
Poulikakos et al. [31]	Channel & Tube	-	PMAW	LTE
Mohamad [32]	Channel & Tube	-	CPL	LTE
Morosuk [33]	Channel & Tube	-	CPL	LTE
Yang and Vafai [34]	Channel	-	CPL	LTNE
Yang et al. [35]	Tube	air	PLAW & CPL	LTNE
Mahmoudi et al. [36]	Channel		CPL	LTNE
Karimi et al. [37]	Channel	-	CPL	LTNE
Torabi et al. [38]	Channel	-	PLAW	LTNE
Torabi et al. [39]	Channel	-	PLAW	LTNE
Torabi et al. [40]	Channel	Cu-water	CPL	LTNE
Dickson et al. [41]	Channel	-	CPL	LTNE
Baig et al. [42]	Microchannel	Al_2O_3-water	CPL	LTNE

Note: Fully developed flow (FDF), laminar forced convection (LFC), Da–Br formulation, without considering nanofluid models.

Poulikakos and Kazmierczak [31] investigated the flow of heat transfer fluid (HTF) within PLAW channels under a constant wall heat flux. Two geometrical configurations, parallel plates and circular pipes, were analyzed. Their study demonstrated that the Nusselt number can be accurately predicted based on various governing parameters, with the critical thickness of the porous layer identified as a key factor influencing heat transfer performance. Mohamad

[32] examined heat transfer in a CPL tube, focusing on the effect of porous layer thickness across a Darcy number range of 10^{-6} to 10. The study revealed that the plug flow assumption ceases to be valid when the Darcy number exceeds 10^{-3}. Yang and Vafai [34] investigated the thermal behavior at the solid-fluid interface within a porous medium. Five different interfacial models were examined, and their validity was assessed. The theoretical temperature distribution for each model was derived, showing that the local thermal equilibrium (LTE) approach is sensitive to parameters such as the Biot number. Mahmoudi et al. [36] studied the enhancement of forced convective heat transfer in a CPL channel under local thermal non-equilibrium (LTNE) conditions. Two interface models for the porous layer–fluid interaction were evaluated. Their results indicate that the analytical expression for the Nusselt number is strongly influenced by both the chosen interface model and the Biot number. Karimi et al. [37] investigated heat transfer fluid (HTF) flow in a CPL channel, emphasizing LTNE conditions and the effects of internal heat generation. They highlighted the phenomenon of temperature gradient bifurcation, demonstrating its sensitivity to the intensity of the energy source. Torabi et al. [38–40] analyzed entropy generation in both PLAW and CPL channels under the LTNE framework. Analytical solutions were obtained for temperature fields, entropy generation rates, and Nusselt numbers. The bifurcation behavior of these quantities was examined with respect to porous layer thickness and the Biot number. Their study concluded that the LTNE approach offers a more accurate description of temperature distributions and entropy generation compared to LTE models. Baig et al. [42] simulated the performance evaluation criterion (PEC) of Al_2O_3–water nanofluid flow within a duct partially filled with porous material (DPFPM). They reported that optimal porous medium filling minimizes pressure drop while enhancing heat transfer.

1.2.2.2. Numerical Solution

The Darcy–Brinkman–Forchheimer (Da–Br–Fo) formulation is employed to model flow within a porous structure. Laminar, turbulent, and mixed convection flows are considered in the clear fluid domain. Additionally, both single-phase (1PMM) and two-phase (2PMM) nanofluid models are applied. To replicate realistic conditions, various symmetrical and non-symmetrical porous insertions are introduced within the ducts, including porous ribs attached to the wall (PRAW), porous square pillars attached to the wall (PSPAW), porous layers attached to the wall (PLAW), and centered porous layers (CPL).

Table 1.5. Numerical solutions for straight ducts partially filled with porous material (DPFPM): nanofluid case.

Reference	Geometry	Nanofluid	NF model	Fluid flow	Porous Matrix	Porous energy equation
Hajipour et al. [43]	channel	Al_2O_3–water	TPMM	LMC	PLAW	LTE
Torabi et al. [44]	channel	Al_2O_3–water	1PMM	LFC	PSPAW	LTE
Siavashi et al. [45]	Annuli	Al_2O_3–water	TPMM	LFC	PLAW	LTE
Siavashi [46]	Annuli	Al_2O_3–water	TPMM	LFC	PRAW	LTNE
Ying et al. [47]	tube	MSBNF	1PMM	k-ε model	PLAW & CPL	LTE

Note: Da–Br–Fo formulation; finite volume method (FVM); finite difference method (FDM) and experimental work [44]; Navier–Stokes formulation [45].

The finite volume method is widely used to solve nanofluid flow problems. For single-phase fluid flow, various numerical techniques have also been employed, including the finite difference method (FDM), the Runge–Kutta method (RKM), the vorticity–velocity method (VVM), the control-volume collocated grid method (CVCGM), the lattice Boltzmann method (LBM), and the finite difference solver `bvp4c`. The influence of nanofluid volume fraction, porous medium isotropy, porous matrix geometry, permeability, and Reynolds number on pressure drop, heat transfer coefficient, and performance evaluation criteria (PEC) has been systematically investigated.

Table 1.6. Numerical solutions for straight ducts partially filled with porous material (DPFPM): single-fluid channel case.

Reference	Geometry	Fluid	Fluid flow	Porous matrix	Porous momentum equation	Numerical method
Pavel et al. [48]	Tube	air	LFC	CPL	-	FDM
Huang et al. [49]	Tube	air	k-ε model	CPL	-	FDM
Jang et al. [50]	Channel	-	LFC	PLAW	Da-Br-Fo	RKM
Morosuk [33]	Channel Tube	-	LFC	CPL	-	FDM
Mohamed [32]	Channel Tube	-	LFC	CPL	-	FDM
Jen et al. [51]	Channel	-	LFC	PLAW	-	VVM
Nimvari [52]	Tube	-	k-ε model	PLAW & CPL	-	CVCGM
Shokouhmand et al. [53]	channel		LFC	PLAW & CPL	-	LBM
Mahmoudi et [54]	Tube	air, water	LFC	CPL	Da-Br-Fo	FVM
Al-Nimr and Alkam [55]	Annuli	-	LFC	PLAW	Da-Br-Fo	FDM
Mahdavi et al. [56]	Tube	-	LFC	PLAW & CPL	Da-Br-Fo	FVM
Teamah et al. [57]	Tube	-	LFC	CPL	Da-Br-Fo	FVM
Wang et al. [58]	μchannel	water	LFC	PRAW	LMDF	LBM
Iranmanesh et al. [59]	Annulus		LFC	PLAW	Da-Br	bvp4c method
Ali et al. [60]	Channel	water	k-ε model.	PLAW&PRAW	Da-Fo	FV

Note: Local thermal equilibrium (LTE) model; fully developed flow (FDF) formulation [50, 59]; experimental work [48, 49]; local thermal non-equilibrium (LTNE) model [54, 59, 60].

The main findings from the investigations summarized in Tables 5 and 6 can be outlined as follows:

- A significant enhancement in the heat transfer rate (up to 20%) was observed at a nanofluid volume fraction of 0.3, while the corresponding increase in pressure drop remained limited to only 5% [44].
- Both experimental and numerical studies indicate that incorporating porous inserts substantially improves thermal performance, although this is accompanied by an increase in pressure drop [49, 57].
- The thickness of the porous layer affects entropy generation and has a considerable influence on the Nusselt number [34, 51].
- Optimal porous layer thicknesses can maximize heat transfer in centrally configured channels while simultaneously minimizing pressure drop in boundary configurations [52, 55].
- The effect of thermal dispersion is particularly significant for small thickness ratios [51].
- The positioning of the porous insert has a substantial impact on thermal performance [53, 56].
- Optimizing foam configurations and parameters can markedly enhance heat dissipation rates in thermal systems [59–61].
- Heat transfer enhancement in a duct partially filled with porous material (DPFPM) under LTNE conditions was investigated, and the applicability of the LTE approach was discussed considering parameters such as the Darcy number (Da), porous layer thickness (d), porosity (ε), and conductivity ratio [54].
- For isotropic porous media, an in-line arrangement exhibits higher performance and achieves thermal equilibrium more rapidly than a staggered arrangement [45].
- In PRAW annuli, optimal configurations with ribs on the inner wall can achieve a performance number of up to 4, enhancing heat transfer efficiency by an order of magnitude [47].
- New correlations for the friction factor and Nusselt number were developed based on the relative parameters studied [58].

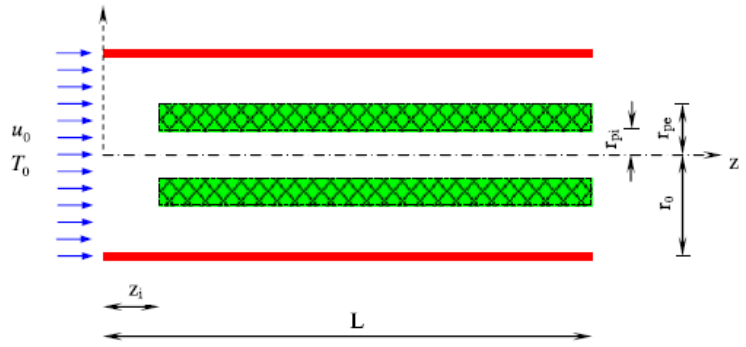


Figure 1.2. Straight tube partially filled with porous media, illustrating a horizontal pipe with a porous insert [57].

1.3. Wavy Ducts

1.3.1. Clear Wavy Ducts

Wavy surfaces enhance turbulence by promoting stronger fluid mixing, which in turn increases heat transfer rates. The introduction of wavy interfaces in heat exchangers has been shown to improve natural convection performance, particularly in nanofluid systems. Figure 1.3 presents schematic diagram of investigated non-porous (clear) wavy duct configurations. Tables 7 and 8 summarize the numerical models employed for single-fluid and nanofluid analyses, respectively.

Table 1.7. Summary of primary numerical studies on clear wavy ducts: single-fluid case.

Reference	Geometry	fluid	Fluid flow	Numerical method
Wang and Chen [62]	Channel	-	LFC	SADIM
Aslan et al. [63]	Channel	air	TFC: k-ε model	FVM
Ma et al (2016) [64]	Channel	air	LFC	FEM
Pati et al [65]	Channel	-	LFC	FVM
Zhang and Che [66]	Channel	air	TFC: k-ε model	FVM
Mohammed et al. [67]	Microchannel	water	LFC	FVM
Naphon and Kornkumjayrit [68]	Channel	air	TFC: k-ε model	FVM

Note: Based on experimental investigations [63, 64].

Table 1.8. Summary of numerical studies on clear wavy ducts: nanofluid case.

Reference	Geometry	Nanofluid	NF model	Fluid flow
Yang et al. [69]	Minitube	SiC-EG/H_2O	1PMM	k-ε model
Fares et al. [70]	Channel	Cu-water	2PMM	k-ε model
Dormohammadi et al. [71]	Channel	Cu-water	1PMM	LMC
Esfahani et al. [72]	Channel	Cu-water	1PMM	LFC
Valinataj-Bahnemiri et al. [73]	Channel	Al_2O_3-water	2PMM	LFC
Rostami et al. [74]	Microchannel	Cu-water & Al_2O_3-water	2PMM	LFC

Note: Finite volume method (FVM) used in the numerical solution.

Tables 7 and 8 summarize the principal investigations addressing the influence of fluid physical parameters and wavy duct geometrical characteristics on heat transfer, thermal performance, and overall efficiency. The physical parameters considered include the Reynolds number, Richardson number, Prandtl number, and nanoparticle volume fraction. The geometrical parameters encompass channel height, wave amplitude, wavelength, phase shift, wavelength ratio, and amplitude ratio. A variety of wavy configurations have been examined, with particular emphasis on sinusoidal, V-shaped, raccoon-shaped, and serpentine geometries, among others.

Overall, the reported findings indicate that:

- Corrugated surfaces enhance heat transfer by promoting disruption and destabilization of the thermal boundary layer [65], [68].
- Both the friction factor (f) and the Nusselt number (Nu) increase with increasing amplitude-to-wavelength ratios and Reynolds numbers [62].
- Wavy channels significantly improve heat transfer performance, albeit at the expense of a higher pressure drop [63], [67].
- Raccoon-shaped channels generally exhibit higher heat transfer rates than serpentine channels at larger wavelengths; however, the performance evaluation criterion (PEC) of serpentine channels often surpasses that of raccoon channels [65].
- The two-phase mixture model (2PMM) predicts higher Nusselt numbers compared to single-phase mixture models (1PMM) [75].
- Conventional single-phase models underestimate experimental observations, thereby motivating the adoption of two-phase mixture models to more accurately represent nanofluid dynamics [74].
- The maximum entropy generation rate decreases with increasing Richardson number. An optimal wave amplitude ratio of 0.2 was identified for minimizing entropy generation at specific wavelength ratios [71].
- Thermal entropy generation is dominant in the vicinity of the undulating walls, whereas viscous entropy generation intensifies with increasing dimensionless wave amplitude and Reynolds number [72].

- Increasing the nanoparticle volume fraction and Reynolds number significantly enhances the average Nusselt number; however, larger wavy-wall amplitudes have a detrimental effect on the performance evaluation criterion (PEC) [73].

- Various configurations of non-porous wavy ducts have been investigated, including double-pipe heat exchangers [76], three-tube systems equipped with sinusoidal wavy fins [77], and triplex wavy-channel latent heat storage heat exchangers (LHSHEs) [78]. These studies primarily focus on enhancing heat transfer performance and improving thermal energy storage capabilities for industrial heat-exchanger applications.

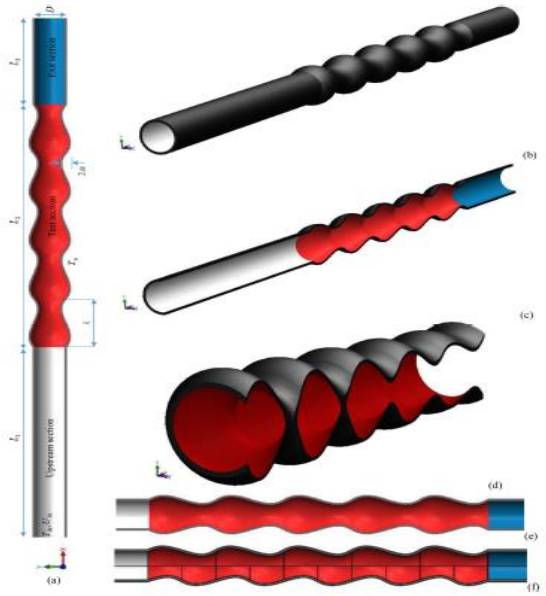


Figure 1.3. Schematic of the clear (non-porous) wavy tube as studied in [69].

1.3.2. Porous Wavy Ducts

Porous materials enhance effective thermal conductivity and increase the thermal capacity of the flow, thereby improving heat transfer in a wide range of thermal systems. The incorporation of porous media in wavy-tube heat exchangers has been shown to significantly enhance heat transfer efficiency, with optimal combinations of porosity and porous-layer thickness yielding superior overall performance. Figure 1.4. presents a Schematic of porous wavy channel heat exchanger, while the corresponding physical models are summarized in Table 1.9.

Table 1.9. Summary of literature studies on porous wavy ducts.

Author	Single fluid or nanofluid	Porous Matrix	Porous Momentum equation	Numerical method
Akbarzadeh and Maghrebi [79]	Water	CPL	Da-Br-Fo	FVM
Akbarzadeh et al. [80]	Cu-water	CPL	Da-Br-Fo	FVM
Aminian et al. [81]	Al_2O_3-water CuO-water	FPM	Da-Br-Fo	FVM
Nazari and Toghraie [82]	CuO-water	PFPM	NS	-
Ashorynejad and Zarghami [83]	Cu-water	PLAW	Br-Fo	LBM
Mezaache et al. [84]	Ag-water	CPL	Da-Br-Fo	FVM

Note: Channel geometry; single-phase porous medium (1PMM); laminar forced convection (LFC); local thermal equilibrium (LTE).

Akbarzadeh et al. [80] investigated the effects of nanofluids, porous inserts, and wavy walls on entropy generation, pressure drop, and heat transfer in a heat exchanger duct. Their study demonstrates that increasing either the thickness of porous inserts or the amplitude of wall waviness can enhance the thermal performance of wavy channels. Nazari and Toghraie [82] examined water–CuO nanofluid flow in a wavy channel incorporating porous material at the converging sections. Their findings indicate that higher Reynolds numbers amplify the temperature gradient and Nusselt number in the converging sections compared to the divergent regions of the channel.

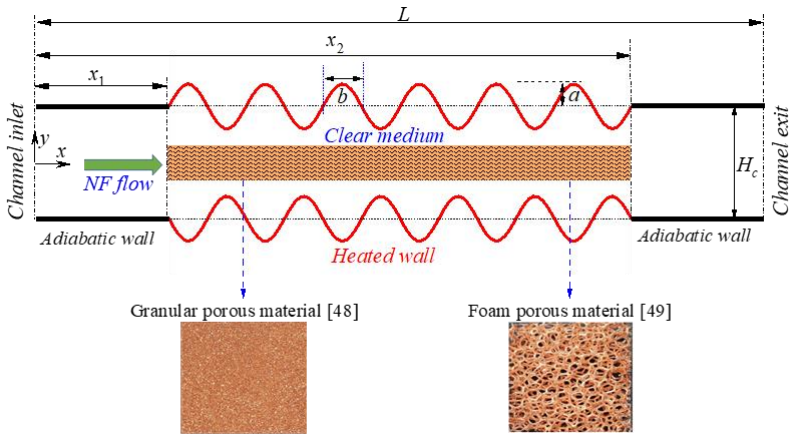


Figure 1.4. Schematic of the porous wavy-channel heat exchanger configuration [84].

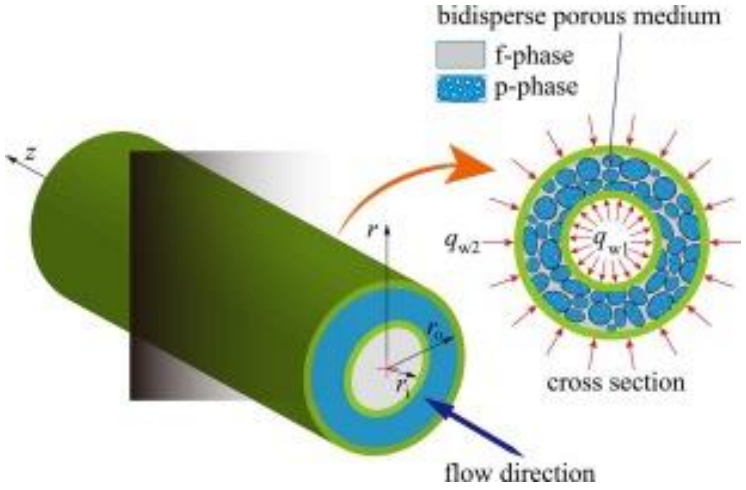
Ashorynejad and Zarghami [83] numerically investigated the influence of a uniform vertical magnetic field on Cu–water nanofluid flow in a partially porous wavy channel using the Lattice Boltzmann Method (LBM). Their results show that strong magnetic fields can confine the fluid within the porous layer, thereby affecting both flow behavior and heat transfer. Aminian et al. [81] studied heat transfer performance and entropy generation in a corrugated mini-channel filled with porous material. Their findings indicate that increasing the nanofluid volume

fraction leads to higher average Nusselt numbers and friction factors, while simultaneously reducing the performance evaluation criterion (PEC). Mezaache et al. [84] investigated the thermal behavior of nanofluids in a wavy duct partially filled with porous material, considering both packed granular and foam structures. They analyzed the effects of Reynolds number (Re) and dimensionless thickness (δ) on the performance evaluation criterion (PEC), including entropy generation, friction factors, and Nusselt number. The results reveal that packed granular materials significantly enhance thermal performance compared to foam structures, showing substantial increases in both entropy generation and Nusselt number at specific Reynolds numbers.

1.4. Porous Heat Exchanger

The combination of wavy walls and porous inserts has been employed in the design of advanced heat exchangers for both experimental studies and engineering applications, as illustrated in Figure 1.5. Konduru et al. [85] performed a numerical and experimental study on heat exchangers incorporating porous foam, specifically using Kelvin-cell foam to improve heat transfer at high temperatures. Their findings indicate that the foam structure effectively enhances temperature uniformity and promotes more efficient heat exchange between the airflow and the solid surfaces. Shang et al. [86] investigated the design and performance of porous-media heat exchangers used in cryogenic systems, which are essential for achieving sub-Kelvin temperatures. Their numerical model, incorporating LTNE and fluid flow equations, shows that the geometry of the porous media significantly affects both thermal and hydrodynamic performance, with optimal length-to-width and width-to-thickness ratios identified. Alhajaj et al. [27] investigated the thermal enhancement of water–Al_2O_3 nanofluid in porous channels. Their experiments showed that selecting an optimal nanofluid volume fraction can increase heat transfer by approximately 6%. A hybrid nanofluid containing both copper oxide and aluminium oxide provided even greater heat transfer enhancement, although this improvement was accompanied by a higher pressure drop. Delalic et al. [87] describe the design and analysis of a small heat exchanger unit incorporating porous media to improve energy efficiency and reduce CO_2 emissions from fossil fuel combustion. Their study indicates that using fuels with high heating values and enhancing latent heat can substantially increase thermal efficiency while lowering emissions. Hassan et al. [20] investigated forced convection heat transfer in a cylindrical channel filled with porous material that generates internal heat. Using both experimental and numerical approaches, they assessed pressure drop and heat

transfer performance, employing dry air as the working fluid and steel spheres to form the porous channel. Their results show that increasing the Reynolds number enhances the Nusselt number, while decreasing porosity further accelerates heat transfer rates.



(b)

Figure 1.5. Annular-tube heat exchanger filled with a bidisperse porous medium [30].

1.5. Wavy Wall Configurations and Parameters

Figure I.6 illustrates several relevant wavy wall geometries, while Figure 7 presents wavy surface configurations commonly used in duct heat exchangers. These configurations form the basis for many studies on enhanced heat transfer. For instance, Zhang and Defu [66] investigate the performance evaluation criterion (PEC) of cross-corrugated plates, considering a variety of corrugation profiles, including triangular, rectangular, sinusoidal, elliptical, and trapezoidal shapes. They employ a k-ε turbulence model to analyze incompressible, fully developed airflow, and identify two distinct flow patterns, L-shaped and Z-shaped, that significantly influence overall heat transfer performance. Ma et al. [64] investigate the pressure drop and heat transfer characteristics of cross-wavy surface channels, highlighting their potential applications in microturbine recuperators. Their numerical simulations indicate that channels with smaller diameters exhibit higher heat transfer coefficients at constant Reynolds numbers. Tian et al. [88] numerically examine the enhancement of heat transfer in wavy channels used in Battery Thermal Management Systems. They analyze the influence of wavy wall parameters, including wavelength, amplitude, and cross-sectional shape. Their findings demonstrate that channels with variable waviness achieve superior thermal efficiency compared to uniform

wavy channels. Qu et al. [89] investigate the performance evaluation criterion (PEC) of heat exchangers employing sinusoidal flow channels with varying amplitudes to enhance heat transfer efficiency while minimizing pressure drop. Seven distinct channel configurations, including a linear channel as a benchmark, are evaluated to identify the optimal arrangement for improved thermal performance and reduced flow resistance. The flow dynamics and heat transfer characteristics are analyzed numerically.

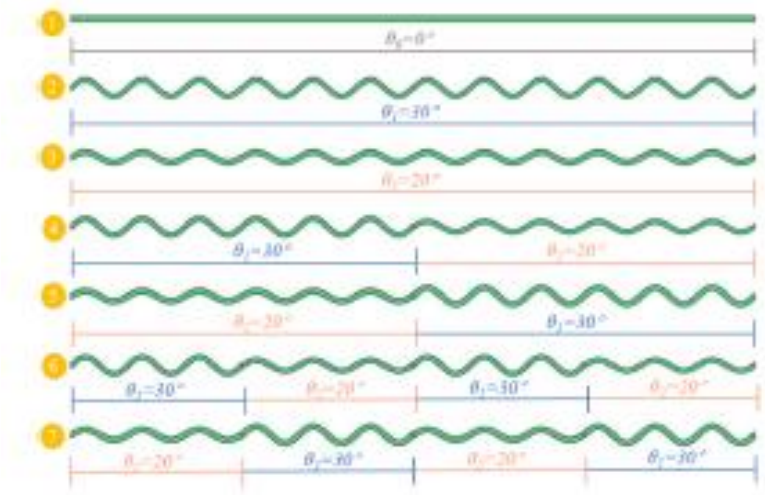


Figure 1.6. Wavy-wall geometries, showing a schematic of the combined model structure with different amplitudes [89].

Amiri et al. [90] investigated the thermal efficiency of a wavy microchannel heat sink (MCHS) using Ag–water nanofluid to enhance heat transfer. Their study revealed that sinusoidal channel designs outperform straight channels, delivering notable improvements in heat transfer rates; however, an excessive number of sinusoidal periods can reduce overall efficiency. Rush et al. [91] explored local heat transport and flow dynamics in sinusoidal wavy channels under laminar and transitional flow regimes. Through flow visualization techniques, they identified recirculation zones and clarified their role in enhancing heat transfer. Similarly, Said et al. [92] analyzed the effects of various wavy geometries, including zigzag, sinusoidal, and step-function profiles, on the solidification phase-change process within triplex-tube latent heat thermal energy storage (LHTES) systems for building heating. Their findings demonstrated that wavy geometries improve thermal exchange and reduce solidification time compared to conventional straight configurations.

1.6. Conclusion

Wavy walls, porous inserts, and nanofluids have attracted significant attention and found practical applications, particularly in heat sinks and thermal storage systems. These features are primarily employed as passive techniques to enhance the efficiency and overall performance of heat exchangers and heat sink systems. This review focused on wavy and straight duct heat exchangers, either fully or partially filled with porous media. The study has summarized and categorized the main analytical, numerical, and experimental contributions in this field. The classification presented across ten tables highlights the key physical parameters relevant to tube and channel heat exchangers and clearly illustrates the differences between existing models. The parameters considered include the interfacial heat transfer approach between the porous structure and the fluid, based on either LTNE or LTE models, and the flow modeling within the porous medium, using Darcy, Darcy–Brinkman, or Darcy–Brinkman–Forchheimer formulations. For nanofluids, either a one-phase or two-phase mixture model is employed.

Additionally, this review has:

- Analysed the dependence of geometrical, structural, and physical properties on the key characteristic parameters of porous media.
- Specified the characteristics of foam media and packed granular porous media.
- Identified the numerical methods commonly employed, including FVM, FEM, FDM, LBM, CVCGM, *bvp4c*, RKM, SADIM, and VVM.
- Presented commonly used configurations of wavy and porous heat exchangers in industrial applications.
- Discussed the effects of porous inserts in both straight and wavy ducts.
- Illustrated various porous material insertion configurations in ducts, namely porous layer attached to the wall (PLAW), centred porous layer (CPL), porous ribs attached to the wall (PRAW), local porous layer (LPL), partially filled porous material (PFPM), porous square pillars attached to the wall (PSPAW), among others.
- Described the characteristic parameters of corrugated walls, principally the wavelength and amplitude.

Finally, this paper aims to provide a comprehensive reference on straight and wavy porous duct heat exchangers. It offers valuable insights into compact heat exchanger design by evaluating the influence of wall geometry, porous inserts, and nanofluids on heat transfer performance. Although the advantages of these passive enhancement techniques are well established, potential drawbacks, such as increased manufacturing complexity, stability issues associated with nanofluids and porous inserts, and higher costs, must also be carefully considered.

CHAPTER 2:

PHYSICAL MODEL AND MATHEMATICAL FORMULATION

2.1 Introduction

Most applied studies in thermal engineering have focused on cavities [93–97], stretching sheets [98–102], and internal flows in channels and annuli [103–106]. In contrast, the present study develops a comprehensive physical model and mathematical formulation to analyze heat transfer, fluid flow, and entropy generation in a wavy channel heat exchanger. A two-dimensional, steady-state Darcy–Brinkman–Forchheimer model coupled with the Local Thermal Equilibrium (LTE) assumption is employed to accurately capture the thermal and hydrodynamic behaviors in both clear and porous regions, including packed granular beds and metal foam structures.

The formulation incorporates the governing conservation equations for mass, momentum, energy, and entropy generation, along with detailed boundary conditions and interface continuity requirements. Three distinct physical configurations are examined: a clear medium, a packed granular porous medium, and a metal foam porous medium. Additionally, the study investigates the evaluation of porous-medium coefficients based on the geometrical and physical characteristics of the porous structure, with particular emphasis on two widely used media: packed granular beds and metal foams.

2.2 Physical problem

The analyzed plate wavy channel heat exchanger is divided into three distinct sections, as illustrated in Fig. 1. The inlet and outlet regions are smooth and adiabatic, while the intermediate sinusoidal section is maintained at a constant temperature. The wavy wall is characterized by a wavelength b and an amplitude a. The inlet section has a length of $1.5H_c$, whereas the sinusoidal section extends over $12H_c$. . The geometrical profiles of the upper and lower wavy walls are defined by Eqs. (1) and (2), respectively [84].

$$y_t(x) = \frac{H_c}{2} - a\sin\left(\frac{\pi(x - x_1)}{b}\right) \tag{2.1}$$

$$y_b(x) = -\frac{H_c}{2} + a\sin\left(\frac{\pi(x - x_1)}{b}\right) \tag{2.2}$$

The dimensionless wave amplitude (α), wavelength (λ), and porous insert thickness are defined by the following equations:

$$\alpha = \frac{a}{H_c} \; ; \; \lambda = \frac{b}{H_c} \; ; \delta = \frac{H_p}{H_c} \tag{2.3}$$

where H_p denotes the porous insert thickness, H_c is the channel height, and x and y represent the Cartesian coordinates.

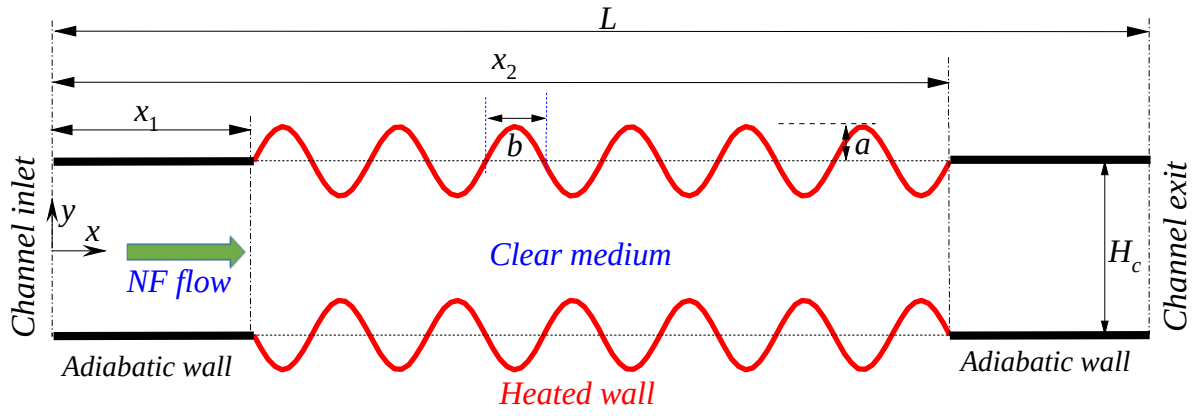


Figure 2.1 Schematic diagram of a sinusoidal wavy-plate channel filled with nanofluid (clear medium): physical configuration 1

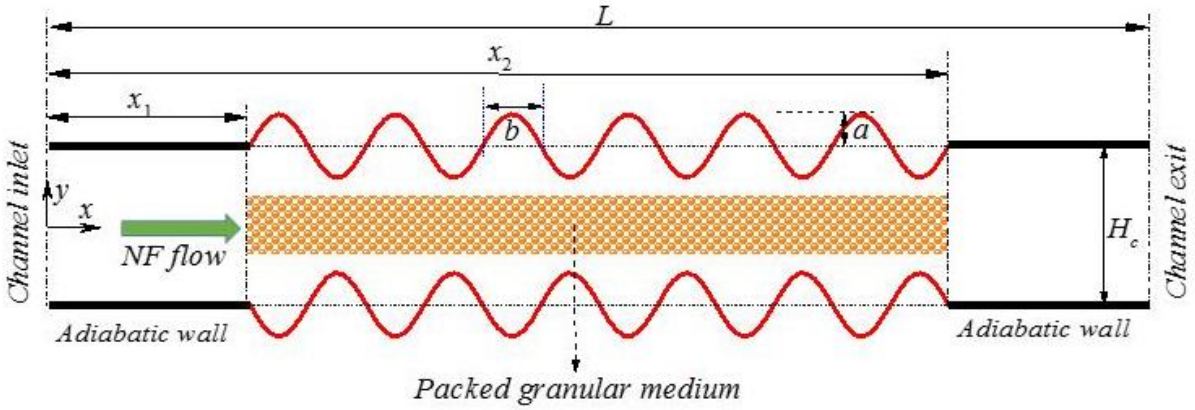


Figure 2.2 Schematic diagram of a sinusoidal wavy-plate channel partially filled with a packed granular porous medium: physical configuration 2

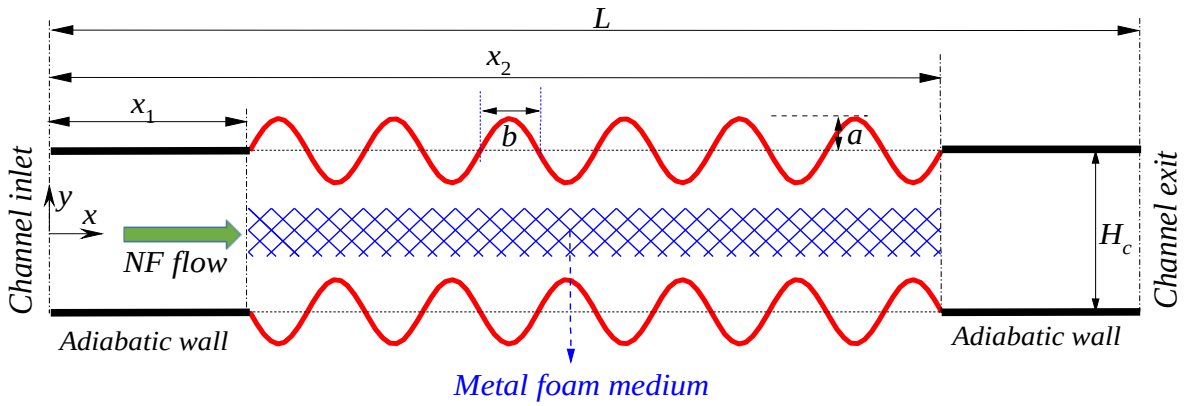


Figure 2.3 Schematic diagram of a sinusoidal wavy-plate channel heat exchanger partially filled with a metal-foam porous medium: physical configuration 3

2.3 Mathematical formulation

The formulation is based on a two-dimensional, laminar, steady-state Darcy–Brinkman–Forchheimer model for nanofluid (NF) flow, coupled with a local thermal equilibrium (LTE) model for the energy equation that accounts for viscous dissipation effects. In the expressions of thermophysical properties, the subscript f denotes the base fluid, np refers to the nanoparticles, p represents the porous material, and effeffeff indicates the effective properties of the porous medium saturated with nanofluid. Quantities without subscripts correspond to the nanofluid.

The base-fluid Reynolds number is defined as $Re = \rho_f u_{in} D/\mu_f$, where the hydraulic diameter is given by $D = 2\,H_c$.

2.3.1 Conservation equations

The one-phase mixture model (1PMM) was adopted because the assumptions underlying the homogeneous nanofluid approximation are reasonably satisfied in the present configuration. In particular, (i) the nanoparticle diameter is sufficiently small for the continuum assumption to remain valid, (ii) the nanoparticle concentration is relatively low, and (iii) the relative slip velocity between the nanoparticles and the base fluid is expected to be negligible. This assumption is further supported by the very small Stokes number $St = \tau_p/\tau_p$) defined as the ratio of the nanoparticle relaxation time, (τ_p), to the characteristic flow time, (τ_f). For the present water-based nanofluid, the estimated Stokes number is of the order of (10^{-6}–10^{-3}), corresponding to nanoparticle diameters of approximately (10–100) nm. Such small values

indicate that the nanoparticles respond rapidly to changes in the surrounding fluid motion and closely follow the fluid velocity. Consequently, the particle–fluid velocity slip is negligible, supporting the use of the one-phase mixture model rather than a computationally more computationally intensive two-phase model. Therefore, the continuity and momentum equations are expressed as follows [79,81]:

$$\nabla \cdot (\rho \vec{v}) = 0 \tag{2.4}$$

$$\frac{\rho}{\varepsilon^2}(\vec{v} \cdot \nabla)\vec{v} = -\nabla p + \frac{\mu}{\varepsilon}\nabla^2 \vec{v} - \lambda' \left(\frac{\mu}{K} + \frac{C_F \rho}{\sqrt{K}} |\vec{v}| \right) \vec{v} \tag{2.5}$$

In these equations, ρ denotes the mass density, p is the pressure, $\vec{v}$ represents the velocity vector, μ is the dynamic viscosity, K is the permeability, ε is the porosity, and C_F is the Forchheimer coefficient. The parameter λ' takes the value 0 in the clear-fluid region and 1 in the porous region.

The correlations employed to evaluate the porous-medium permeability K and the Forchheimer coefficient C_F for both packed granular and metal foam materials are presented in Section 4.

The local thermal equilibrium (LTE) model was adopted because the metallic porous matrix provides strong thermal coupling with the water–nanofluid, leading to a negligible temperature difference between the solid and fluid phases. Moreover, the porous medium is located away from the heated wall, where the thermal gradients and interfacial temperature differences are expected to be less significant. Therefore, the LTE assumption is considered appropriate for the present configuration. An NLTE model would be more appropriate if substantial temperature differences between the solid matrix and the fluid phase were expected. Consequentely, the energy equation is given by Eqs. (2.6) and (2.7) for the clear-fluid and porous regions, respectively.

$$\rho c \vec{v} \cdot \nabla T = \nabla \cdot (k \nabla T) + \phi_1 \tag{2.6}$$

$$\rho c \vec{v} \cdot \nabla T = \nabla \cdot \left(k_{eff} \nabla T \right) + \phi_2 \tag{2.7}$$

The viscous dissipation functions ϕ_1 and ϕ_2 are defined as follows [49–50]:

$$\emptyset_1 = \mu\left\{2\left(\frac{\partial u}{\partial x}\right)^2 + 2\left(\frac{\partial v}{\partial y}\right)^2 + \left(\frac{\partial u}{\partial y} + \frac{\partial v}{\partial x}\right)^2\right\} \tag{2.8}$$

$$\emptyset_2 = \mu_{eff}\left\{2\left(\frac{\partial u}{\partial x}\right)^2 + 2\left(\frac{\partial v}{\partial y}\right)^2 + \left(\frac{\partial u}{\partial y} + \frac{\partial v}{\partial x}\right)^2\right\} + \frac{\mu}{K}(u^2 + v^2) \tag{2.9}$$

Here, c denotes the specific heat capacity, k is the thermal conductivity, T represents the temperature, and u corresponds to the mass-averaged velocity vector.

2.3.2 Boundary conditions

At the channel inlet ($x = 0$), a uniform velocity and constant temperature were imposed.

$$u = u_{in};\ v = 0;\ T = T_{in} \tag{2.10}$$

At the channel exit ($x = L$), the variables (u, v, T) were assumed to satisfy the zero-gradient condition. At the channel walls, a no-slip condition was applied, with one wall being adiabatic and smooth, and the other wall corrugated at a constant temperature.

$$\vec{v} = \vec{0}\,;\ \begin{cases} \dfrac{\partial T}{\partial y} = 0 : 0 \le x \le x_1 \\ T = T_w : x_1 \le x \le x_2 \\ \dfrac{\partial T}{\partial y} = 0 : x_2 \le x \le (L - x_2) \end{cases} \tag{2.11}$$

At the interface between the clear fluid (region 1) and the porous medium (region 2), continuity conditions were applied, as reported in [80].

$$\vec{v}_{i,1} = \vec{v}_{i,2} \equiv u_{i,1} = u_{i,2}\ ;\ v_{i,1} = v_{i,2} \tag{2.12}$$

$$\mu\left(\frac{\partial u}{\partial y}\right)_{i,1} = \mu_{eff}\left(\frac{\partial u}{\partial y}\right)_{i,2} \tag{2.13}$$

$$T_{i,1} = T_{i,2} \tag{2.14}$$

$$k\left(\frac{\partial T}{\partial y}\right)_{i,1} = k_{eff}\left(\frac{\partial T}{\partial y}\right)_{i,2} \tag{2.15}$$

2.3.3 Physical properties

Nanofluids can be classified into several categories, including single nanofluids [107–110], hybrid nanofluids, such as Casson hybrid nanofluids [111–112], MgO–Al_2O_3/water hybrid nanofluids [113–114], Fe_3O_4–MWCNT/H_2O hybrid nanofluids [115–117], and MgO–Ag/water nanofluids [118–120], as well as special nanofluids, including ethylene glycol–water–based titania nanofluids [121–123], nanofluids applied in biomedicine and engineering [124–125], Casson nanofluid flows [126–128], and Jeffery nanofluids [129–130].

For the case of single nanofluids, the effective thermophysical properties are evaluated using the following correlations, as reported in [52].

$$\rho = (1-\varphi)\rho_{\mathrm{f}} + \varphi\rho_{np} \tag{2.16}$$

$$c = \frac{(1-\varphi)\rho_f c_{\mathrm{f}} + \varphi\rho_{np}c_{np}}{\rho} \tag{2.17}$$

$$\beta = \frac{(1-\varphi)\rho_f \beta_{\mathrm{f}} + \varphi\rho_{np}\beta_{np}}{\rho} \tag{2.18}$$

$$\frac{k}{k_{\mathrm{f}}} = \frac{k_{np} + 2k_{\mathrm{f}} + 2\varphi \times \left(k_{\mathrm{f}} - k_{np}\right)}{k_{np} + 2k_{\mathrm{f}} - \varphi \times \left(k_{\mathrm{f}} - k_{np}\right)} \tag{2.19}$$

The nanofluid viscosity is evaluated using the Brinkman model, which is suitable for spherical solid nanoparticles at moderate volume fractions [83].

$$\mu = \frac{\mu_{\mathrm{f}}}{(1-\varphi)^{2.5}} \tag{2.20}$$

The thermophysical properties of the porous medium are expressed as follows [80].

$$\rho_{eff} = (1-\varepsilon)\rho_{\mathrm{p}} + \varepsilon\rho \tag{2.21}$$

$$c_{eff} = (1-\varepsilon)c_{\mathrm{p}} + \varepsilon c \tag{2.22}$$

$$k_{eff} = (1-\varepsilon)k_{\mathrm{p}} + \varepsilon k \tag{2.23}$$

$$\mu_{eff} = \frac{\mu}{\varepsilon} \tag{2.24}$$

2.3.4 Physical parameters

2.3.4.1 Entropy

Flow irreversibilities, including thermal dissipation and viscous effects, lead to entropy generation, which can be described by Eqs. (2.27)–(2.28).

$$S = S_h + S_{\mathrm{v}} \tag{2.25}$$

The first term, S_h, in Eq. (25) represents the volumetric entropy generation rate due to thermal dissipation. The second term, S_{v}, corresponds to the volumetric entropy generation rate associated with viscous dissipation [33,131–133]. Accordingly, the entropy generation formulation is written separately for the clear fluid region and the porous region as follows:

Clear region

$$S_h = \frac{k}{T^2}\left[\left(\frac{\partial T}{\partial x}\right)^2 + \left(\frac{\partial T}{\partial y}\right)^2\right] \tag{2.26}$$

$$S_{\mathrm{v}} = \frac{\emptyset_1}{T} = \frac{\mu}{T}\left\{2\left(\frac{\partial u}{\partial x}\right)^2 + 2\left(\frac{\partial v}{\partial y}\right)^2 + \left(\frac{\partial u}{\partial y} + \frac{\partial v}{\partial x}\right)^2\right\} \tag{2.27}$$

Porous region

$$S_h = \frac{k_{eff}}{T^2}\left[\left(\frac{\partial T}{\partial x}\right)^2 + \left(\frac{\partial T}{\partial y}\right)^2\right] \tag{2.28}$$

$$S_{\mathrm{v}} = \frac{\emptyset_2}{T} = \frac{\mu_{eff}}{T}\left\{2\left(\frac{\partial u}{\partial x}\right)^2 + 2\left(\frac{\partial v}{\partial y}\right)^2 + \left(\frac{\partial u}{\partial y} + \frac{\partial v}{\partial x}\right)^2\right\} + \frac{\mu}{K\,T}(u^2 + v^2) \tag{2.29}$$

2.3.4.2 Nusselt number

The local Nusselt number (Nu), the mean Nusselt number (Nu_m), and the mean entropy generation (S_m) are defined as in [79], where n denotes the direction perpendicular to the wavy surface.

$$Nu = \frac{hH_c}{k_{nf}} \quad \text{or} \quad Nu = -\frac{\left.\frac{\partial T}{\partial n}\right|_w H_c}{(T_w - T_{in})} \tag{2.30}$$

$$Nu_m = \overline{Nu} = \frac{1}{x_2 - x_1}\int_{x_1}^{x_2} Nu dx \;\; ; \;\; S_m = \bar{S} = \frac{1}{x_2 - x_1}\int_{x_1}^{x_2} S dx \tag{2.31}$$

2.3.4.3 Performance evaluation creteria

The performance evaluation criterion (PEC), used to compare the hydrodynamic and thermal performance of different systems, is defined as in [26, 28]:

$$PEC = \frac{\overline{Nu}/\overline{Nu}_s}{\left(\bar{f}/\bar{f}_s\right)^{1/3}} \tag{2.32}$$

Here, $\bar{f}$ and $\bar{f}_s$, as well as $\overline{Nu}$ and $\overline{Nu}_s$, represent the average friction factor and Nusselt number for the wavy and smooth channels, respectively.

2.4 Porous medium coefficients

The evaluation of porous media properties, particularly permeability, is crucial for numerical simulations and for predicting the thermal and dynamic behavior of porous systems. Various methodologies are employed depending on the nature of the porous media, specifically as outlined below:

2.4.1 Packed granular porous medium

Badri et al. [134] investigated the use of granular materials (GM) to reduce low-frequency impact sound transmission in lightweight floors. Several methods for estimating damping were reviewed to analyze the interaction between floor and excitation (Fig. 8). Multi-particle systems with varying characteristics were examined. The results indicate that GM can substantially enhance vibration isolation and sound absorption in building applications.

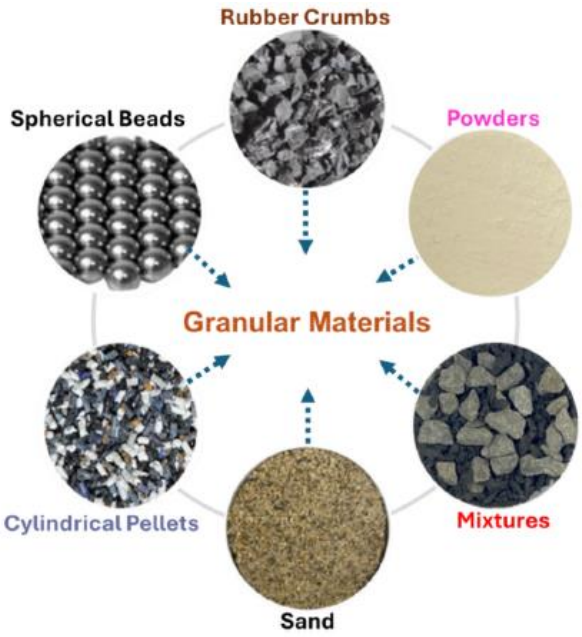


Figure 2.4 Examples of granular materials in nature and industry [134].

Forchheimer's equation has been effectively used to determine the permeability of granular media. It indicates that, for incompressible fluid flow, the pressure drop in a porous medium (PM) is given by [135]. In this equation, the constants K and K' depend solely on the medium's properties, representing the Darcian and non-Darcian permeabilities, respectively.

$$\frac{\Delta p}{L} = \frac{\mu}{K}u + \frac{\rho}{K'}u^2 \tag{2.33}$$

Ergun [136] proposed a similar formulation for equation (2.33):

$$\frac{\Delta p}{L} = \frac{\mu}{K}u + \frac{C_F}{\sqrt{K}}\rho u^2 \tag{2.34}$$

For a packed granular medium, the proposed expression for K is given as follows:

$$K = \frac{\varepsilon^3 \Phi^2 d^2}{150(1-\varepsilon)^2} \tag{2.35}$$

Here, L, ΔP, and Φ represent the bed length, the pressure drop, and the particle sphericity, respectively, and the Forchheimer and inertial coefficients are given by:

$$C_F = \frac{1.75}{\sqrt{150\varepsilon^3}} \tag{2.36}$$

$$C_2 = \frac{2C_F}{\sqrt{K}} = 3.5\frac{(1-\varepsilon)}{\varepsilon^3 d\Phi} \tag{2.37}$$

For spherical particles, the porosity of granular packed beds can be accurately described using the Furnas relation:

$$\varepsilon = 0.375 + 0.34\frac{d}{H_p} \tag{2.38}$$

A new model for the porosity of packed granular beds composed of spherical particles was proposed [137]:

$$\varepsilon = 0.36 + 0.08\left(\frac{d}{H_p}\right)^{0.5} \tag{2.39}$$

Here, H_p denotes the thickness of the porous medium (PM), and d is the average particle diameter.

2.4.2 Foam porous medium

Ranut et al. [97, 98] investigated the potential of open-cell aluminum metal foams to enhance thermal efficiency. They employed microtomography-based CFD simulations to study HTF flow in various foam samples with different pore densities (10, 20, and 30 PPI). The results indicate that the 30 PPI foam exhibits isotropic properties, whereas the 20 and 10 PPI foams display anisotropy due to their structural characteristics (Fig. 9). This study underscores the importance of evaluating thermal conductivity and flow permeability for practical applications.

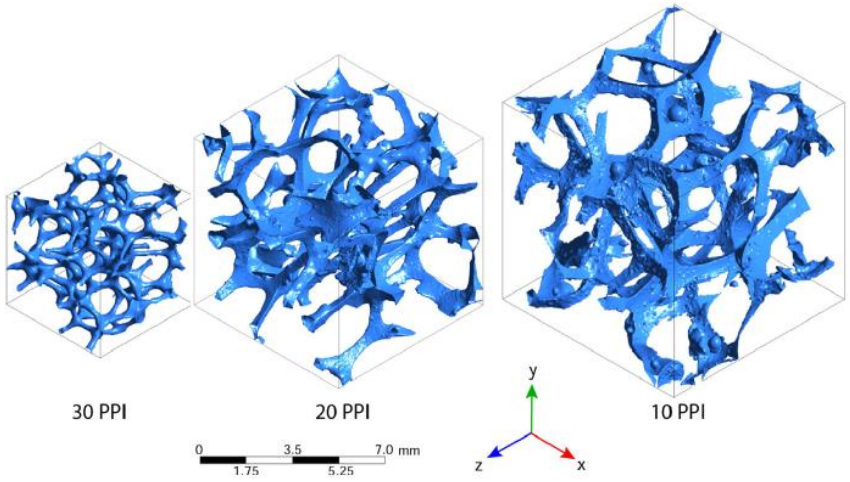


Figure 2.5 Metal foam structure representation showing cubic volumes used for CFD computations [138,139].

The assessment of these factors remains an important consideration. Permeability is influenced by several parameters, notably pore density (PPI), pore diameter, and fiber diameter. It can be evaluated using two approaches: empirical correlations and experimental measurements.

2.4.2.1 Experimental evaluation of permeability

Table 2.1 lists the experimentally measured properties of porous foams, including pore density (ω), porosity (ε), pore diameter (d_{po}), fiber diameter (d_f), and permeability (K).

Table 2.1 Experimental Permeability Values of Foam Materials

Reference	Foam	ω (PPI)	ε	d_{po} (m)	d_f (m)	K (m^2)
Hamzah and Nima [140]	Copper	40	0.89	-	-	1.75×10^{-8}
Pourfarzad et al. [141]	Copper	15	0.90	$1.642\text{x}10^{-3}$	$501\text{x}10^{-6}$	1.816×10^{-7}
Alhajaj et al. [27]	6061-T6	40	0.91	-	-	3.36×10^{-8}
Kamath et al. [24]	Aluminum	10	0.95	-	-	2.480×10^{-7}
		20	0.90	-	-	2.177×10^{-7}
		30	0.92	-	-	1.644×10^{-7}
		45	0.90	-	-	0.420×10^{-7}
Kamath et al. [142]	Copper	10	0.88	-	-	1.742×10^{-7}
Borakhade and Mahalle [143]	Copper	40	0.96	0.000565	-	1.340×10^{-9}

		50	0.94	0.000533	-	1.306×10^{-9}
		60	0.95	0.000495	-	1.0012×10^{-9}
Calmidi and Mahajan [144]	Aluminum	5	0.97	0.00402	0.00050	2.7×10^{-7}
		10	0.95	0.00313	0.00040	1.2×10^{-7}
		20	0.90	0.00258	0.00035	0.8×10^{-7}
		40	0.91	0.00180	0.00025	0.53×10^{-7}

2.4.2.2 Evaluation from correlations

2.4.2.2.1 Modified Ergun correlation

A general modified Ergun correlation was derived based on the experimental results.

$$K = \frac{\varepsilon^3 d_f^2}{\sigma(1-\varepsilon)^2} \tag{2.40}$$

Numerical studies by [25], [60], [145], and [146] indicate that the selected value for the coefficient σ is 150. Experimental results suggest a suitable value of 180 for [147] and [148]. For [149], σ falls within the range 100–865, while $\sigma = 175$ is reported in [58].

2.4.2.2.2 Calmidi correlation

Calmidi and Mahajan [144] proposed a distinct formulation for permeability based on experimental evidence. The permeability depends on three key characteristics of metal foams: average pore diameter d_{po}, pore density ω (measured in PPI), and average fiber diameter d_f. The Calmidi correlation, presented in Equations (9)–(11), has been employed in several recent studies [59, 150, 151].

$$K = 0.00073 d_{po}^2 (1-\varepsilon)^{-0.224} \left(\frac{d_f}{d_{po}}\right)^{-1.11} \tag{2.41}$$

$$d_{po} = \frac{0.0254}{\omega} \tag{2.42}$$

$$d_f = 1.18 d_{po} \sqrt{\frac{(1-\varepsilon)}{3\pi}} \frac{1}{1-\exp\left[-\frac{(1-\varepsilon)}{0.04}\right]} \tag{2.43}$$

where the parameters C_F and C_2 are defined as follows:

$$C_F = 0.00212(1-\varepsilon)^{-0.132}\left(\frac{d_f}{d_{po}}\right)^{-1.63} \tag{2.44}$$

$$C_2 = \frac{2C_F}{\sqrt{K}} \tag{2.45}$$

2.4.2.2.3. Theoretical models for the evaluation of permeability

The permeability expression was derived as a function of tortuosity χ, porosity ε, and the width d_c of the cubic representative unit cell [152].

$$K = \frac{\varepsilon^2 d_c^2}{36\chi(\chi-1)} \tag{2.46}$$

Yang et al. [153] proposed a permeability equation applicable to porosities in the range $\varepsilon = 0.55-0.98$ and pore densities (ω) from 5 to 100 PPI, expressed as a function of porosity and the cross-sectional pore diameter D_p.

$$K = \frac{\varepsilon\left[1-(1-\varepsilon)^{1/3}\right]}{108[(1-\varepsilon)^{1/3}-(1-\varepsilon)]} D_p^2 \tag{2.47}$$

2.5. Conclusion

The developed physical model offers a robust framework for evaluating system performance, accounting for factors such as viscous dissipation, permeability, and porosity. Key performance metrics, including the Nusselt number, entropy generation rate, and Performance Evaluation Criteria (PEC), enable a comprehensive assessment of thermal efficiency and flow resistance. Overall, this formulation serves as a valuable tool for optimizing heat exchanger designs, enhancing heat transfer, and minimizing energy losses.

CHAPTER 3:

NUMERICAL SOLUTIONS AND VALIDATION

3.1 Introduction

This study successfully investigated fluid flow and heat transfer in clear and porous channels using ANSYS Fluent 2020R1.

High numerical accuracy was ensured through the use of structured meshes and second-order discretisation schemes, particularly in the near-wall regions and at fluid–porous interfaces [154–156].

The numerical methodology was validated against available literature and experimental data, demonstrating strong agreement for both wavy and porous channel configurations.

3.2 Numerical procedure for solving

In this study, ANSYS Fluent 2020R1 was employed to solve the governing equations using the finite volume method. A structured square mesh was applied throughout the computational domain. The SIMPLE and Coupled algorithms were used for pressure–velocity coupling. Spatial discretisation was carried out using the Least Squares Cell-Based method for gradient evaluation, while second-order schemes were adopted for the pressure, momentum, and energy equations. Convergence was ensured by setting the absolute residuals to 10^{-7} for continuity and velocity components in both directions, and 10^{-9} for the energy equation. These numerical settings ensured high accuracy of the computed results.

3.3. Mesh generation

Figures 3.1 and 3.2 present detailed views of the computational meshes for the clear channel ($\delta = 0$) and the porous channel ($\delta = 0.4$), respectively. High-quality structured square meshes were employed throughout the computational domain.

Due to the pronounced variations in physical properties, mesh refinement was applied near the channel walls and at the clear fluid–porous medium interface. This locally refined mesh ensures the accuracy of the numerical calculations.

To assess mesh independence, several grids with different cell counts were generated and analysed for each porous layer thickness, and comparative calculations were performed to confirm the grid–computational domain independence of the results.

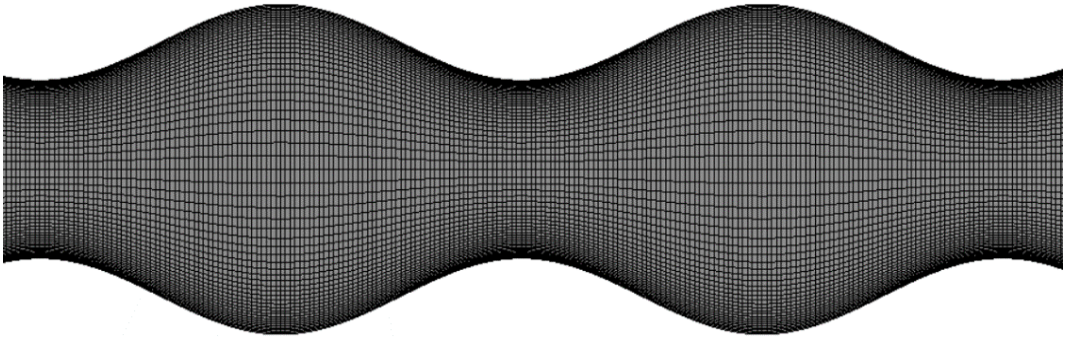


Figure 3.1 Mesh generation in the clear region and near the walls (δ = 0)

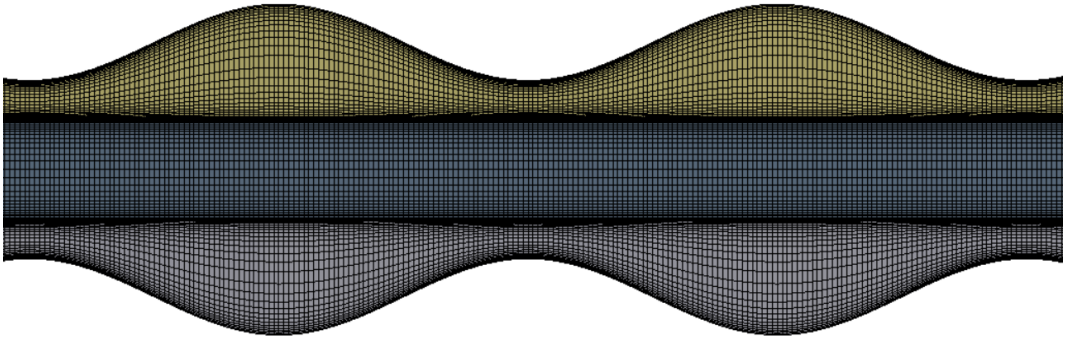


Figure 3.2 Mesh generation in the clear and porous domains, near the walls, and at the nanofluid–porous medium interfaces (δ = 0.4)

3.4 Numerical solution-Mesh independency

Figures 3.3 and 3.4 illustrate the variation of the average Nusselt number as a function of the number of mesh elements for the clear and porous channels, respectively.

These figures present a representative sample used to conduct the mesh independence test. As reported in Table 3.1, Grid 6 exhibits a relative variation of only 0.04% for the clear channel and 0.004% for the porous channel in the average Nusselt number. Consequently, Grid 6 was selected as the optimal mesh for the numerical simulations, as further mesh refinement resulted in negligible changes in the computed results.

The same mesh independence procedure was applied to the remaining geometries corresponding to different porous layer thicknesses to ensure consistent numerical accuracy across all cases.

Table 3.1 Mean Nusselt number for different grid sizes

	Grid	Number of elements	Number of nodes	Nu_m	$\Delta Nu_m/Nu_m$ (%)
Clear channel (δ=0)	1	19640	20643	5.372417	
	2	39480	40919	5.664303	5.153
	3	79400	81426	5.788509	2.146
	4	99250	101286	5.821134	0.560
	5	119130	121278	5.832275	0.191
	6	142400	144261	5.834605	0.040
Porous channel (δ=0.4)	1	18150	20024	9.652966	
	2	38805	41864	9.913019	2.623
	3	78880	83067	10.08599	1.715
	4	119680	123917	10.13936	0.526
	5	155660	161245	10.16953	0.297
	6	176156	181949	10.16909	0.004

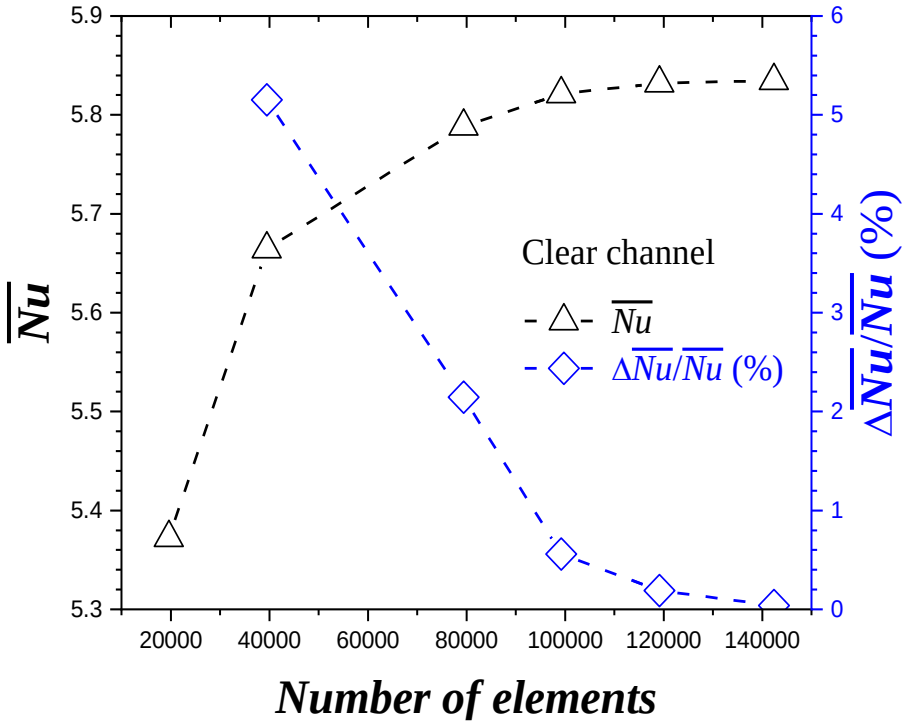


Figure 3.3 Mesh independence study for the clear channel

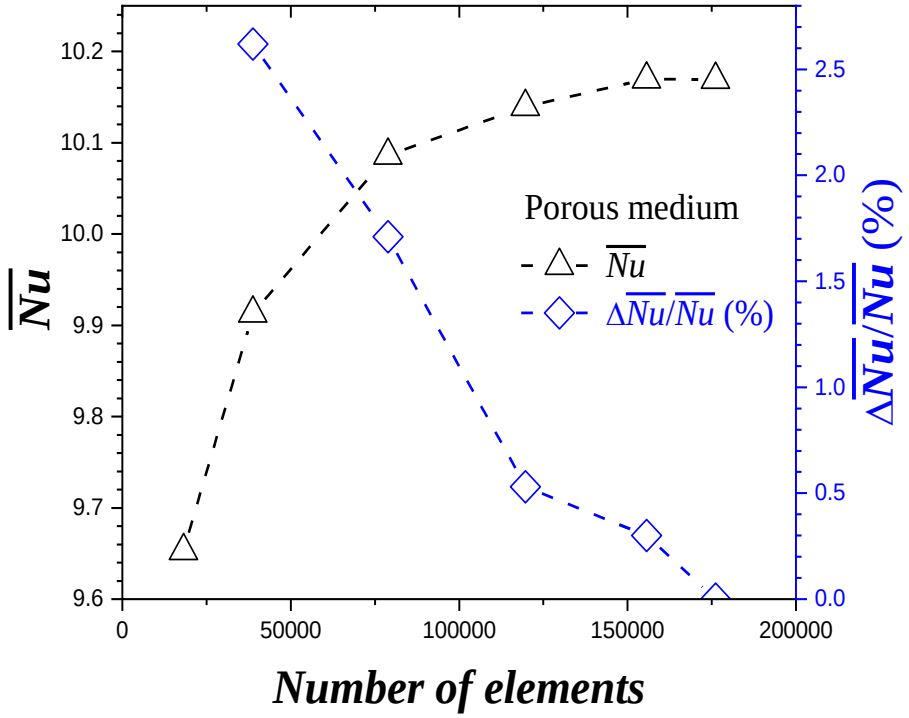


Figure 3.4 Mesh independence study for the porous channel (δ = 0.4)

3.5 Numerical validations

To evaluate the accuracy of the numerical approach employed in this study, the present results are compared with previously published works for two benchmark cases: wavy clear channels and porous sinusoidal channels, as illustrated in Figures 3.5 and 3.6, respectively. In addition, comparisons of velocity profiles and heat transfer coefficients are presented in Figures 3.7, 3.8, and 3.9, further demonstrating the reliability of the numerical methodology.

Figure 3.5 presents the distribution of the local Nusselt number (Nu) along the wavy section of the channel for forced convection at $Re = 500$, $\alpha = 0.2$, and $Pr = 6.93$, where α denotes the ratio of wave amplitude to wavelength. As shown in the figure, satisfactory agreement is achieved between the present results and those reported by Wang and Chen [62], validating the numerical approach. The results indicate that Nu attains higher values in the converging regions of each wave than in the diverging regions. This behaviour is attributed to the higher local velocity and velocity gradients in the converging sections, which enhance convective heat transfer. Moreover, the maximum Nu occurs near the beginning of the first wave, after which it gradually decreases and approaches a quasi-constant value at larger axial positions X.

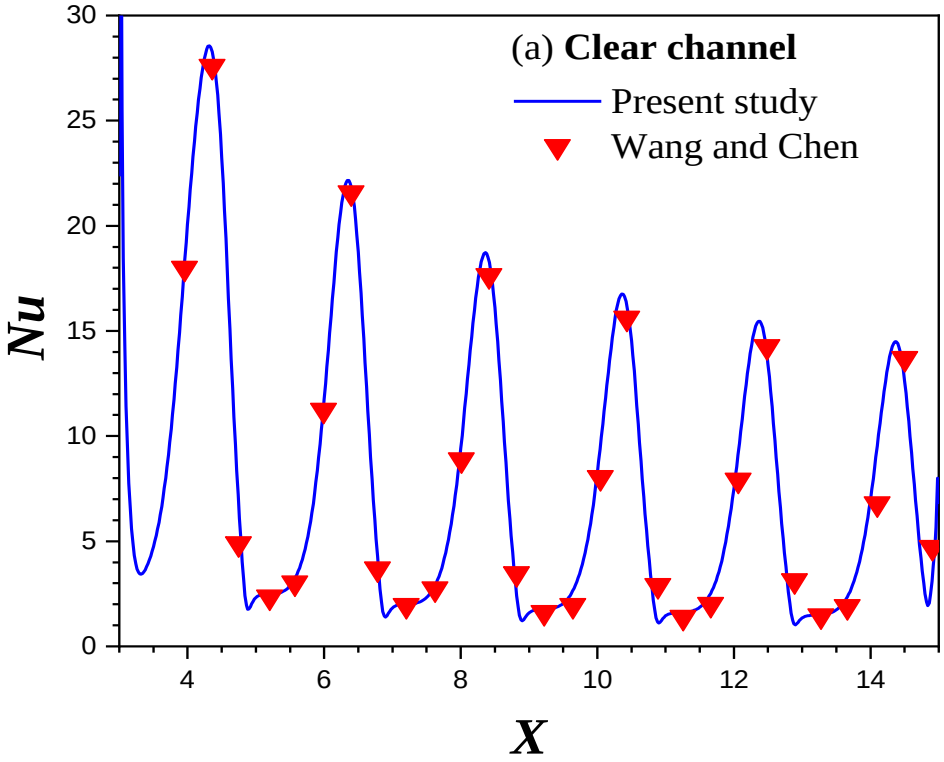


Figure 3.5 Comparison of the present results with literature data for local Nusselt numbers: (a) wavy non-porous channel [62], $Re = 500$, $\alpha = 0.2$

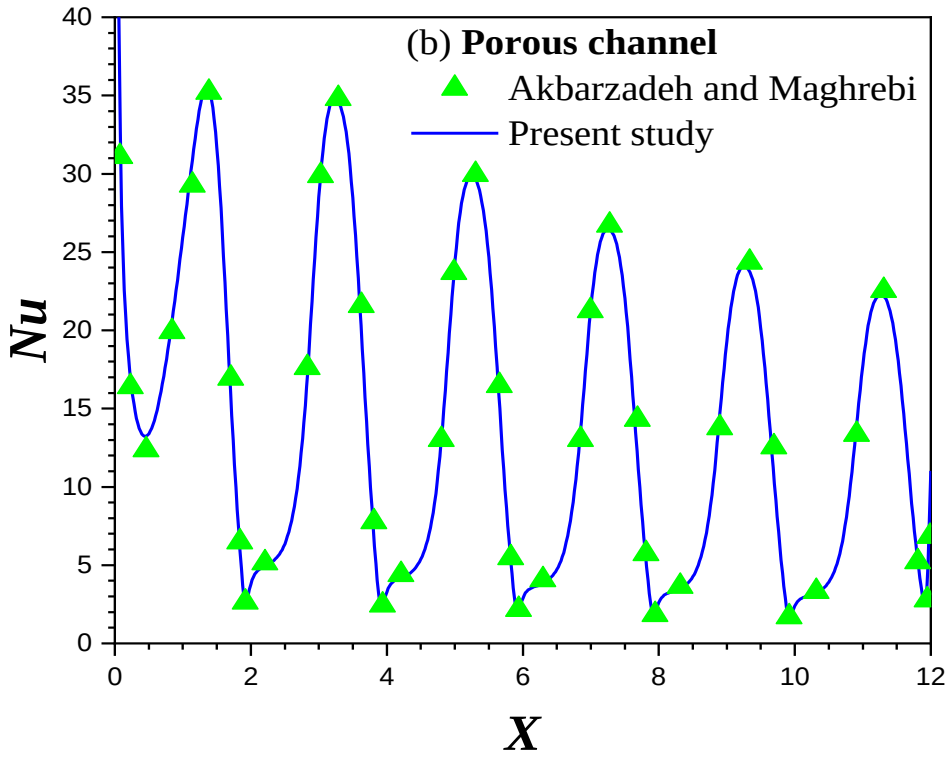


Figure 3.6 Comparison of the present results with literature data for local Nusselt numbers: (b) wavy porous channel [79], $Re = 300$, $Da = 10^{-4}$, $\alpha = 0.15$, $\delta = 0.3$

Figure 3.6 illustrates the distribution of the local Nusselt number along a wavy sinusoidal channel partially filled with a porous substrate at $Re = 300$, $Da = 10^{-6}$, $\alpha = 0.15$, and $\delta = 0.3$.

The results obtained in the present study show good agreement with those reported by Akbarzadeh and Maghrebi [79], further confirming the validity of the numerical model.

Figures 3.7 and 3.8 present a comparison between the dimensionless velocity profiles obtained numerically and the analytical solution of Torabi et al. [40] for fully developed nanofluid forced convection in a straight channel partially filled with a central porous insert. Excellent agreement is observed between the numerical and analytical results.

In this comparison, two limiting cases are considered: $\delta = 0$, corresponding to a channel without a porous medium, and $\delta = 1$, representing a channel completely filled with porous material.

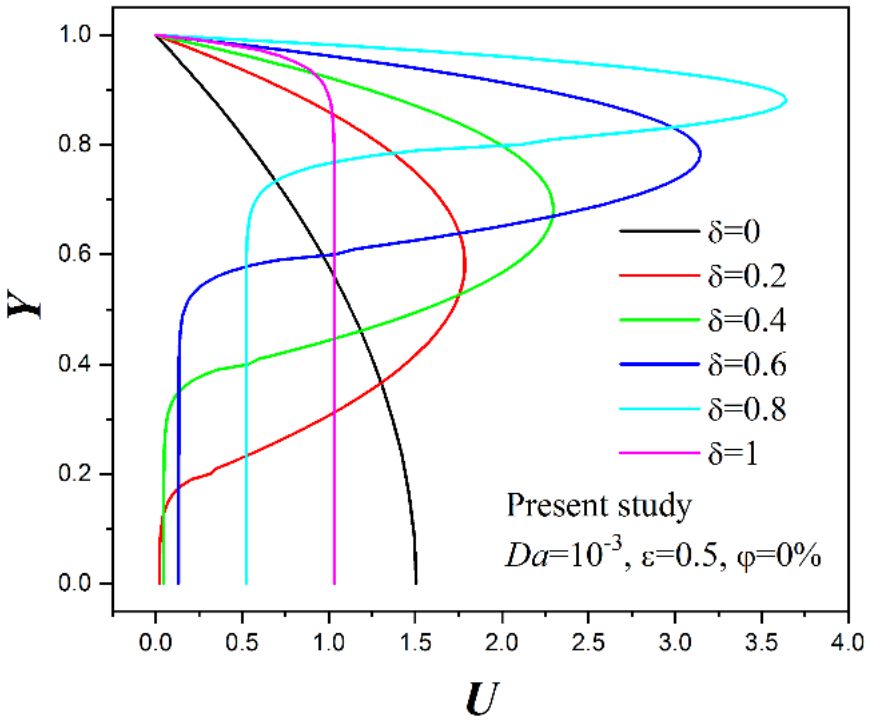


Figure 3.7 Present numerical results of the dimensionless velocity distribution for different dimensionless porous medium thicknesses

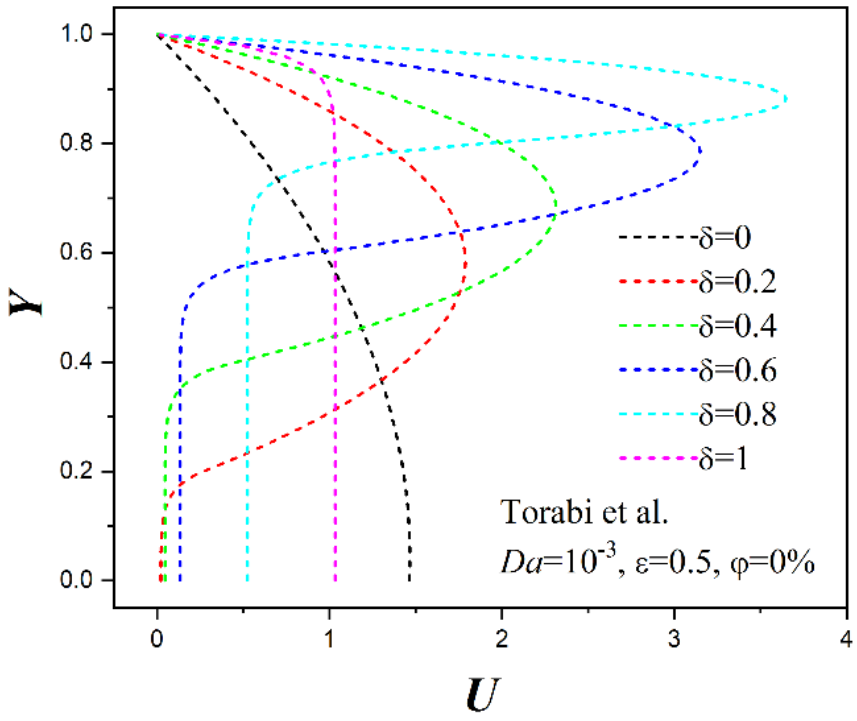


Figure 3.8 Analytical solution of Torabi et al. [41] for the dimensionless velocity distribution at different dimensionless porous medium thicknesses

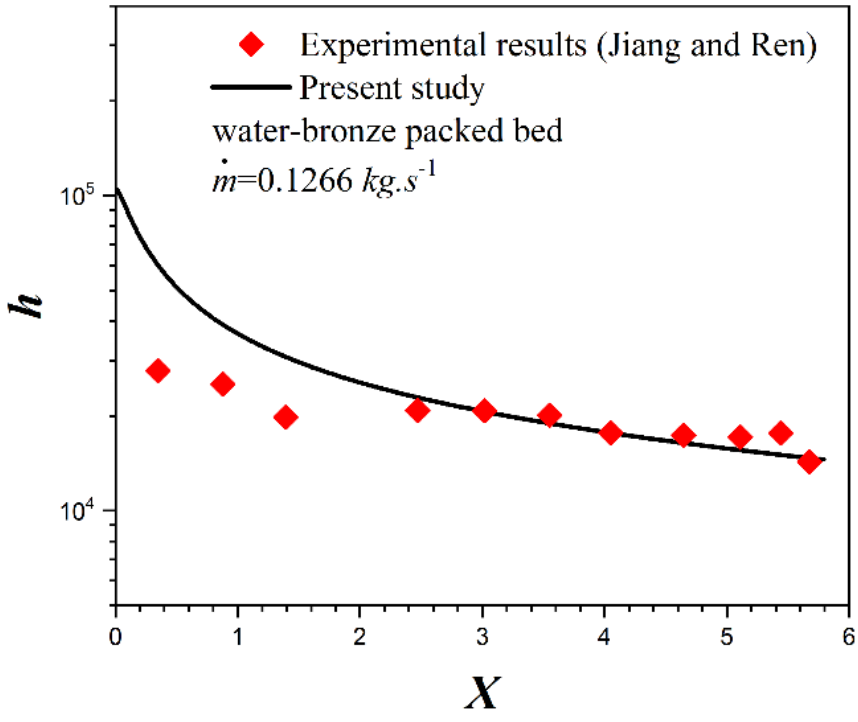


Figure 3.9 Comparison of the present numerical results with the experimental data of Jiang and Ren [22] for the local heat transfer coefficient: water, straight porous channel, $d_p = 0.428$ mm, $\varepsilon = 0.365$, $k_p = 75.35$ W·m⁻¹·K⁻¹

Figure 3.9 presents a comparison between the numerical results and the experimental data of Jiang and Ren [22] for a copper channel filled with packed metallic bronze particles, modeled as a homogeneous and isotropic porous medium. Water was employed as the working fluid. The upper plate of the channel is subjected to a constant heat flux via electrical heating, while the lower plate is thermally insulated.

The numerical results slightly overpredict the experimental heat-transfer coefficient, particularly near the channel inlet. This difference may result from the idealizations adopted in the numerical model compared with the actual experimental configuration. In particular, axial heat conduction through the relatively thick heated plate may redistribute heat in the streamwise direction and modify the local wall temperature. In addition, unavoidable heat losses from the experimental setup to the surroundings may reduce the effective heat transferred to the fluid and consequently lead to lower experimental values. Other experimental factors, such as thermal contact resistance and possible non-uniformities in particle packing and porosity, may also contribute to the observed discrepancy, whereas these effects are not explicitly considered in the homogeneous and isotropic porous-medium model. These effects are expected to be more significant near the inlet, where the thermal field is still developing. Nevertheless, the overall agreement between the numerical and experimental results remains satisfactory.

3.6 Conclusion

The results demonstrate the capability of the numerical methodology to accurately capture complex heat transfer and fluid flow phenomena in porous media. This study offers valuable insights for the design and optimization of engineering systems, such as heat exchangers and filtration units, emphasizing the critical roles of mesh independence and high-accuracy numerical schemes. Overall, the findings provide a robust foundation for future investigations and innovations in fluid–porous interactions.

CHAPTER 4 (A):

HEAT TRANSFER IN A WAVY CHANNEL-POROUS PACKED GRANULAR MEDIUM

4.1A Introduction

In this section, the influence of porous medium thickness on the key parameters characterizing nanofluid flow within the corrugated channel is analyzed. These parameters include velocity vector contours and magnitude, streamlines, isotherm contours, local and mean Nusselt numbers, entropy, and the relative variations of Nusselt number and entropy. In the simulations, the dimensionless amplitude (α), wavelength (λ), and porosity of the corrugated channel are fixed at 0.2, 0.5, and 0.375, respectively. Six different geometries of the partially porous channel (PCC) are considered, corresponding to dimensionless porous medium thickness values of $\delta = 0$, 0.1, 0.2, 0.3, 0.4, 0.5, and 0.6. The numerical simulations are conducted using water as the base fluid, CuO nanoparticles, and AISI 304 as the porous medium, with physical properties provided in [22, 28]. Furthermore, the effects of nanoparticle volume fraction ($\varphi = 0\text{–}5\%$) and Reynolds number ($Re = 200\text{–}500$) are examined. The simulation and computational parameters are summarized in Table 4.1A.

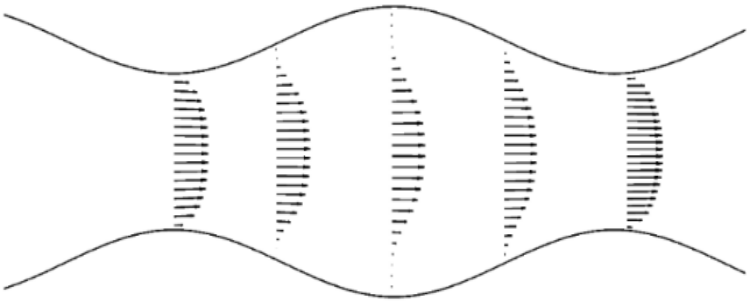
Table 4.1A. Simulation data for the corrugated plate channel.

Geometry	Wavy channel and Porous wavy channel
Dimensionless corrugation amplitude (α)	0.15
Dimensionless corrugation length (λ)	2
Base fluid	Water
Porous medium	AISI 304
Nanoparticles	CuO
Nanoparticles fraction φ (%)	0, 1, 2, 3, 4, 5
Dimensionless porous insert thickness (δ)	0, 0.1, 0.2, 0.3, 0.4, 0.5, 0.6
Reynolds number (*Re*)	200, 300, 400, 500

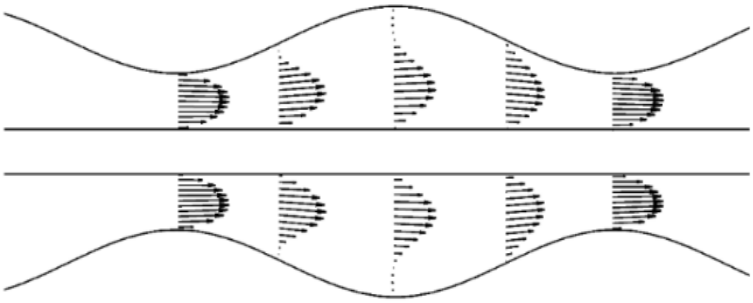
4.2A Effect of porous layer thickness on velocity vectors and streamlines

Figure 4.1A illustrates the velocity vectors for various values of δ at $Re = 500$ and $\varphi = 5\%$, showing their evolution along different locations of the channel. For δ =0, the velocity vectors reach their maximum at the channel centerline. However, the presence of a porous insert significantly reduces the velocity in this region. In the convergent sections of the channel, the velocity vectors exhibit higher intensity compared to other areas. Flow reversal

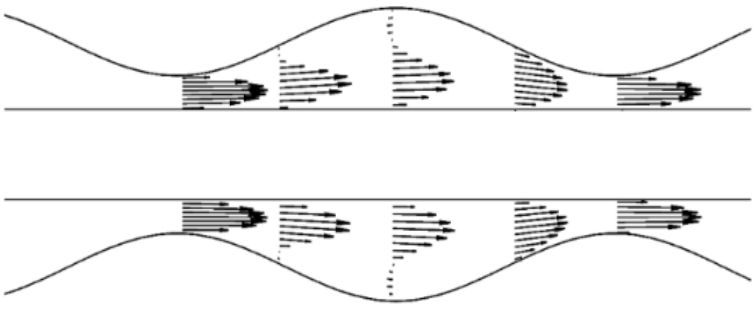
occurs predominantly in the diverging sections of the undulating walls. These reversed flows create recirculation zones that disturb the overall flow, significantly influencing the temperature distribution within the channel.



δ=0



δ=0.2

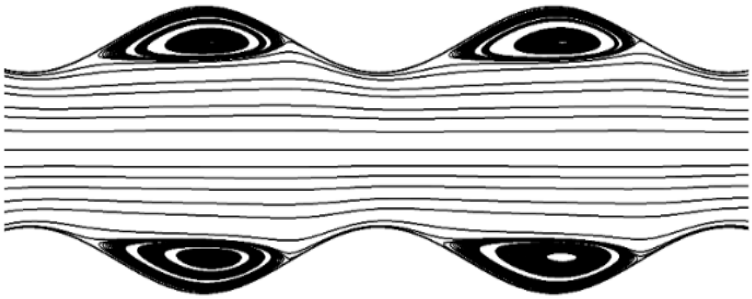


δ=0.4

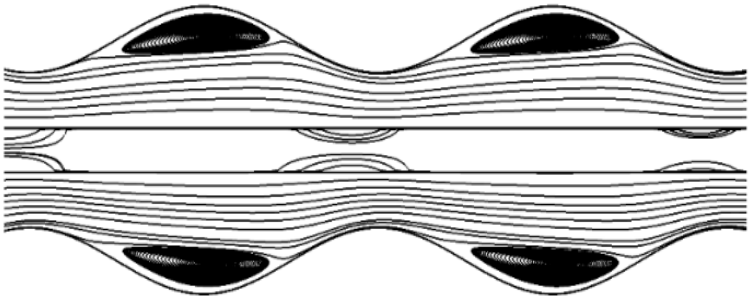
Figure 4.1A. Effect of δ on velocity vectors at $Re = 500$ and $\varphi = 5\%$.

Figure 4.2A shows the streamlines for various values of δ at $Re = 500$ and $\varphi = 5\%$. As illustrated, reverse flow occurs within the diverging sections of the wavy wall. With increasing δ, the size and intensity of the recirculation zones grow, causing greater

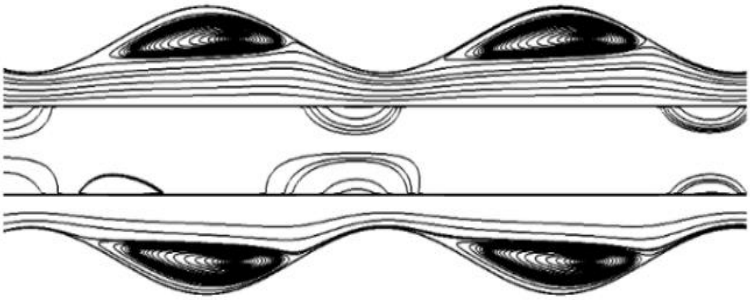
disturbances in the flow pattern. In this section, the influence of these vortices on heat transfer, flow behavior, and entropy generation within the wavy channel is examined.



δ=0



δ=0.2



δ=0.4

Figure 4.2A. Effect of δ on streamlines at $Re = 500$ and $\varphi = 5\%$.

4.3A Effect of porous layer thickness on velocity magnitude and isotherms

Figure 4.3A presents the velocity magnitude distribution for various values of δ at $Re = 500$ and $\varphi = 5\%$. As shown, two distinct regions of fast-moving fluid are observed near the

upper and lower portions of the porous insert. For $\delta = 0$, these high-velocity regions are entirely uniform. As expected, the velocity increases in the convergent sections of the wavy wall. Increasing δ further enhances the velocity magnitude within these fast-flow regions. Conversely, low velocities occur in the divergent sections of the wavy wall due to fluid recirculation.

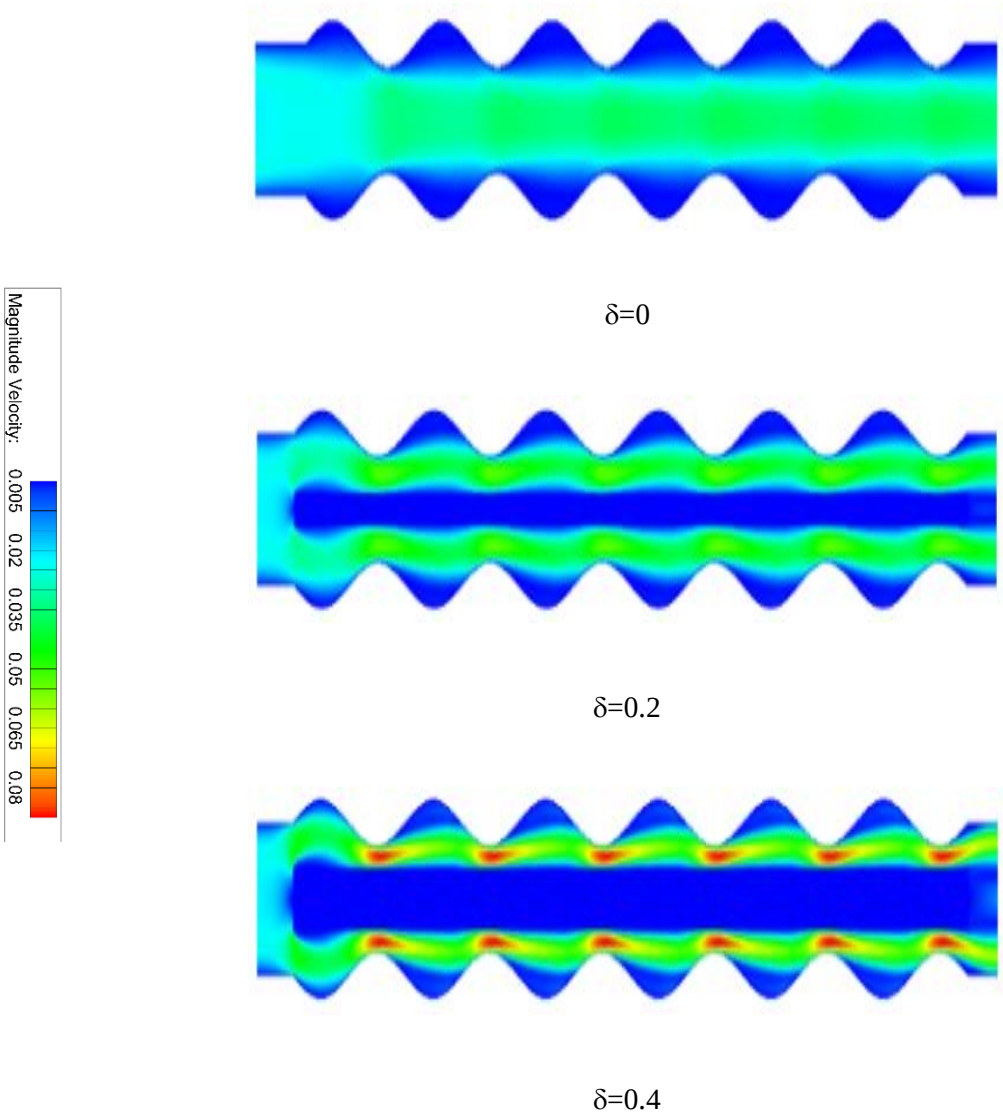


Figure 4.3A. Effect of δ on velocity magnitude at $Re = 500$ and $\varphi = 5\%$.

Figure 4.4A depicts the isotherms for various values of δ at $Re = 500$ and $\varphi = 5\%$. The figure shows that the thermal boundary layer thickness decreases as the porous layer thickness increases. As δ increases, more fluid flows through the clear region, causing the isotherms to become more compact near the undulating surfaces and enhancing the temperature gradients. In the diverging sections of the wavy walls, the fluid temperature is

higher than in the converging sections due to the influence of vortices, which generate reverse flow in these regions.

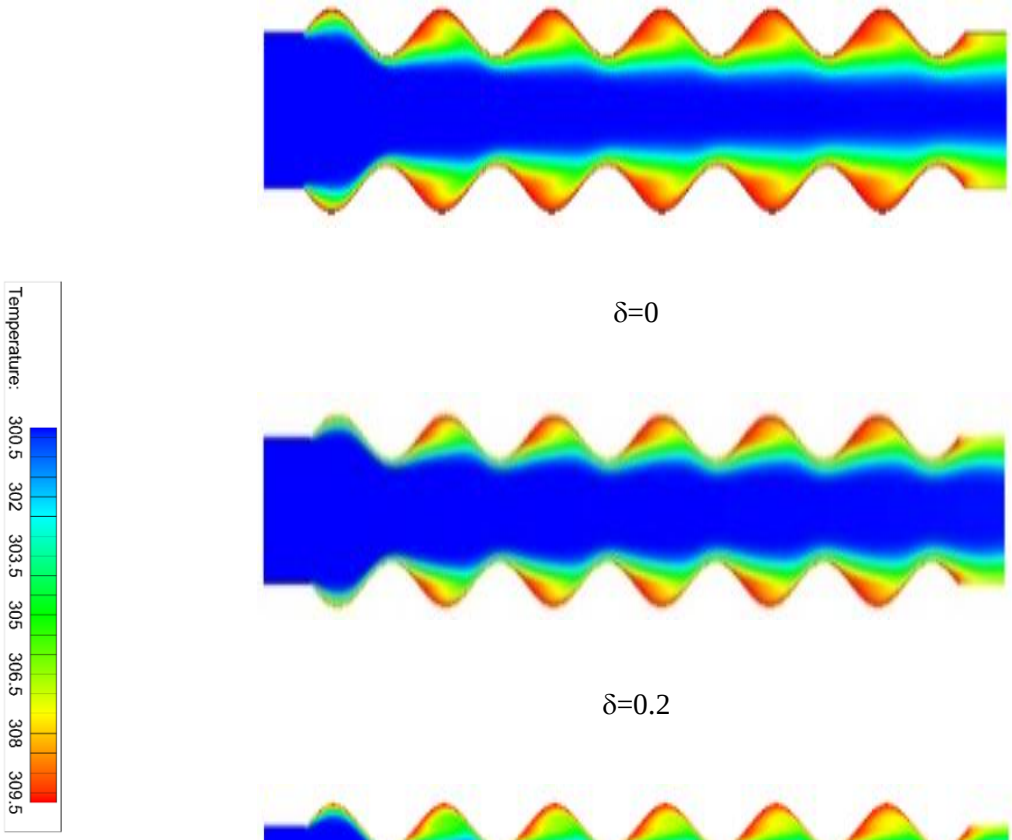


Figure 4.4A. Effect of δ on isotherms at $Re = 500$ and $\varphi = 5\%$.

4.4A Effect of porous layer thickness on *Nu* and *S*

Figures 4.5A and 4.6A illustrate the effect of δ on the Nusselt number (Nu) and entropy generation (S) along the length of the heated channel at $Re = 200$ and $\varphi = 5\%$. As shown, both Nu and S reach their maximum values in the converging sections of the channel, while attaining their minimum values in the diverging sections. Additionally, in the convergent regions, Nu and S increase with increasing δ, indicating enhanced heat transfer. This enhancement reduces the thermal boundary layer thickness, further increasing the local heat

transfer rate. In contrast, for a straight channel, Nu and S are highest at the inlet and gradually decrease along the channel length.

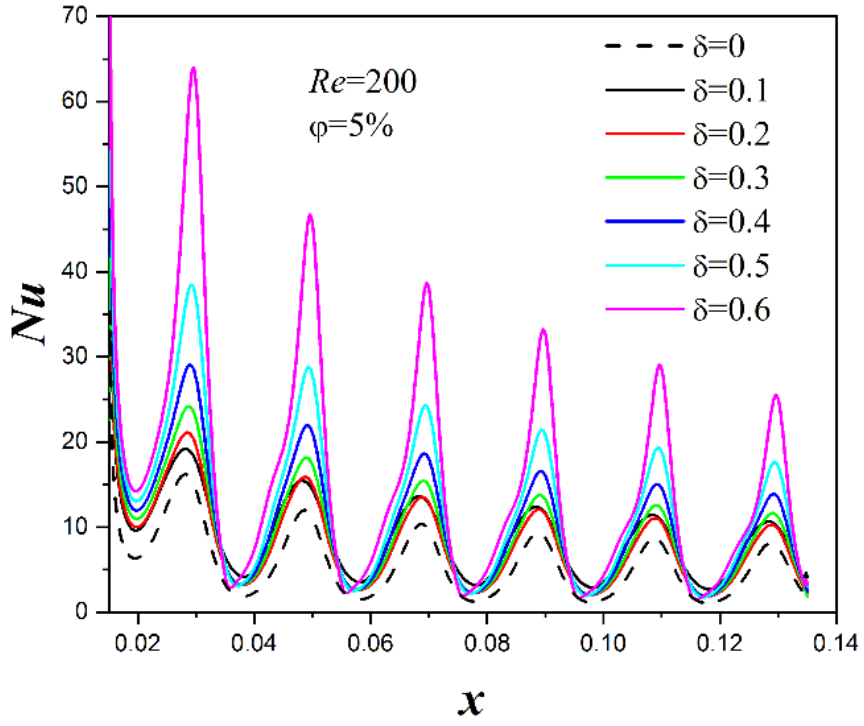


Figure 4.5A. Effect of porous insert thickness on local Nusselt number.

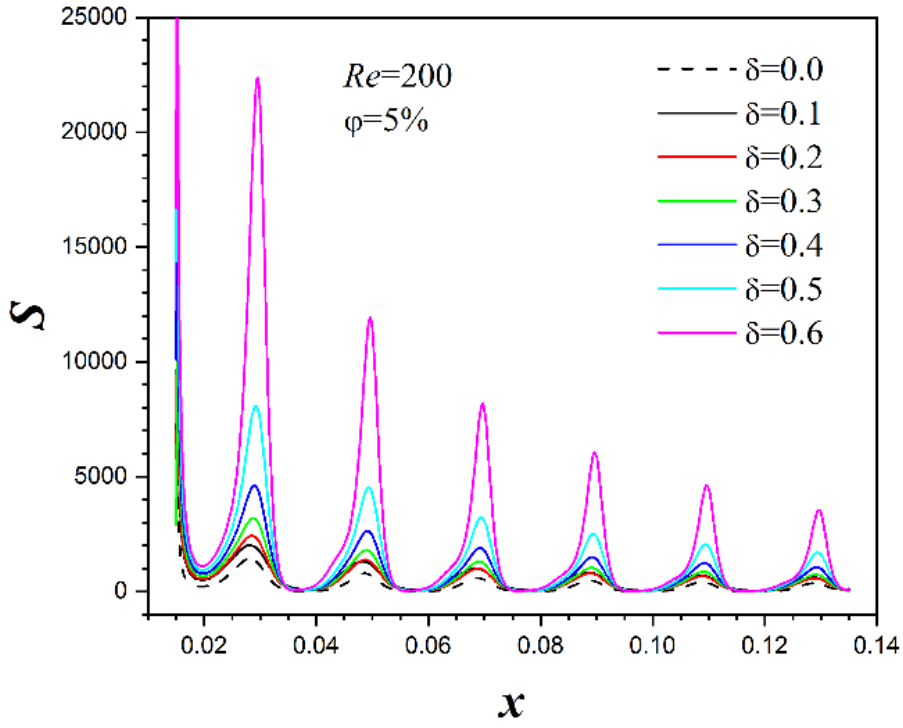


Figure 4.6A. Effect of porous insert thickness on local entropy generation.

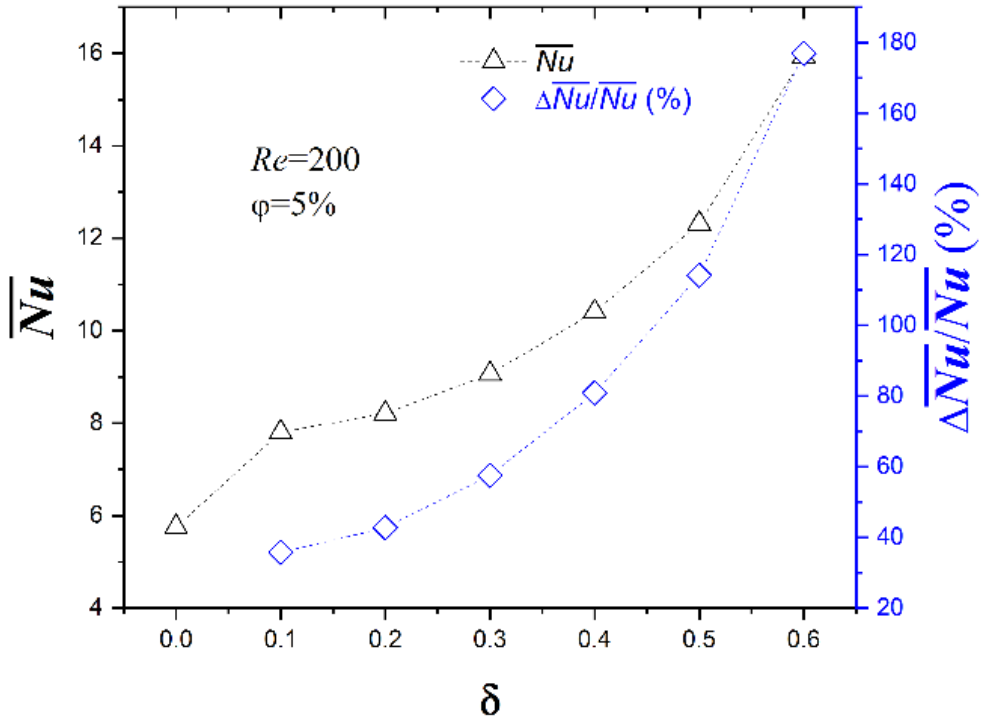


Figure 4.7A. Effect of porous insert thickness on the average Nusselt number.

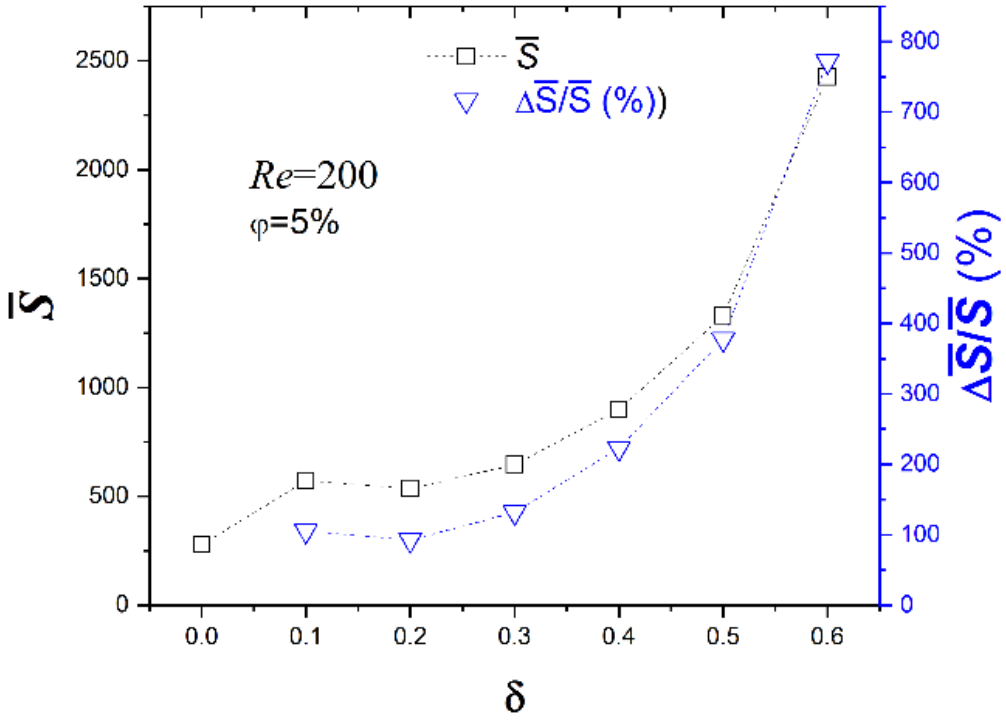


Figure 4.8A. Effect of porous insert thickness on the average entropy generation.

Figures 4.7A and 4.8A, along with Table 4.2A, illustrate the effect of δ on the average Nusselt number ($\overline{Nu}$) and average entropy generation ($\bar{S}$) at $Re = 200$ and $\varphi = 5\%$. As shown, for $\delta = 0.6$, $\overline{Nu}$ increases by approximately 180%, while $\bar{S}$ rises by 750% compared

to the empty channel. Increasing δ within the range 0.1–0.6 leads to enhancements in $\overline{Nu}$ from 35.7% to 176.9% and in $\bar{S}$ from 105.4% to 771.9%. This demonstrates the critical role of δ in controlling vortex formation and velocity magnitude, thereby significantly enhancing heat transfer.

Table 4.2A. Effect of δ on $\Delta\overline{Nu}/\overline{Nu}$ (%) and $\Delta\bar{S}/\bar{S}$ (%), with $Re = 200$ and $\varphi = 5\%$; the clear PCC is used as reference.

δ	Δ*Nu*/*Nu* (%)	Δ*S*/*S* (%)
0.1	35.72971	105.39973
0.2	42.75993	92.48842
0.3	57.58222	132.00703
0.4	80.86191	222.91157
0.5	114.1366	377.48438
0.6	176.94945	771.93213

4.5A Effect of Reynolds number on $\overline{Nu}$ and $\bar{S}$

Figures 4.9A–4.12A and Table 4.3A present the variations of the average Nusselt number ($\overline{Nu}$) and average entropy generation ($\bar{S}$) with Reynolds number for both the clear and porous channels at $\delta = 0.4$ and $\varphi = 5\%$. As shown, $\overline{Nu}$ and $\bar{S}$ increase with Reynolds number in an approximately linear manner, with a more pronounced effect in the porous channel than in the clear channel. Compared to the clear channel, at $Re = 200$, the porous channel exhibits increases of about 80.9% in $\overline{Nu}$ and 222.9% in $\bar{S}$. This enhancement becomes even more significant at higher Reynolds numbers; at $Re = 500$, $\overline{Nu}$ rises by approximately 108.4%, while $\bar{S}$ increases by around 309.15%.

Table 4.3A. Effect of Re on $\Delta\overline{Nu}/\overline{Nu}$ (%) and $\Delta\bar{S}/\bar{S}$ (%) for $\delta = 0.4$ and $\varphi = 5\%$, using the clear PCC channel as reference.

Re	Δ*Nu*/*Nu* (%)	Δ*S*/*S* (%)
200	80.86197	222.94186
300	88.45857	246.75594
400	99.20086	277.09579
500	108.37771	309.0967

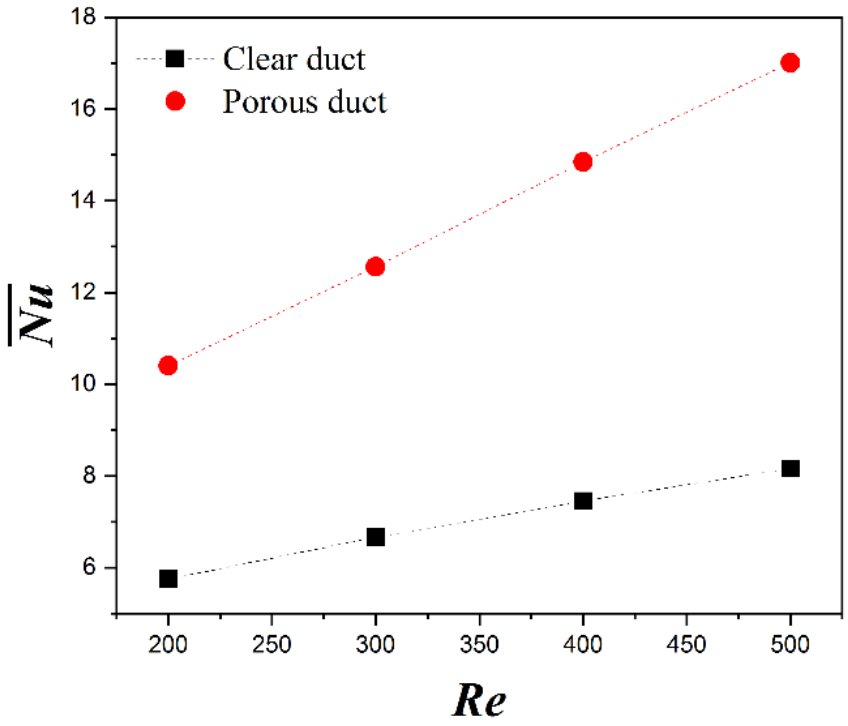


Figure 4.9A. Effect of Reynolds number on the average Nusselt number for clear and porous channels at $\delta = 0.4$ and $\varphi = 5\%$.

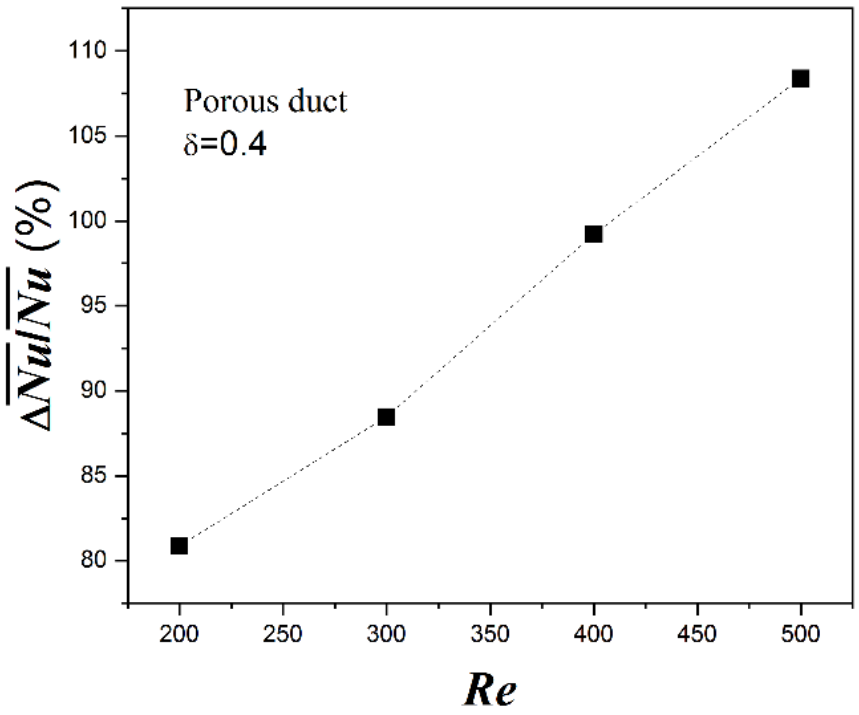


Figure 4.10A. Effect of Re on the rate of change of the average Nusselt number at φ = 5%.

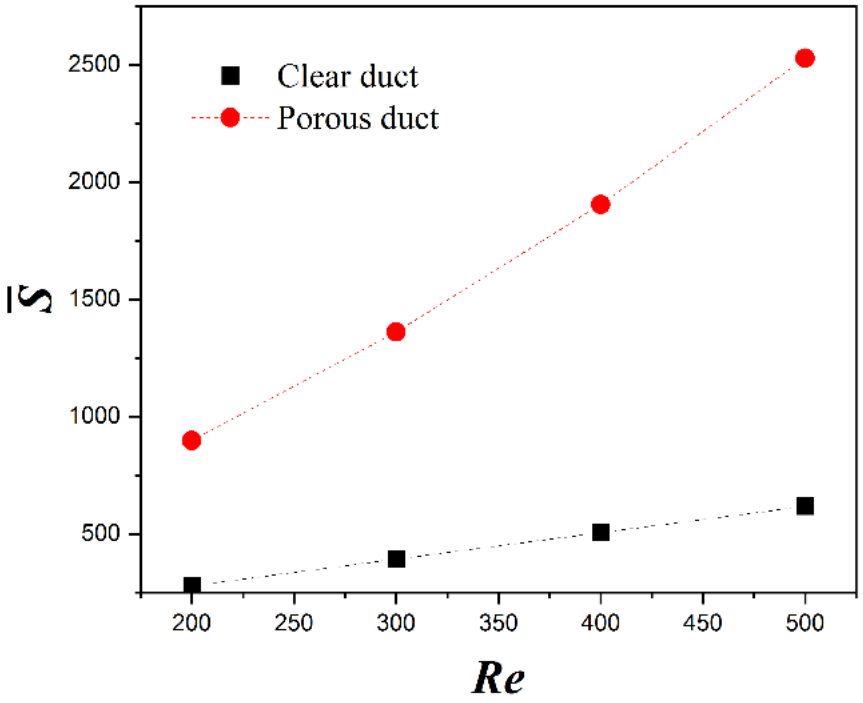


Figure 4.11A. Effect of the Reynolds number on the average entropy of clear and porous channels ($\varphi = 5\%$).

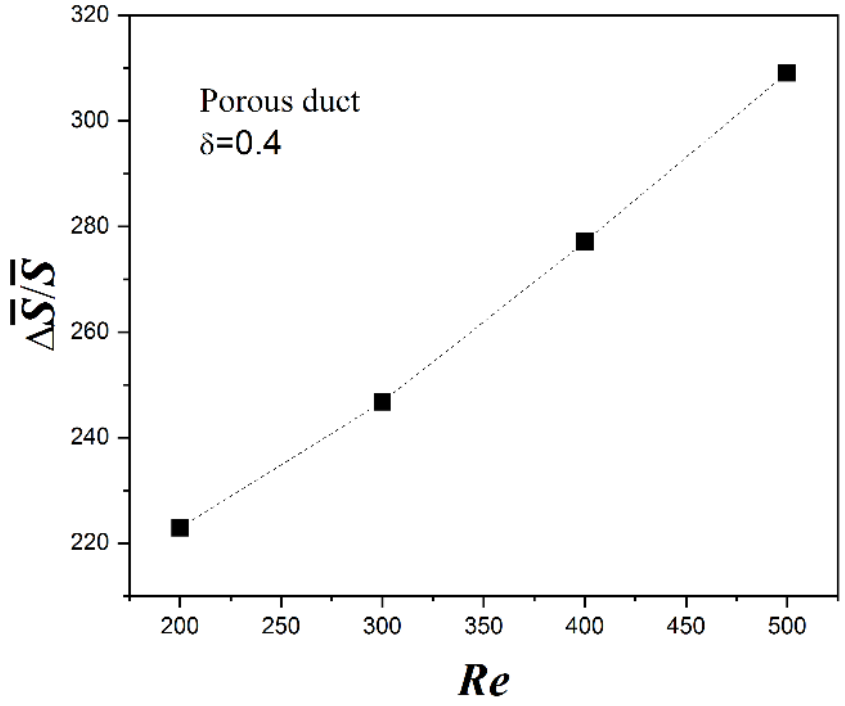


Figure 4.12A. Effect of the Reynolds number on the rate of change of the average entropy, $\varphi = 5\%$.

4.6A Effect of nanoparticle volume fraction on $\overline{Nu}$ and $\bar{S}$

Figures 4.13A–4.16A and Table 4.4A show the variations of the average Nusselt number ($\overline{Nu}$) and average entropy generation ($\bar{S}$) with nanoparticle volume fraction (φ) for both clear

and porous channels at $\delta = 0.4$ and $Re = 400$. As illustrated, both the heat transfer rate and entropy generation increase with increasing φ. This enhancement is attributed to the improved thermal conductivity of the nanofluid, which strengthens convective heat transfer. Consequently, the associated thermal irreversibility, reflected in entropy generation, also rises. Specifically, as φ increases from 0% to 5%, $\overline{Nu}$ increases by approximately 9%, while $\bar{S}$ rises by about 5.5%.

Table 4.4A. Effect of φ on $\Delta\overline{Nu}/\overline{Nu}$ (%) and $\Delta\bar{S}/\bar{S}$ (%) at $Re = 400$ for both porous and clear PCC channels.

	Porous channel (δ=0.4)		Clear channel	
φ	$\Delta Nu/Nu$ (%)	$\Delta Nu/Nu$ (%)	$\Delta S/S$ (%)	$\Delta S/S$ (%)
1%	1.92241	1.88095	1.38439	1.17491
3%	5.56499	5.6907	3.70613	3.42379
5%	9.01752	9.46675	5.55408	5.49631

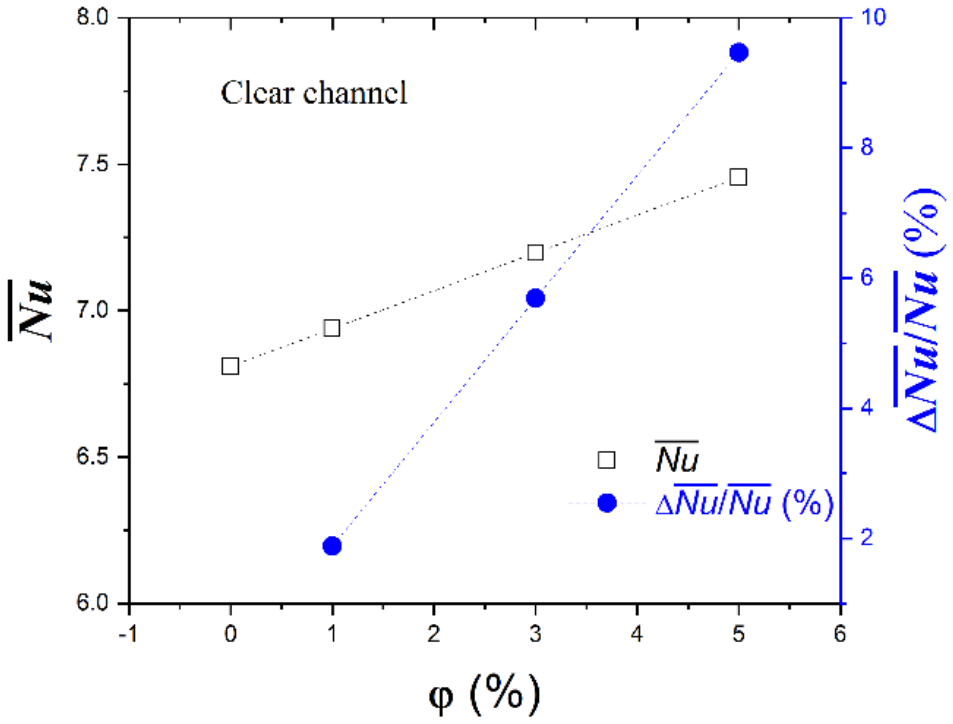


Figure 4.13A. Effect of the porosity φ on the mean Nusselt number of a clear channel for $\delta = 0.4$ and $Re = 400$.

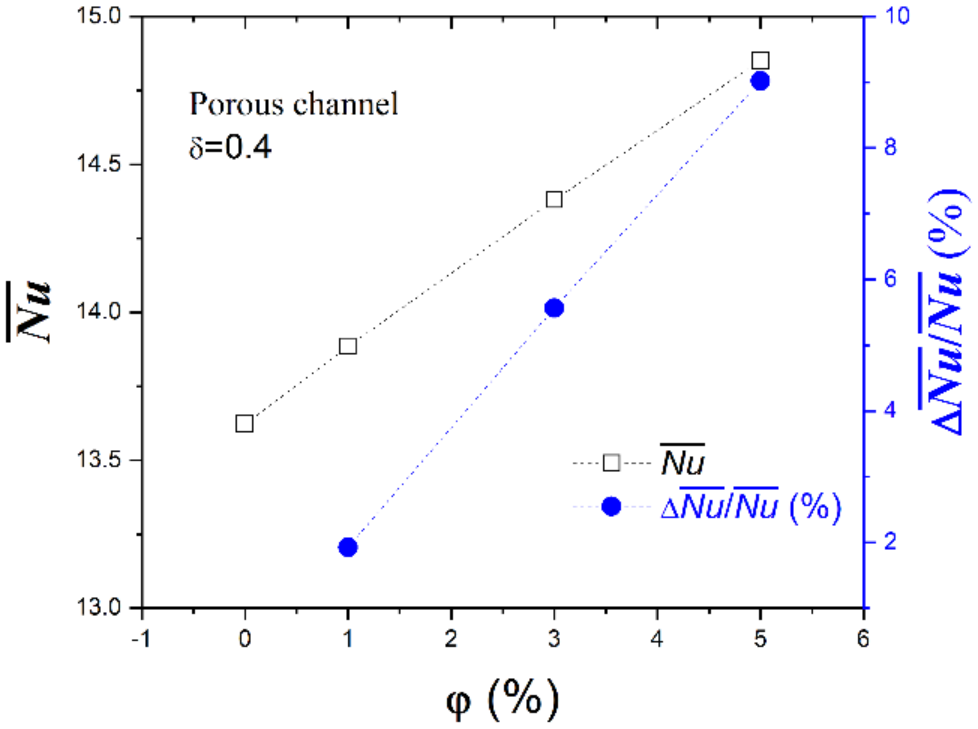


Figure 4.14A. Effect of the porosity φ on the mean Nusselt number of a porous channel for Re=400.

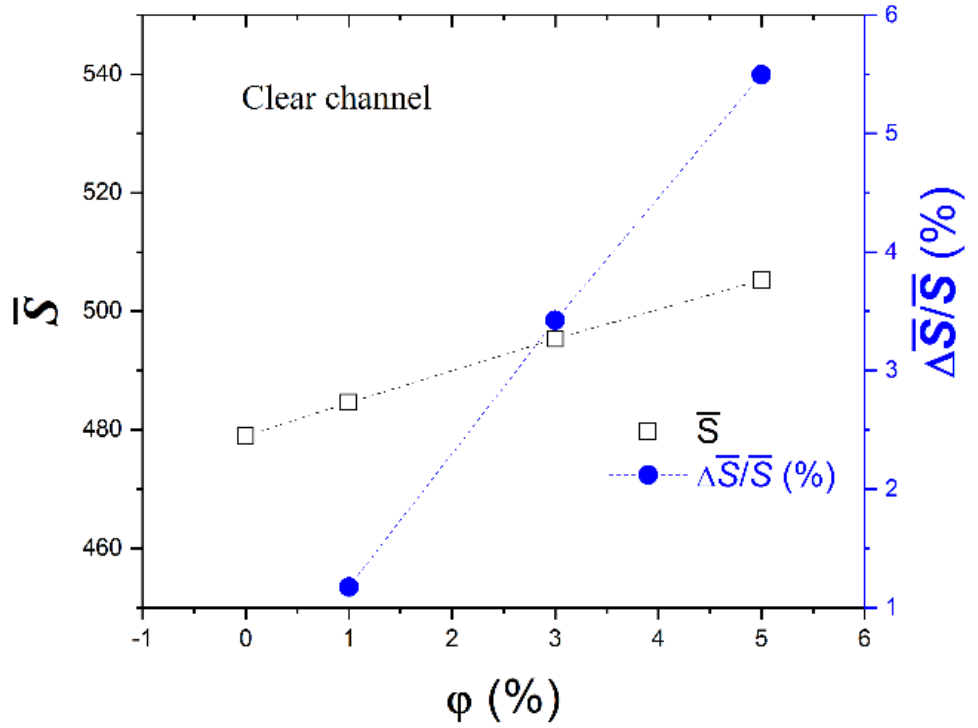


Figure 4.15A. Effect of the volume fraction on the mean entropy of a clear channel for $Re = 400$.

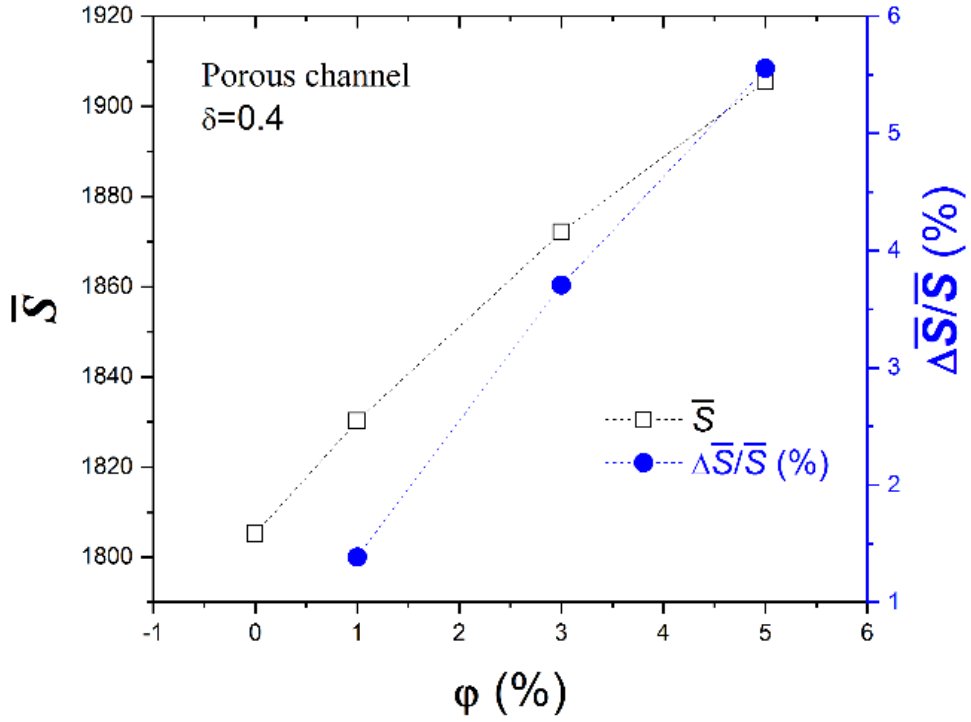


Figure 4.16A. Effect of the volume fraction on the mean entropy of a porous channel for $Re = 400$.

4.7A Conclusion

The simulations investigated the effects of porous layer thickness, Reynolds number, and nanoparticle volume fraction on the key parameters governing heat transfer in a corrugated channel with sinusoidal undulations of dimensionless amplitude 0.15 and dimensionless wavelength 2. Using CuO/water nanofluid and an AISI 304 porous layer, the main findings can be summarized as follows:

- Effect of porous insertion: The presence of a porous layer significantly enhances heat transfer and entropy generation. Both the average Nusselt number ($\overline{Nu}$) and average entropy generation ($\bar{S}$) increase almost linearly with δ. Compared to the clear channel ($\delta = 0$), for $\delta = 0.6$, $\overline{Nu}$ increases by 176.9% and $\bar{S}$ by 771.9%.
- Effect of Reynolds number: The influence of Reynolds number is more pronounced in a porous channel than in a clear channel. For $\delta = 0.4$ and $\varphi = 5\%$, at $Re = 500$, $\overline{Nu}$ increases by 108.4% and $\bar{S}$ by 309.1% relative to the clear channel.
- Effect of nanoparticle fraction: The volume fraction of nanoparticles has a similar effect in both clear and porous channels. For $\varphi = 5\%$, $\overline{Nu}$ increases by approximately 9% and $\bar{S}$ by about 5%.

These results highlight the critical role of porous layer thickness and flow conditions in enhancing heat transfer and controlling thermal irreversibility in wavy corrugated channels.

CHAPTER 4 (B):

HEAT TRANSFER IN A WAVY CHANNEL-POROUS METAL FOAM

4.1B Introduction

This section examines the influence of the porous layer thickness (δ) and Reynolds number (Re) on the key parameters governing nanofluid (NF) flow within the corrugated channel. The investigated parameters include velocity vector contours, velocity magnitude, streamlines, isotherm distributions, local and mean Nusselt numbers, entropy generation, relative Nusselt number and entropy, friction factor, and the performance evaluation criterion (PEC). The geometrical and physical characteristics of the wavy channel heat exchanger employed in the numerical simulations are summarized in Table 4.1B.

Table 4.1B. Characteristics of the wavy-channel heat exchanger used in numerical simulations

Dimensionless wave amplitude (α)	0.15
Dimensionless wavelength (λ)	2
Porous medium	Copper
Dimensionless porous insert thickness (δ)	0, 0.1, 0.2, 0.3, 0.4, 0.5
Base fluid	Water
Nanoparticles	Silver
Nanoparticles fraction φ (%)	5
Reynolds number (Re_D)	100,200, 300, 400

The dimensionless amplitude (α) and wavelength (λ) are fixed at 0.15 and 2, respectively. Six distinct wavy channel geometries are investigated, corresponding to different values of the dimensionless porous medium thickness ($\delta = 0$, 0.1, 0.2, 0.3, 0.4, and 0.5). The numerical simulations employ water as the base fluid, silver (Ag) nanoparticles, and copper (Cu) as the porous medium; the corresponding thermophysical properties are listed in Table 4.2B.

Table 4.2B. Physical properties of the materials used [50, 82]

	Material	ρ (kg.m^{-3})	c (J.kg^{-1}.K^{-1})	μ (Pa.s)	k (W.m^{-1}.K^{-1})
Base Fluid	water	998.2	4182.0	0.001003	0.6
Nanoparticles	Silver (Ag)	10490	236	-	429
Porous material	Copper (Cu)	8960	390	-	401

Furthermore, the effects of the Reynolds number are analyzed over the range $Re = 100-400$. Two types of porous medium layers are considered:

(1) a copper foam material with a porosity of 0.8 and a pore density of 10 PPI [45], for which the Calmidi correlation presented in Section 4 is employed to evaluate the metal foam properties;
(2) and (2) a packed granular porous medium, whose properties are determined using the correlations introduced in Chapter 2, namely correlation (2.39) for porosity and the Ergun equation (2.35) for permeability.

For the packed granular material, assuming a mean particle diameter significantly smaller than the channel height ($d/Hc < 0.1$), the porosity estimated from Eq. (2.39) is approximately 0.4. The corresponding parameters of the metal foam and packed granular media are summarized in Table 4.3B.

Table 4.3B. Characteristics of the porous material used

Material	Porosity ε	Pore density ω (PPI)	Permeability K (m^2)	Average fiber diamere d_f (m)	Average pore diameter d_{po} (m)
Metal foam	0.8	10	4.73×10^{-8}	0.44×10^{-3}	2.54×10^{-3}
Packed granular metal	0.373	-	2.19×10^{-10}	-	-

4.2B Effect of porous layer thickness on velocity vectors and streamlines

Figure 4.1B illustrates the velocity vector fields for different values of the porous layer thickness (δ) at $Re = 400$ and a nanoparticle volume fraction of $\varphi = 5\%$, for both packed granular and metal foam configurations.

The figure highlights the evolution of the velocity vectors at various locations along the channel. For $\delta = 0$ (clear channel), the velocity vectors attain their maximum magnitude along the channel centerline. However, the introduction of a porous insert in this region significantly attenuates the flow intensity. In addition, the velocity vectors are noticeably stronger in the converging sections of the channel compared to other regions.

For the packed granular medium, flow reversal occurs mainly in the diverging regions of the undulating walls. These reverse flows generate recirculation zones that locally disturb the flow field and significantly influence the temperature distribution.

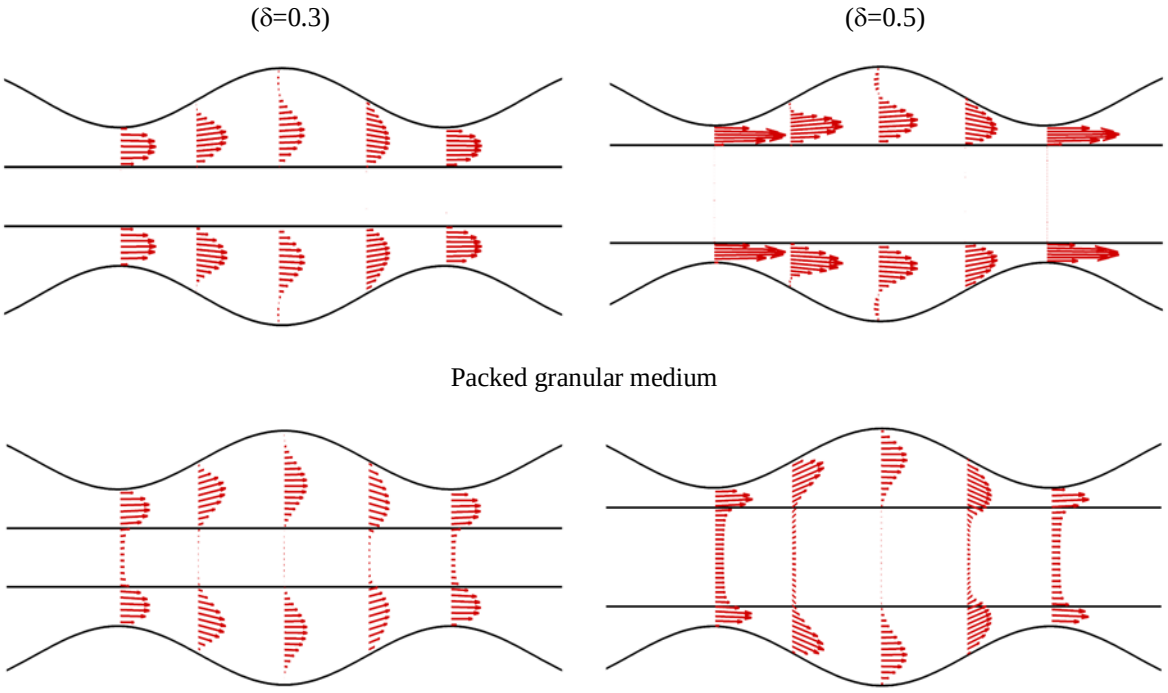


Figure 4.1B. Velocity vectors for $Re = 400$ and $\varphi = 5\%$.

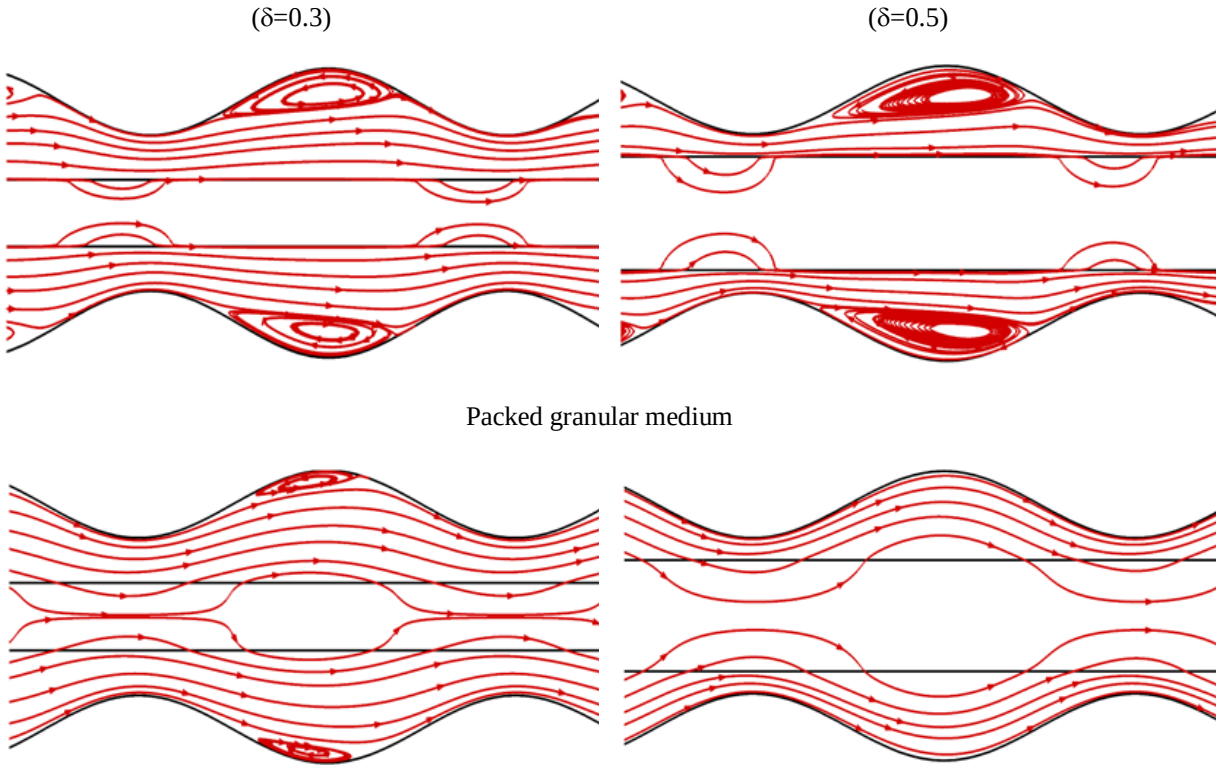


Figure 4.2B. Streamlines for $Re = 400$ and $\varphi = 5\%$.

Figure 4.2B presents the streamline patterns for various values of the porous layer thickness (δ) at $Re = 400$ and a nanoparticle volume fraction of $\varphi = 5\%$, for both packed granular and metal foam configurations. As shown, reverse flow develops within the diverging sections of the wavy walls in the packed granular channel. Moreover, increasing δ leads to an expansion of the recirculation zones, thereby intensifying disturbances in the flow structure. Such flow recirculation within the wavy sections strongly affects heat transfer characteristics, overall flow behavior, and entropy generation in the corrugated channel.

The main differences between the packed granular and metal foam media are localized in three distinct regions of the flow domain. Although the flow velocity within the porous region is generally low, it is more pronounced in the metal foam than in the packed granular medium. In the diverging sections of the wavy walls, flow reversal occurs predominantly in the packed granular medium. Conversely, in the converging regions, the flow velocity is higher for the packed granular medium compared to the metal foam.

4.3B Effect of porous layer thickness on velocity magnitude and isotherms

Figure 4.3B presents the velocity magnitude distributions for different values of the porous layer thickness (δ) at $Re = 400$ and a nanoparticle volume fraction of $\varphi = 5\%$, for both packed granular and metal foam configurations.

The figure reveals two high-velocity bands located near the lower and upper boundaries of the porous insert. For $\delta = 0$ (clear channel), these bands are uniformly distributed. Higher velocities are observed in the converging sections of the wavy walls. Increasing δ intensifies the velocity within these high-speed bands. In the packed granular medium, low-velocity regions appear in the diverging sections of the wavy wall due to flow recirculation. In contrast, the elevated velocities in the converging sections arise from flow acceleration associated with velocity compensation caused by fluid deceleration within the porous zone.

Figure 4.4B depicts the isotherm contours for various values of the porous layer thickness (δ) at $Re = 400$ and a nanoparticle volume fraction of $\varphi = 5\%$.

The results indicate a reduction in the thermal boundary layer thickness as the porous layer becomes thicker. Increasing δ enhances fluid flow in the clear region, leading to denser isotherms along the undulating walls and, consequently, higher temperature gradients. In the packed granular medium, the fluid temperature is higher in the diverging sections of the wavy walls than in the converging regions. This behavior is attributed to vortex formation, which induces local flow reversal in these zones.

4.4B Porous layer thickness impact on Nusselt number and entropy

Figures 4.5B and 4.6B illustrate the effect of the porous layer thickness (δ) on the local Nusselt number (Nu) and entropy generation (S) along the heated channel at $Re = 400$ and a nanoparticle volume fraction of $\varphi = 5\%$, for the clear channel, packed granular, and metal foam configurations.

The results show that both Nu and S reach their maximum values in the converging sections of the channel and are minimized in the diverging regions. In addition, Nu and S in the converging sections increase with increasing δ, indicating an enhanced heat transfer rate in these areas. This behavior is associated with a reduction in the thermal boundary layer thickness, which promotes more effective heat transfer. Furthermore, it is observed that, in a straight channel, both the Nusselt number and entropy generation attain their highest values near the inlet and gradually decrease along the channel length.

Table 4.4B. Effect of δ on $\Delta\overline{Nu}/\overline{Nu}$, $\Delta\bar{S}/\bar{S}$, and $\Delta\bar{f}/\bar{f}$ for $Re = 400$, $\varphi = 5\%$, using the clear wavy channel as reference

δ	Packed granular medium			Foam medium		
	$\Delta Nu/Nu$ (%)	$\Delta S/S$ (%)	$\Delta f/f$ (%)	$\Delta Nu/Nu$ (%)	$\Delta S/S$ (%)	$\Delta f/f$ (%)
0.2	43.03979	97.68197	83.94442218	36.18772	70.83366	80.52977475
0.3	58.08636	138.27155	90.69389013	51.16389	94.61269	87.90524316
0.4	91.18911	254.21243	95.43633631	73.90894	143.2935	92.92844474
0.5	134.64137	437.06005	98.27141621	94.52679	197.90102	95.98483136

Packed medium Foam medium

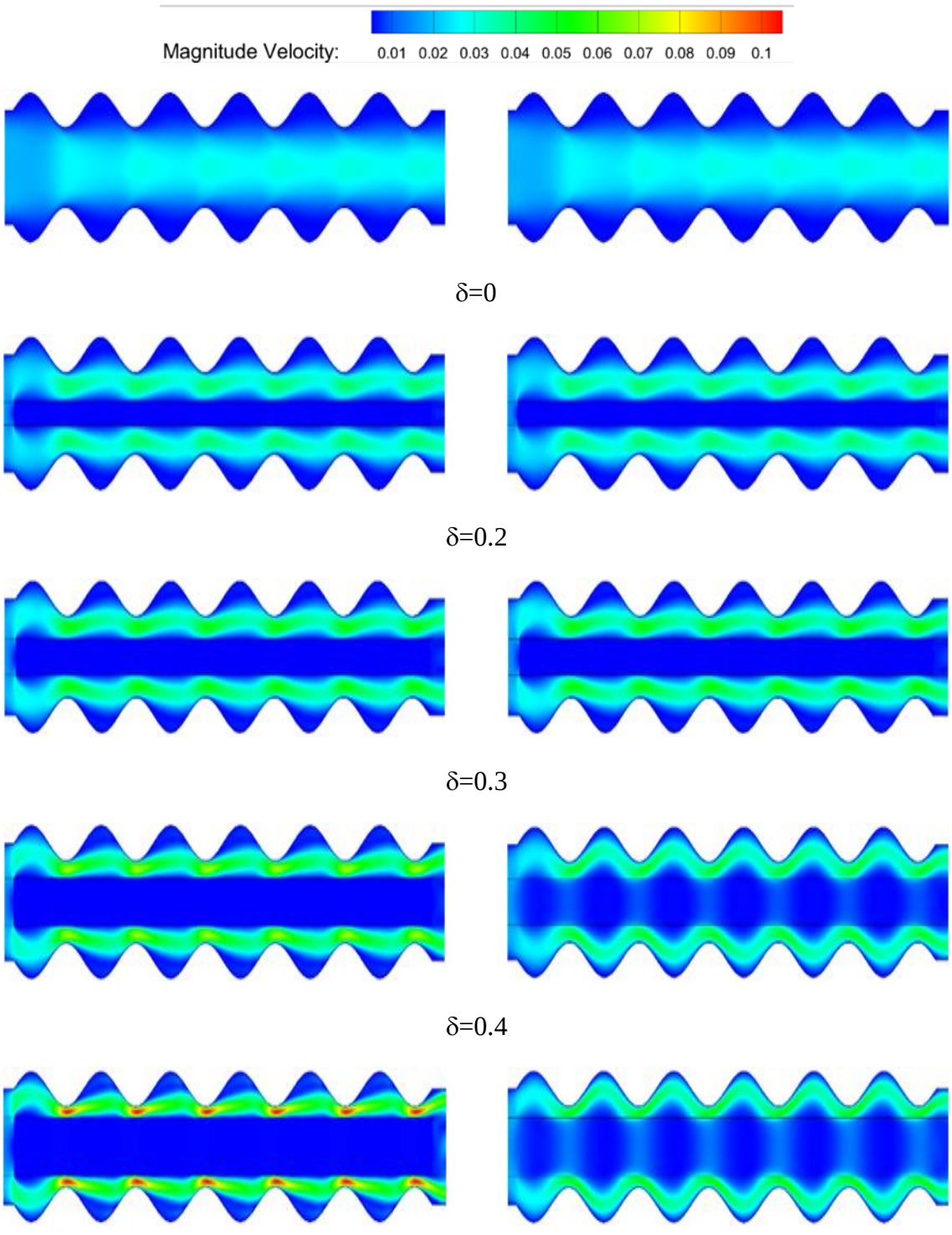


Figure 4.3B. Effect of δ on the velocity magnitude for $Re = 400$ and $\varphi = 5\%$.

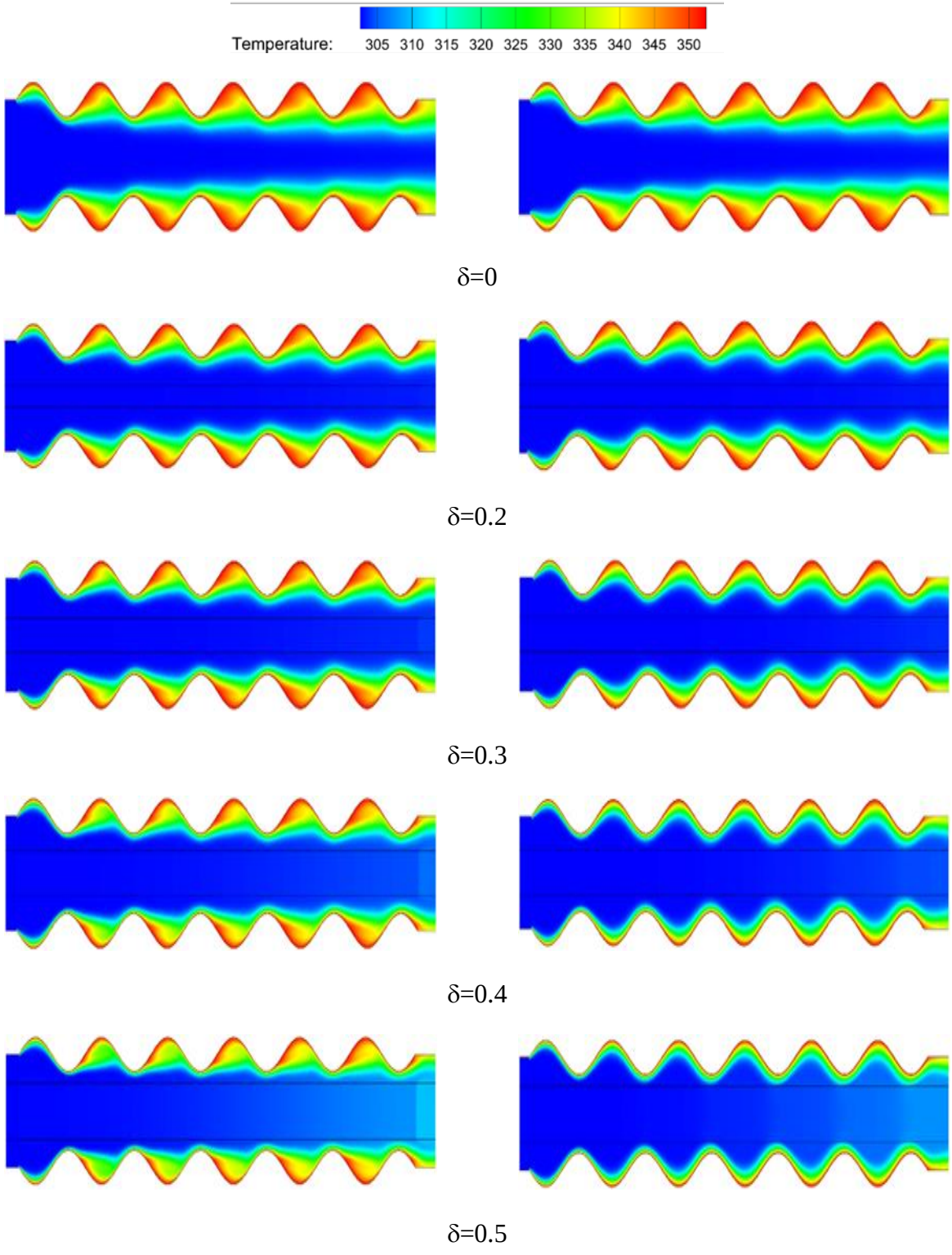


Figure 4.4B. Effect of δ on the isotherms for $Re = 400$ and $\varphi = 5\%$.

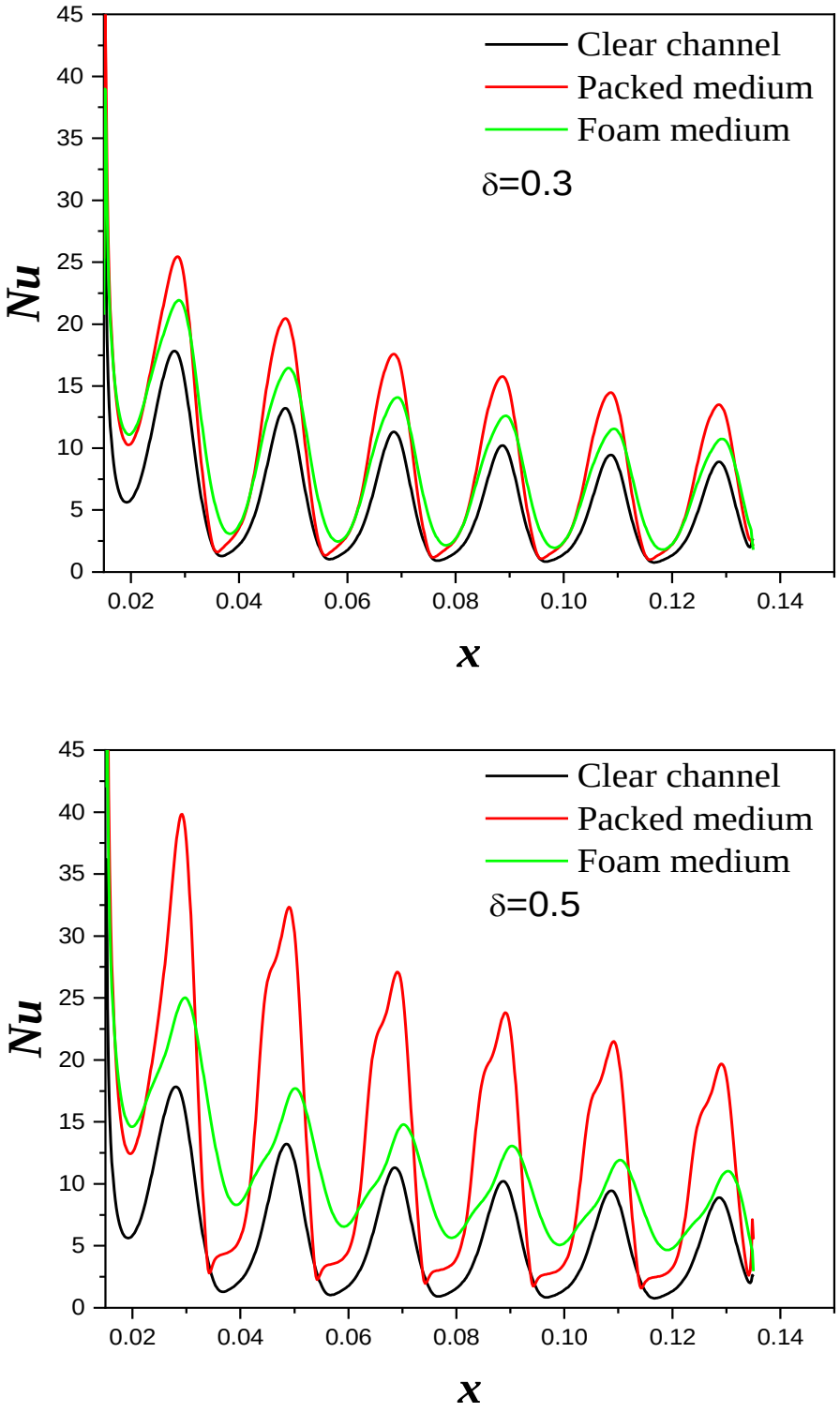


Figure 4.5B. Effect of δ on the local Nusselt number for $Re = 400$.

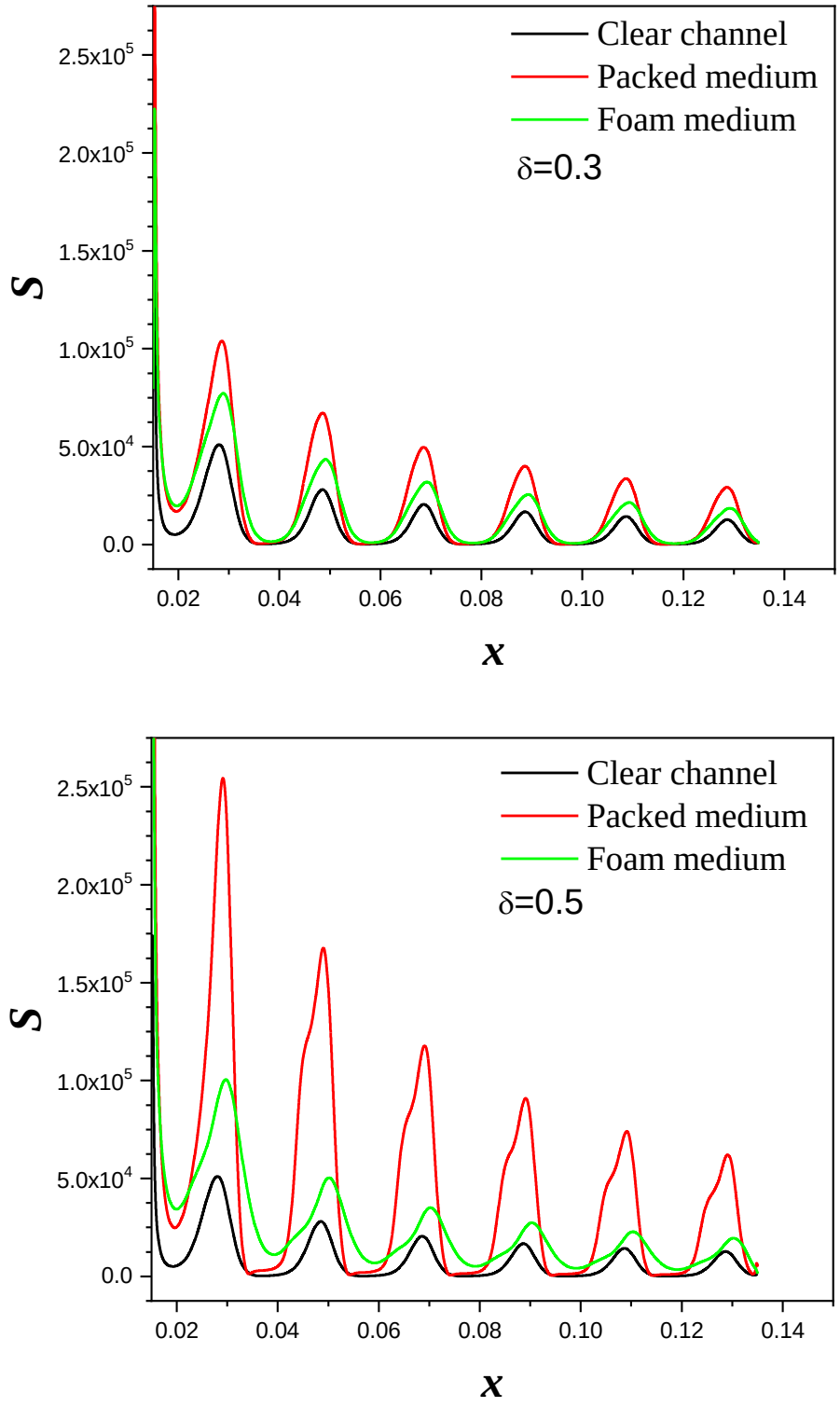


Figure 4.6B. Effect of δ on the local entropy for $Re = 400$.

Figures 4.7B, 4.8B, and 4.9B, together with Table 4.4B, illustrate the effect of the porous layer thickness (δ) on the mean Nusselt number ($\overline{Nu}$), mean entropy generation ($\bar{S}$), and friction factor ($\bar{f}$) at $Re = 400$ and a nanoparticle volume fraction of $\varphi = 5\%$. The results indicate that, for the packed granular medium with $\delta = 0.5$, the average Nusselt number increases by approximately 134.64%, while the entropy generation and friction factor rise by 437.06% and 98.27%, respectively, compared with the clear channel. As δ increases from 0.2 to 0.5, $\overline{Nu}$ is enhanced by 43.04% to 134.64%, entropy generation increases from 97.68% to 437.06%, and the friction factor rises from 83.94% to 98.27%. These findings highlight the critical role of δ in controlling vortex formation and velocity magnitude, thereby intensifying heat transfer. In contrast, the relatively lower values of $\overline{Nu}$, $\bar{S}$, and $\bar{f}$ observed for the metal foam medium are attributed to its higher permeability, which suppresses vortex formation and reduces the flow velocity near the corrugated walls.

4.5B Effect of Reynolds number on velocity magnitude and isotherms

the velocity magnitude distributions for different Reynolds numbers at $\delta = 0.5$ and $\varphi = 5\%$, for both packed granular and metal foam media. The figure reveals two high-velocity bands located near the lower and upper boundaries of the porous insert. Elevated velocities are observed in the converging sections of the wavy wall, and increasing Re further intensifies the velocity within these high-speed regions. In the packed granular medium, low velocities occur in the diverging sections due to flow recirculation, whereas the high velocities in the converging sections arise from flow acceleration associated with velocity compensation caused by fluid deceleration within the porous zone. In contrast, the metal foam medium exhibits a more uniform velocity distribution due to its higher permeability.

Figure 4.11B presents the isotherm contours for different Reynolds numbers at $\delta = 0.5$ and $\varphi = 5\%$. The results indicate that increasing Re reduces the thickness of the thermal boundary layer. Higher Re also enhances fluid flow in the clear region, leading to denser isotherms along the undulating walls and consequently higher temperature gradients. In the packed granular medium, the fluid temperature is elevated in the diverging sections of the wavy walls compared to the converging regions, owing to vortex formation that induces local reverse flow.

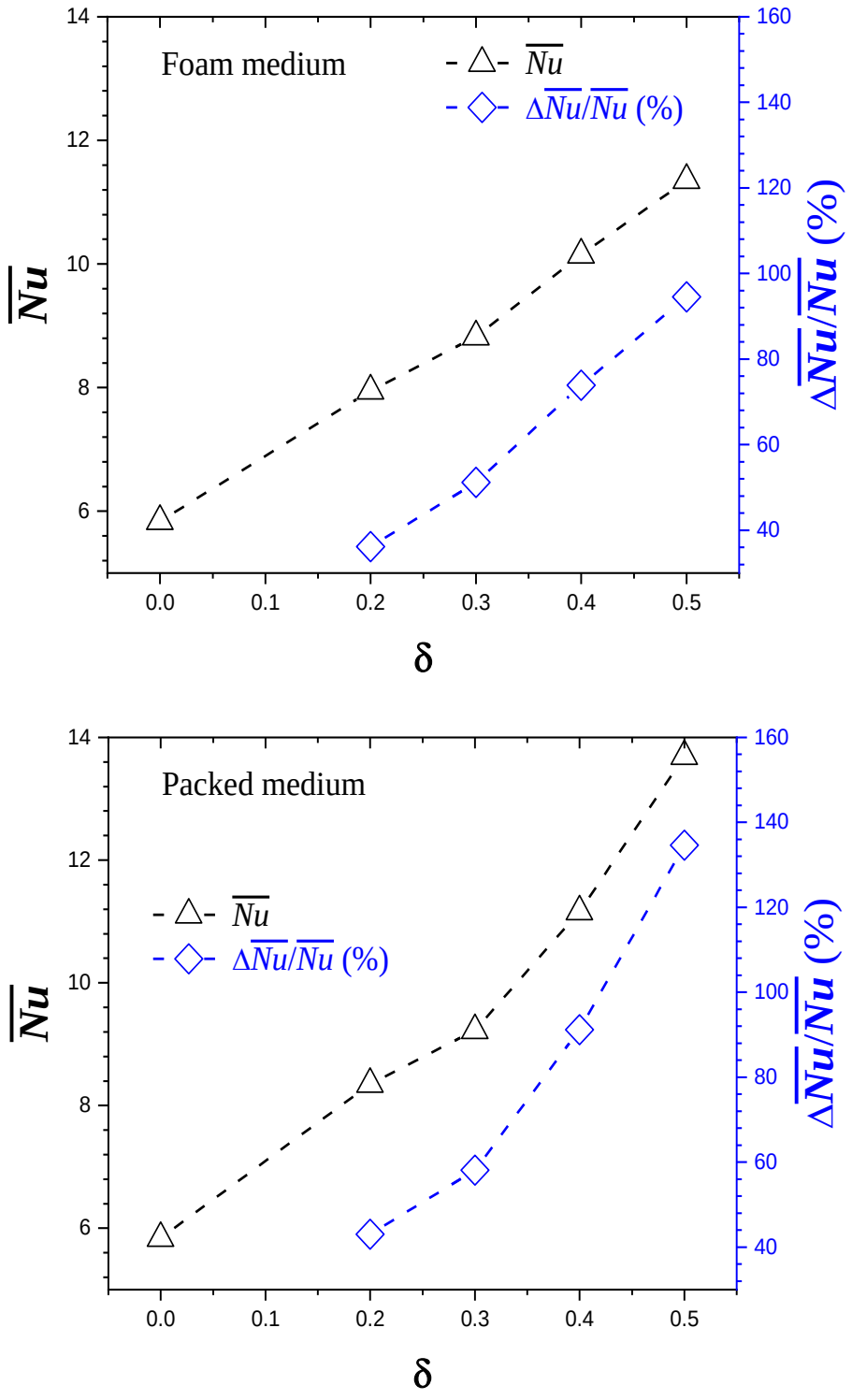


Figure 4.7B. Effect of δ on the average Nusselt number for $Re = 400$ and $\varphi = 5\%$.

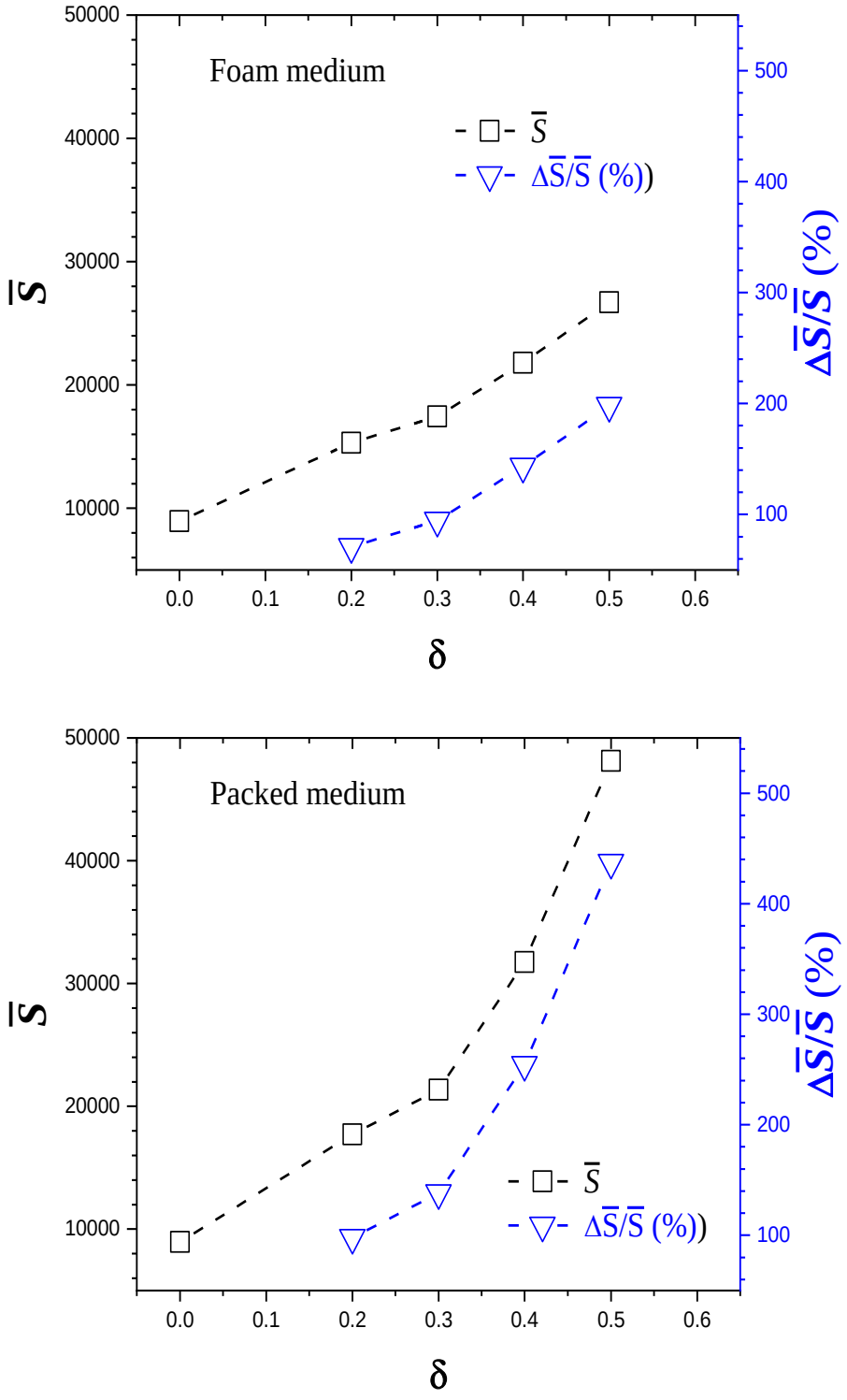


Figure 4.8B. Effect of δ on the average entropy for $Re = 400$ and $\varphi = 5\%$.

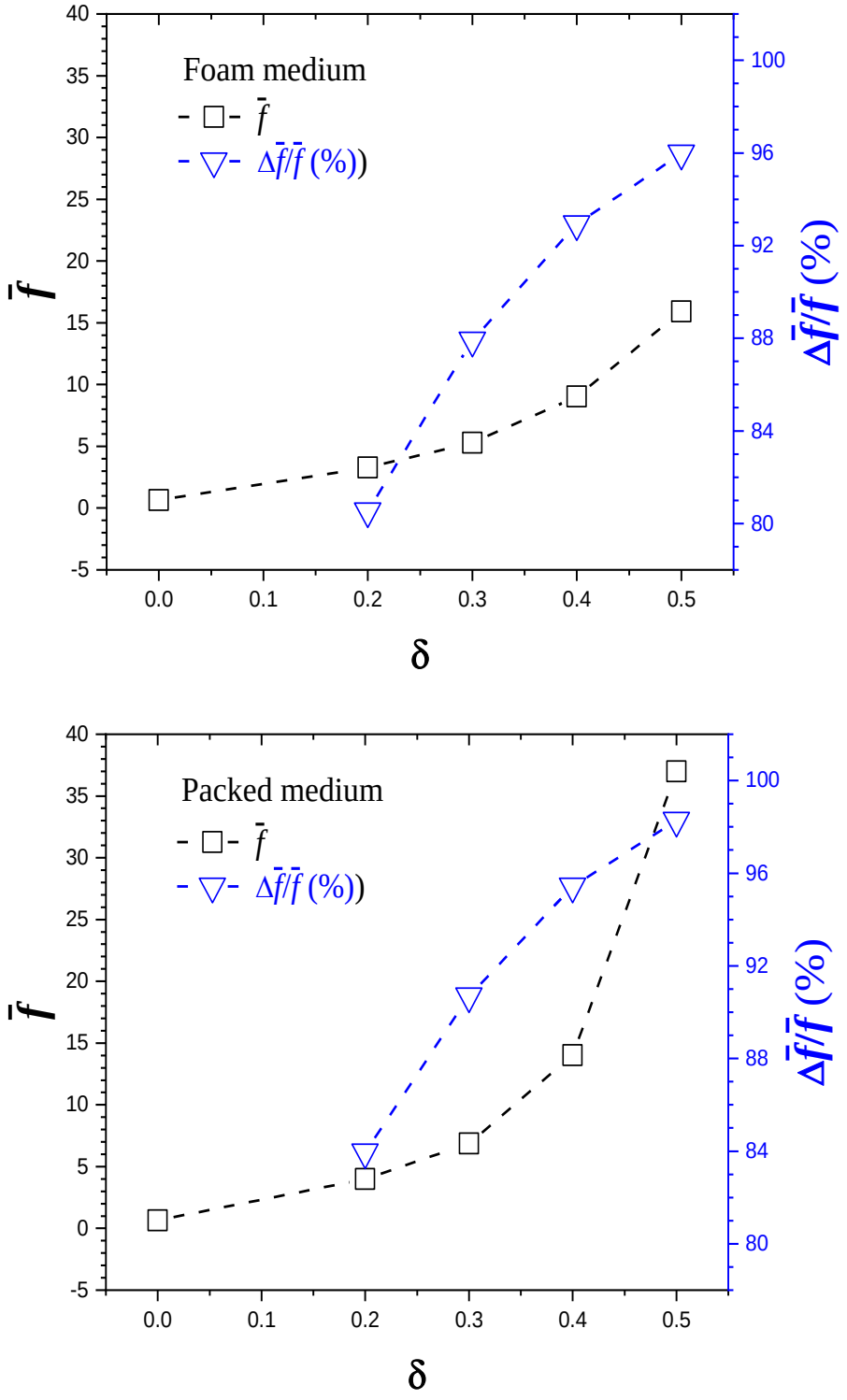
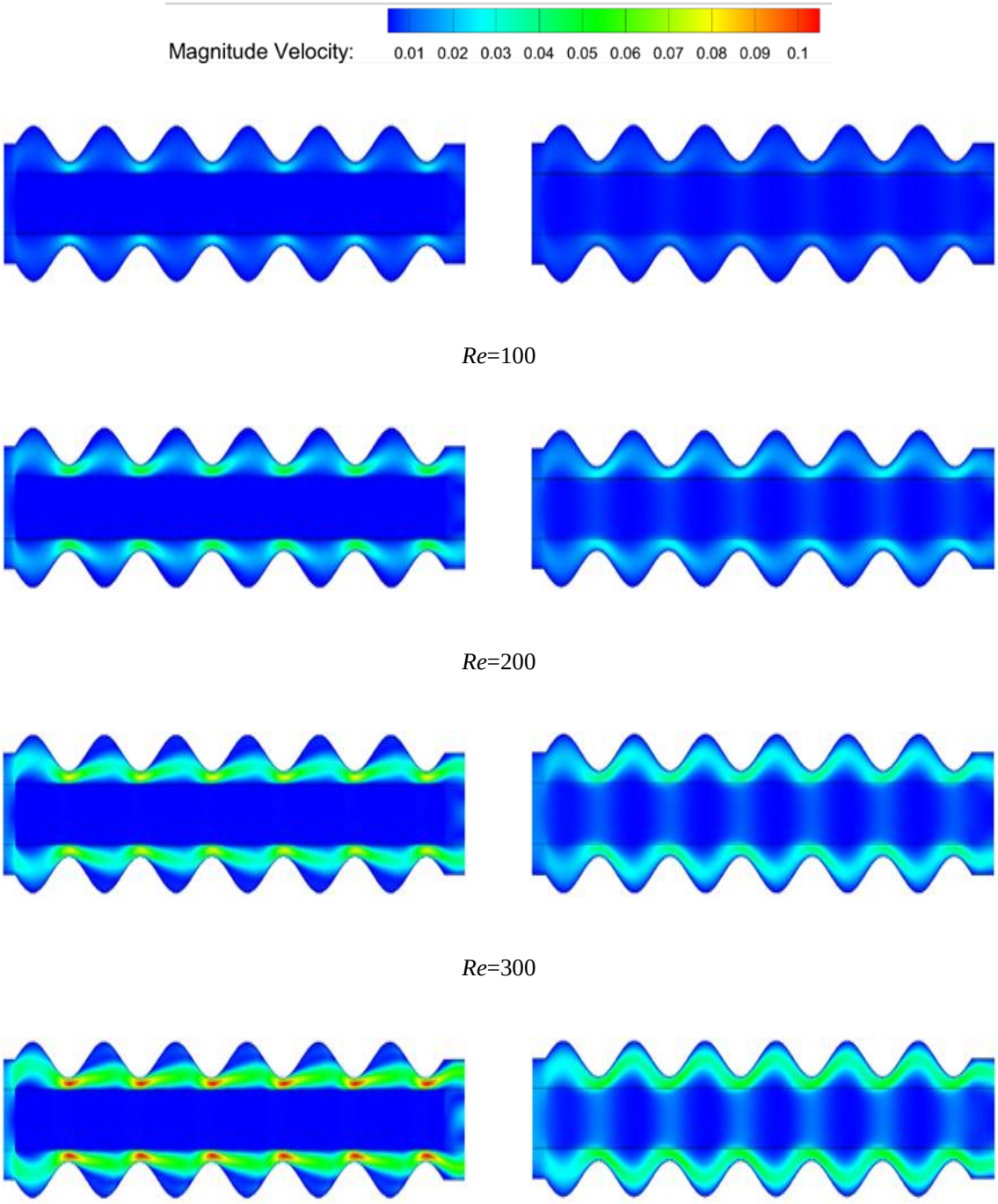


Figure 4.9B. Effect of δ on the average friction factor for $Re = 400$ and $\varphi = 5\%$.

Packed medium Foam medium



Re=100

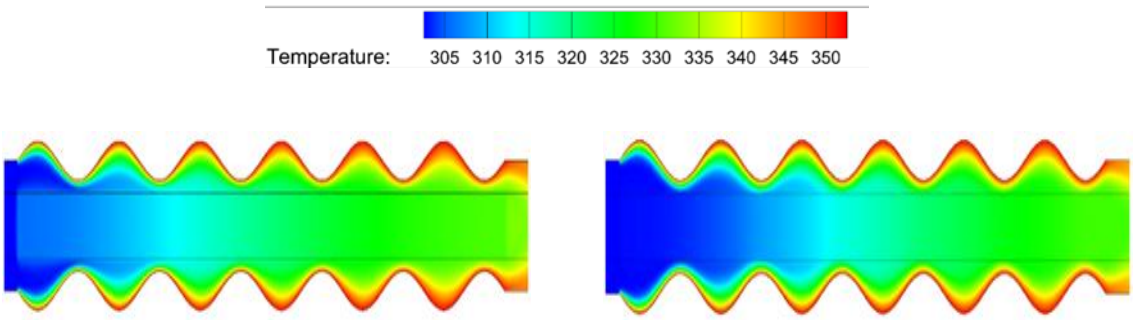
Re=200

Re=300

Re=400

Figure 4.10B. Effect of the Reynolds number on the velocity magnitude.

Packed medium Foam medium



Re=100

Re=200

Re=300

Re=400

Figure 4.11B. Effect of the Reynolds number on the isotherms.

4.6B Impact of Reynolds number on $\overline{Nu}$, $\bar{S}$, and $\bar{f}$

Figures 4.12B, 4.13B, 4.14B, and Table 4.5B illustrate the variations of the mean Nusselt number ($\overline{Nu}$), mean entropy generation ($\bar{S}$), and friction factor ($\bar{f}$) with Reynolds number at $\delta = 0.5$ and $\varphi = 5\%$. As shown, all three parameters increase with Re, with the effect being more pronounced for the packed granular medium compared to the metal foam and clear channels. At $Re = 400$, $\overline{Nu}$, $\bar{S}$, and $\bar{f}$ for the packed granular channel are approximately 134.8%, 447%, and 98.3% higher, respectively, than those of the clear duct. For the metal foam, the corresponding increases are comparatively lower. These results highlight that the influence of porous medium thickness on heat transfer enhancement becomes increasingly significant at higher Reynolds numbers.

Table 4.5B. Effect of Re on $\Delta\overline{Nu}/\overline{Nu}$, $\Delta\bar{S}/\bar{S}$, and $\Delta\bar{f}/\bar{f}$ for $\delta = 0.5$, $\varphi = 5\%$, using the clear wavy channel as reference

Re	Packed granular medium			Foam medium		
	Δ*Nu*/*Nu* (%)	Δ*S*/*S* (%)	Δ*f*/*f* (%)	Δ*Nu*/*Nu* (%)	Δ*S*/*S* (%)	Δ*f*/*f* (%)
100	83.50042	297.07256	98.49355	67.41229	193.98238	96.73478
200	106.92949	342.43633	98.35103	84.55595	209.24868	96.45018
300	119.47924	391.08676	98.27654	91.29136	204.80633	96.21765
400	134.8214	447.03199	98.27139	94.67604	203.43234	95.98477

4.7B Effect of porous layer thickness and Reynolds number on the *PEC*

Figures 4.15B and 4.16B examine the effects of the porous layer thickness (δ) and Reynolds number (Re) on the performance evaluation criterion (PEC). Three configurations of the wavy channel are considered: the clear wavy channel (CWC), the foam wavy channel (FWC), and the packed granular wavy channel (PGWC). For the clear wavy channel, increasing Re slightly reduces the PEC, which remains close to unity. In contrast, for the wavy porous channels, δ and Re influence PEC differently: PEC decreases with increasing δ and increases with Re. Within the investigated ranges of δ and Re, the PEC of the foam channel is higher than that of the packed granular medium. For $\delta \leq 0.2$, PEC values are nearly identical for both porous foam and granular channels, indicating that the influence of porous medium structure on PEC becomes significant only for $\delta > 0.2$. Across the investigated ranges of δ (0–0.5) and Re (100–400), PEC values vary between 0.46 and 0.73.

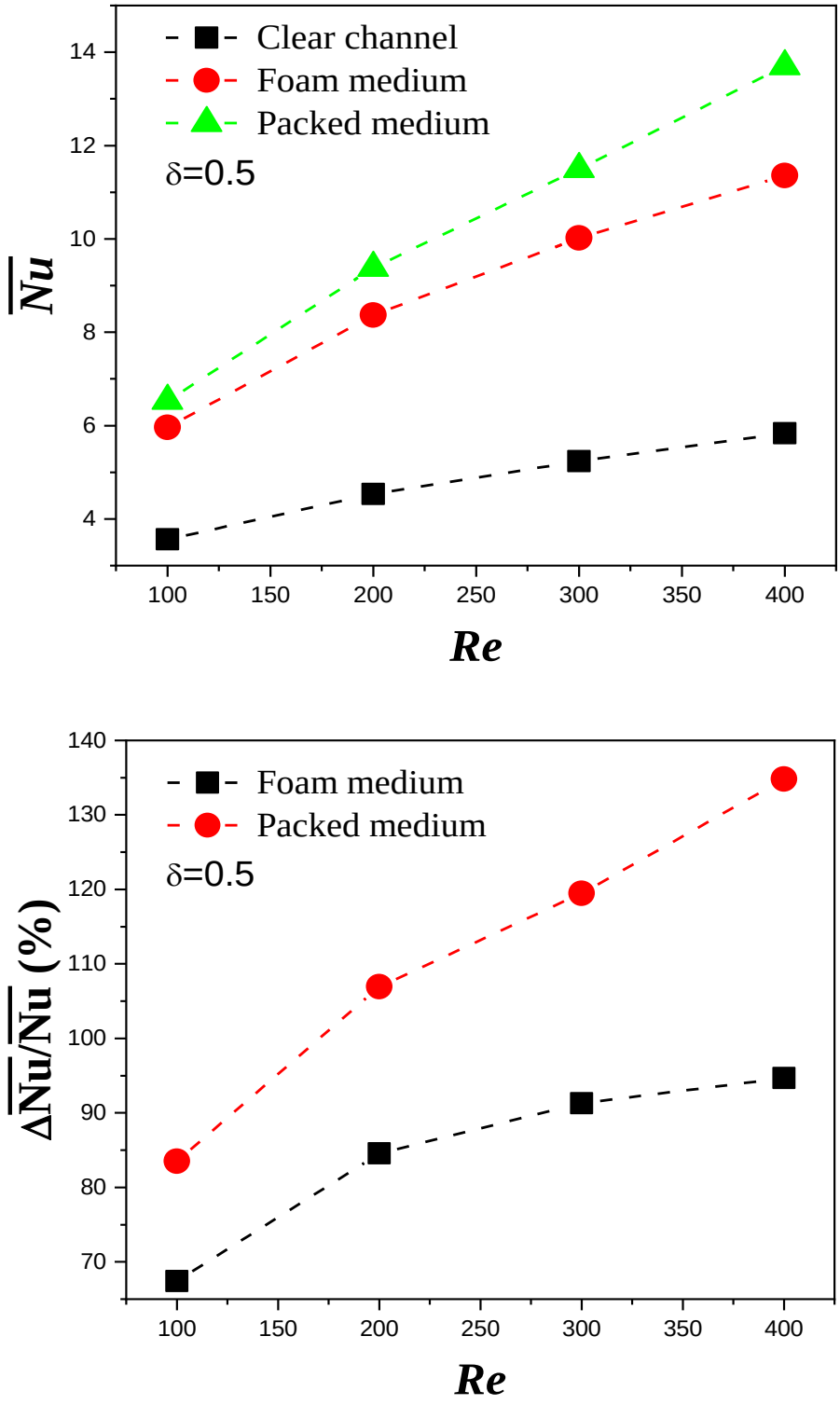
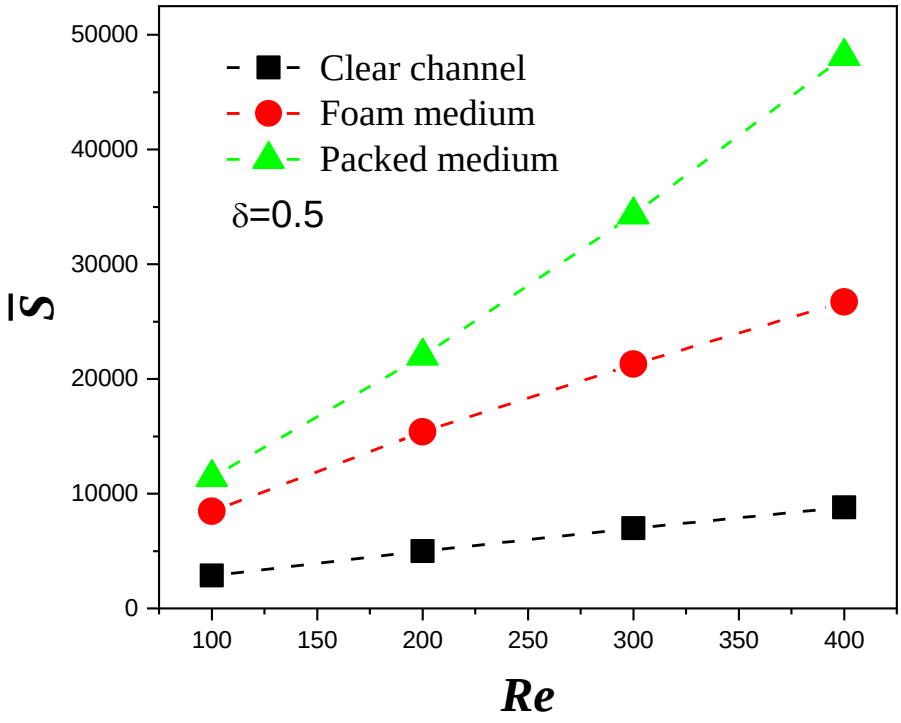


Figure 4.12B. Effect of the Reynolds number on the average Nusselt number for $\delta = 0.5$ and $\varphi = 5\%$.



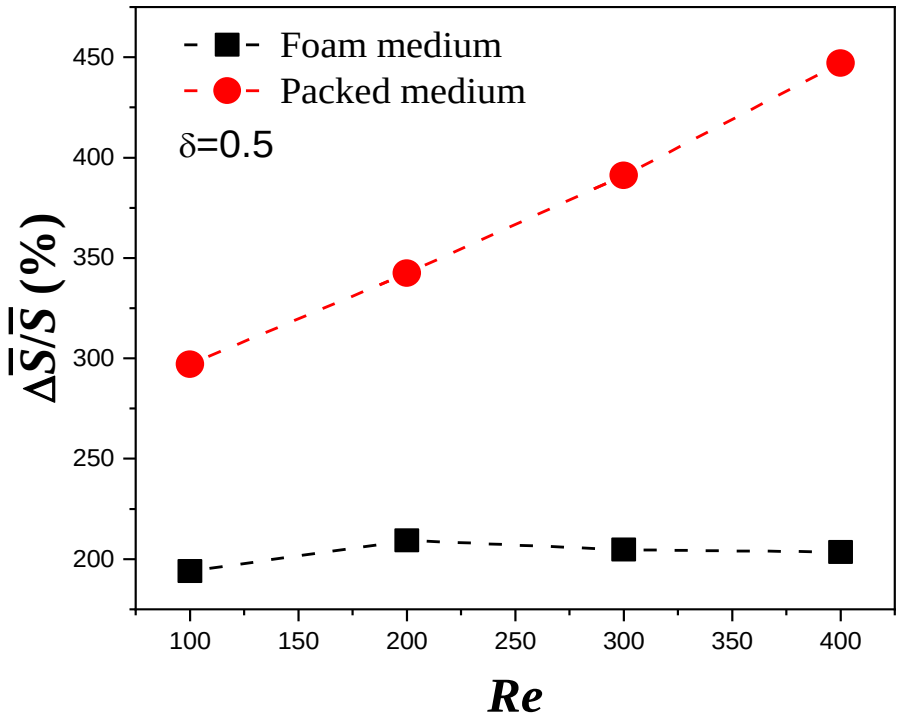


Figure 4.13B. Effect of the Reynolds number on the average entropy for $\delta = 0.5$ and $\varphi = 5\%$.

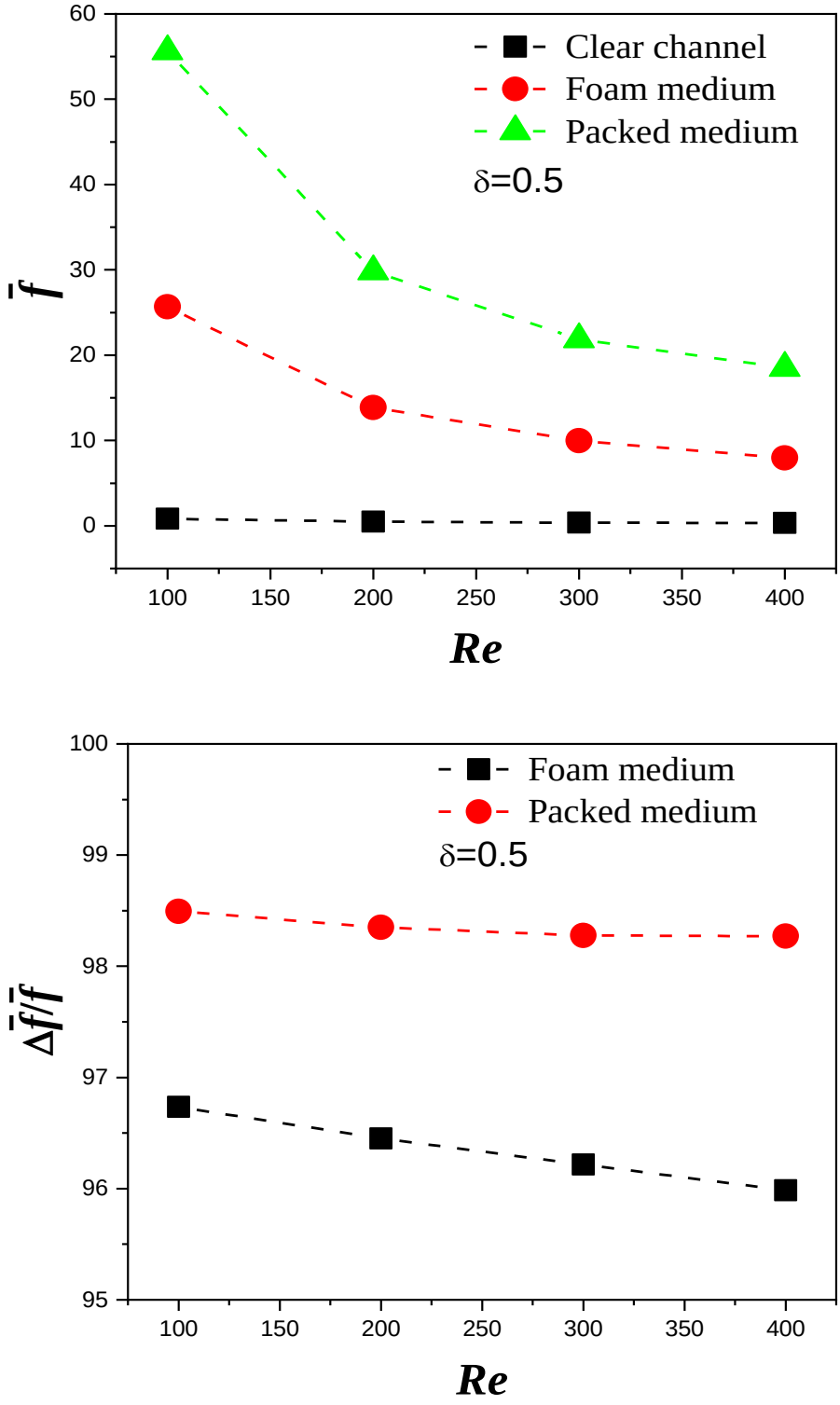


Figure 4.14B. Effect of the Reynolds number on the average friction factor for $\delta = 0.5$ and $\varphi = 5\%$.

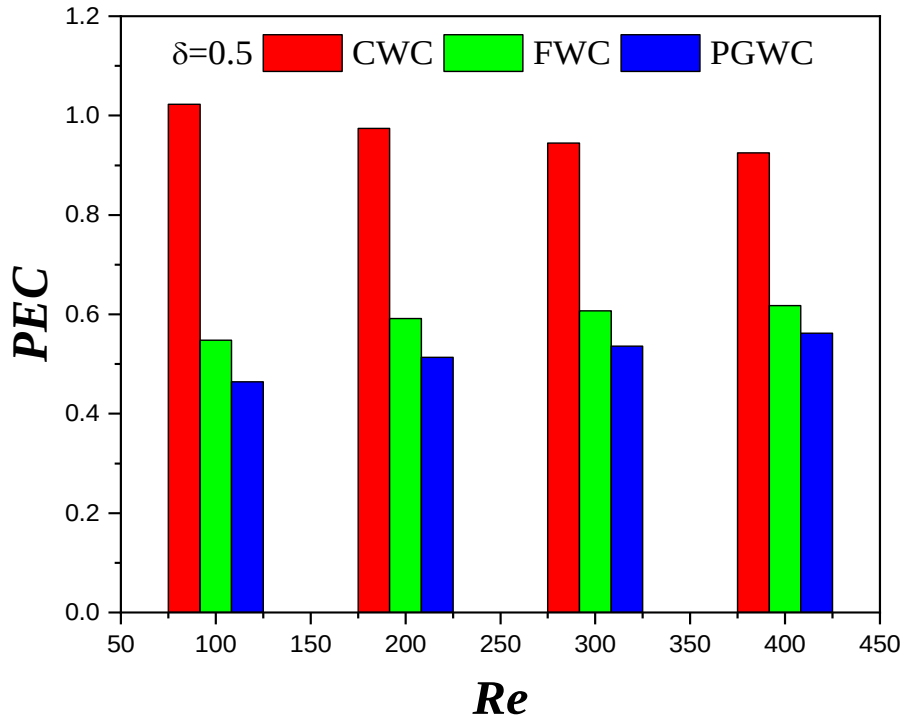


Figure 4.15. Effect of the Reynolds number on the performance evaluation criteria.

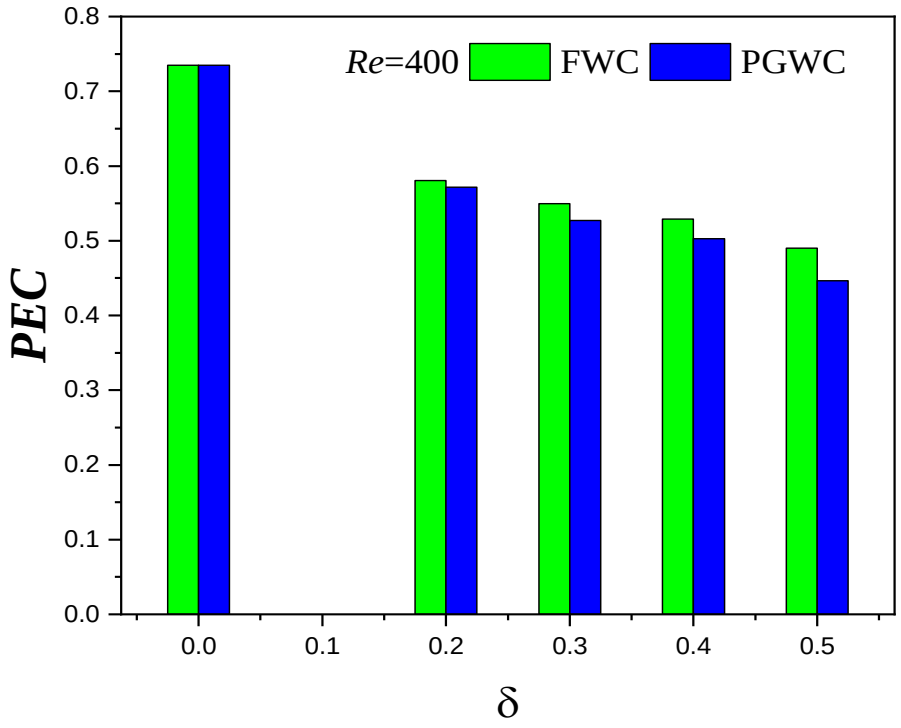


Figure 4.16B. Effect of δ on the performance evaluation criteria.

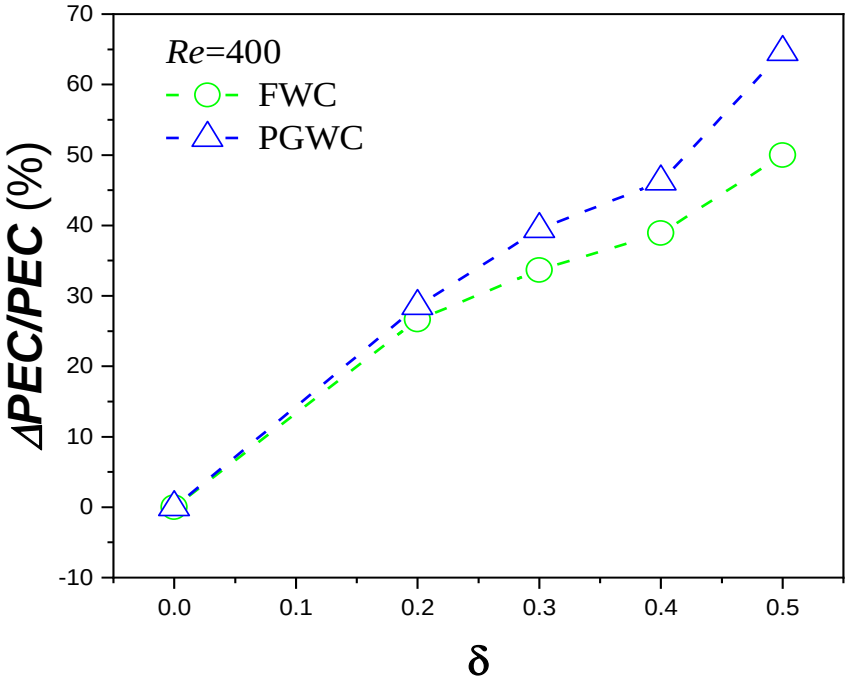


Figure 4.17B. Effect of δ on the relative gap of the performance evaluation criteria.

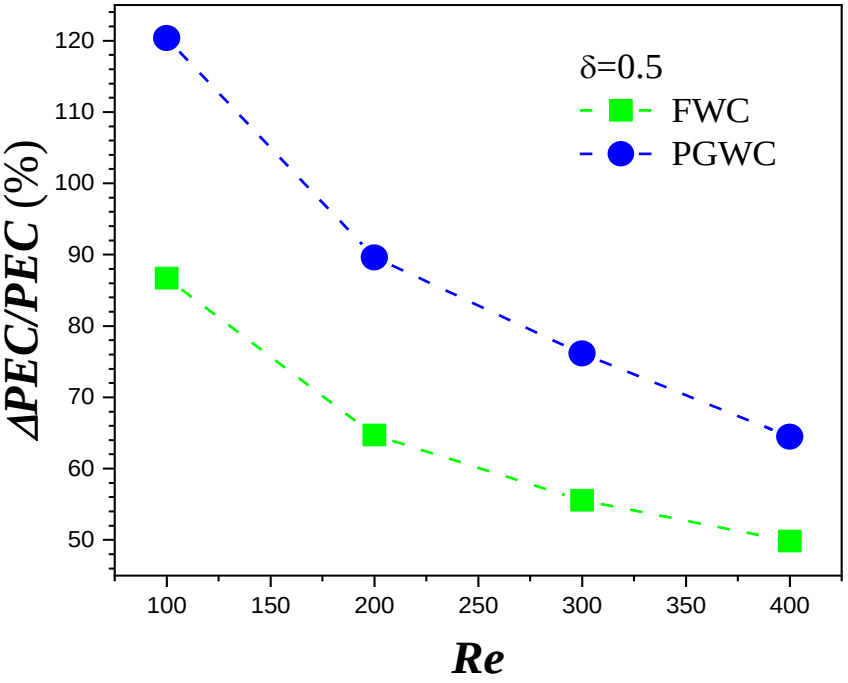


Figure 4.18B. Effect of the Reynolds number on the relative gap of the performance evaluation criteria.

These results are consistent with the findings of Moghadasi et al. [24] for a straight U-bend pipe with a porous layer at the pipe center, where PEC decreased over the δ range of 0.2–0.8, with corresponding PEC values in a similar range.

Table 4.6B. Effect of δ and Re on the PEC, using the clear wavy channel as reference

	δ, Re=400					Re, δ=0.5			
	0.0	0.2	0.3	0.4	0.5	100	200	300	400
PEC_{clear}	0.73	0.73	0.73	0.73	0.73	1.02	0.97	0.94	0.92
PEC_{foam}	0.73	0.58	0.55	0.53	0.49	0.55	0.59	0.61	0.62
$PEC_{granular}$	0.73	0.57	0.53	0.50	0.45	0.46	0.51	0.54	0.56
$(\Delta PEC/PEC)_{foam}$ (%)	0.0	26.62	33.67	38.93	49.96	86.67	64.68	55.56	49.85
$(\Delta PEC/PEC)_{gran}$ (%)	0.0	28.55	39.48	46.21	64.61	120.35	89.60	76.15	64.48

Figures 4.17B, 4.18B, and Table 4.6B present a comparison of the relative PEC gap between the porous foam and packed granular channels, using the clear wavy channel as a reference. Compared with the clear channel, increasing the porous layer thickness (δ) reduces the PEC gap. At $Re = 400$ and $\delta = 0.5$, the reduction is 64.61% for the packed granular channel and 49.96% for the foam channel. Increasing Re also decreases the relative PEC gap: as Re rises from 100 to 400, the reduction changes from 120.35% to 64.48% for the packed granular channel and from 86.67% to 49.85% for the foam channel.

4.8B Conclusion

A numerical investigation was carried out on the heat transfer, fluid dynamics, and entropy generation of a silver/water nanofluid flowing through a wavy channel partially filled with copper porous material. The studied wavy heat exchanger consists of three sections: the inlet and outlet sections are smooth and adiabatic, while the intermediate sinusoidal segment is maintained at a constant temperature. The numerical results are consistent with previous studies, validating the approach.

This study focused on the following key aspects:

1. Heat transfer analysis of laminar nanofluid flow in a wavy channel heat exchanger, considering cases of a clear channel and channels partially filled with packed granular or foam materials.

2. Evaluation of the effects of the dimensionless amplitude (δ) and Reynolds number (Re) on the Nusselt number, entropy generation, performance evaluation criterion (PEC), and hydrodynamic–thermal parameters.

3. Comparison of thermal performance between wavy porous channels partially filled with packed granular material versus foam.

From the simulation results conducted over the Reynolds number range $Re = 100–400$ and dimensionless amplitude $\delta = 0.2–0.5$, considering a silver–water nanofluid with a volume fraction $\varphi = 5\%$ and a copper porous material (foam: $\varepsilon = 0.8$, $PPI = 10$; packed granular: $\varepsilon = 0.373$) under isothermal heating conditions, the main conclusions of this study can be summarized as follows:

- Porous insertion significantly enhances heat transfer, entropy generation, and the friction factor.

- The structure of the porous material strongly influences the thermal performance of the wavy channel, with packed granular material having a more pronounced effect than foam.

- For $Re = 400$ and $\delta = 0.2–0.5$, compared to a clear channel, the mean Nusselt number ($\overline{Nu}$) increases by 43.04%–134.64% and the mean entropy generation ($\bar{S}$) by 97.68%–437.06% for the packed granular material. The corresponding increases are less pronounced for foam, with $\overline{Nu}$ rising by 36.19%–94.53% and $\bar{S}$ by 70.83%–197.90%.

- The relative variation of the friction factor is nearly independent of Re, showing only a slight increase with δ.

- Substantial improvements in heat transfer and entropy generation can be achieved through the interplay between the Reynolds number and the porous layer thickness.

CHAPTER 4 (C):

HEAT TRANSFER IN A WAVY CHANNEL CONVERGENT DIVERGENT CHANNEL

4.1C Introduction

This chapter investigates the effect of the shrinkage thickness parameter on the primary characteristics of nanofluid flow within a convergent-divergent heat exchanger plate channel. The analyzed parameters include velocity vector contours and magnitudes, streamlines, isotherm contours, local and mean Nusselt numbers, entropy, and the relative variations of both Nusselt number and entropy. Five geometrical configurations of the convergent-divergent channel are considered, corresponding to different shrinkage thickness parameter values: $\delta_s = 0.0$, 0.2, 0.4, 0.6, and 0.8.

Numerical simulations are conducted using water as the base fluid and CuO nanoparticles, accounting for the effects of both the shrinkage thickness parameter and the flow Reynolds number. The simulations are performed for a nanofluid volume fraction of φ = 5%, Reynolds numbers in the range of 100–500, and shrinkage thickness parameter values from 0 to 0.8. The simulation data are presented in Table 6.1, and the corresponding results are discussed in Sections 6.4 through 6.8.

4.2C Physical model of convergent-divergent channel heat exchanger

The studied plate-type convergent-divergent channel heat exchanger is divided into three sections, as illustrated in Figure 4.1C. The inlet and outlet sections are smooth and adiabatic, while the intermediate sinusoidal section is maintained at a constant temperature (isothermal). The entrance section has a length of $1.5H_c$, whereas the convergent-divergent section extends over $12H_c$ [157].

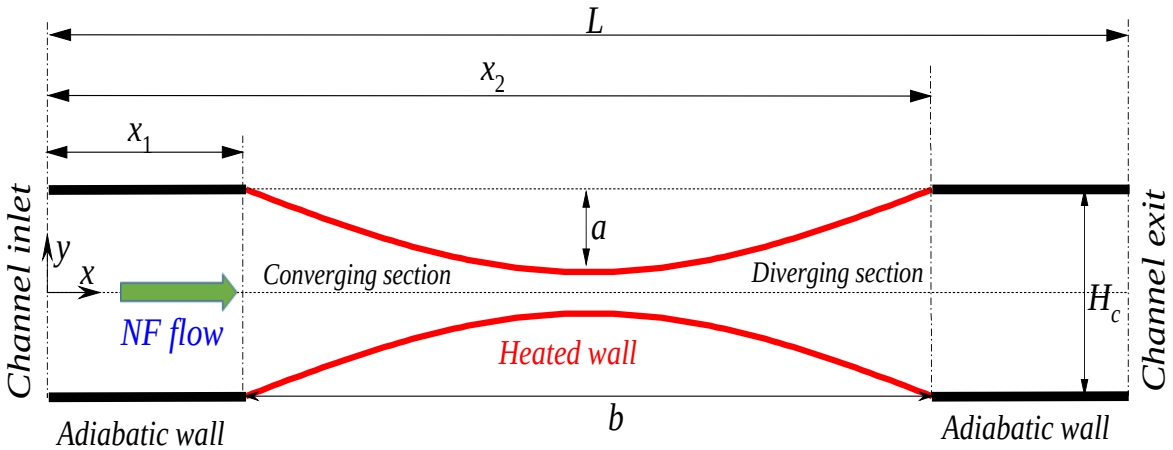


Figure 4.1C Schematic of the studied convergent–divergent plate channel heat exchanger (Physical Configuration 4)

The heated surface exhibits a sinusoidal convergent-divergent profile, with an amplitude a and a wavelength equal to twice the length b of the heated section. The y-coordinates of the upper and lower walls of the convergent-divergent section are defined by the following equations, respectively:

$$y_t(x) = \frac{H_c}{2} - a \cdot \sin\left(\frac{\pi(x - x_1)}{b}\right) \tag{6.1}$$

$$y_b(x) = -\frac{H_c}{2} + a \cdot \sin\left(\frac{\pi(x - x_1)}{b}\right) \tag{6.2}$$

The convergent-divergent channel is characterized by the shrinkage thickness parameter, defined as:

$$\delta_s = \frac{H_c - H_t}{H_c} = 1 - \frac{H_t}{H_c} \tag{6.3}$$

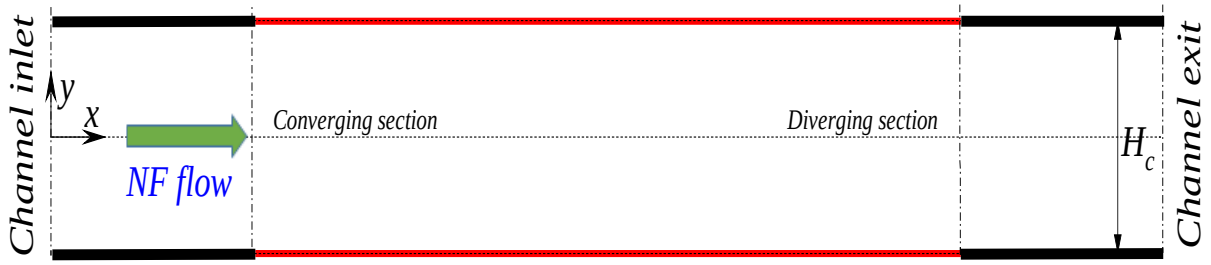
Here, H_t denotes the height of the throat, H_c is the height of the channel, and x and y represent the Cartesian coordinates.

4.3C Simulated geometric cases for the convergent-divergent channel

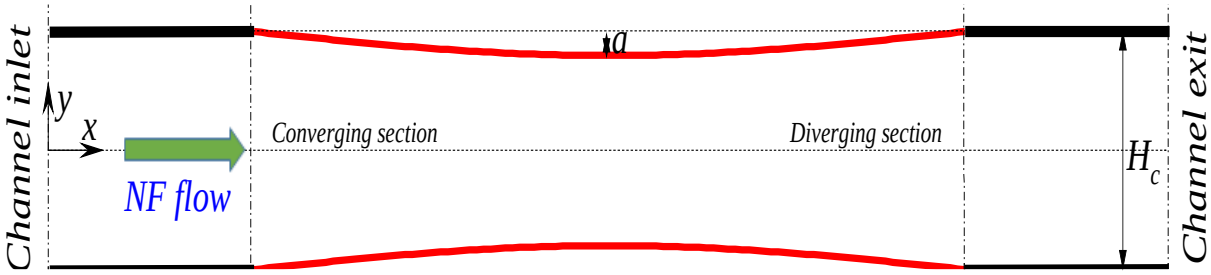
The simulated geometric cases correspond to different values of the flow-section reduction, represented by the shrinkage thickness parameter: $\delta_s = 0.2$, 0.4, 0.6, 0.8, and 1.0. The limit value $\delta_s = 1$ corresponds to a convergent-divergent channel without a passage section, whereas $\delta_s = 0$ represents a straight channel. These configurations are illustrated in Figure 4.2C.

Table 4.1C: Simulation data for the studied plate convergent–divergent channel heat exchanger

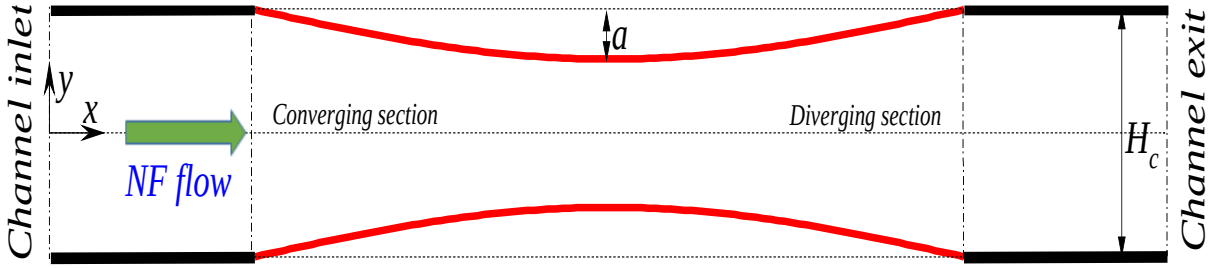
Channel height	0.01 m
Length of adiabatic section	0.015 m
Length of heated section	0.12 m
Base fluid	Water
Nanoparticles	CuO
Nanoparticles fraction	5%
Shrinkage thickness parameter	0.0; 0.2; 0.4; 0.6; 0.8
Reynolds number	100; 200; 300; 400; 500



δ_s=0

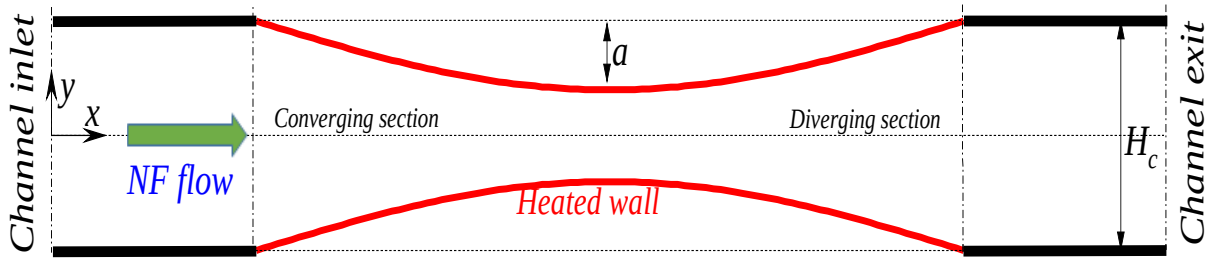


δ_s=0.2

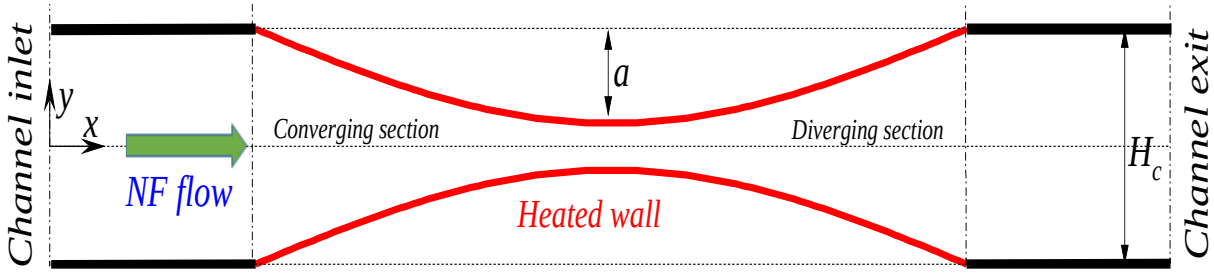


δ_s=0.4

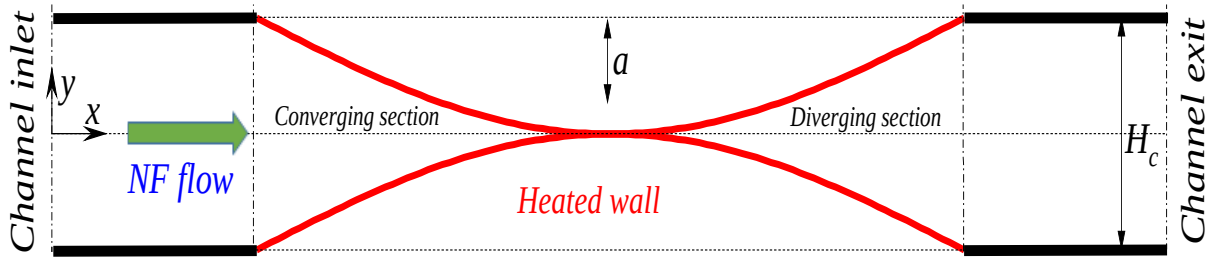
Figure 4.2C (a) Convergent–divergent heated section for different values of the shrinkage thickness parameter (δ_s = 0, 0.2, and 0.4)



δ_s=0.6



δ_s=0.8

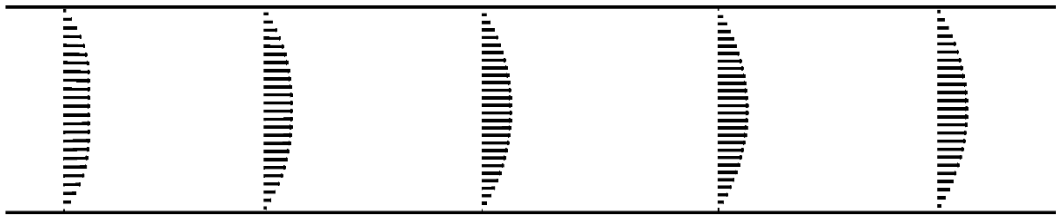


δ_s=1.0

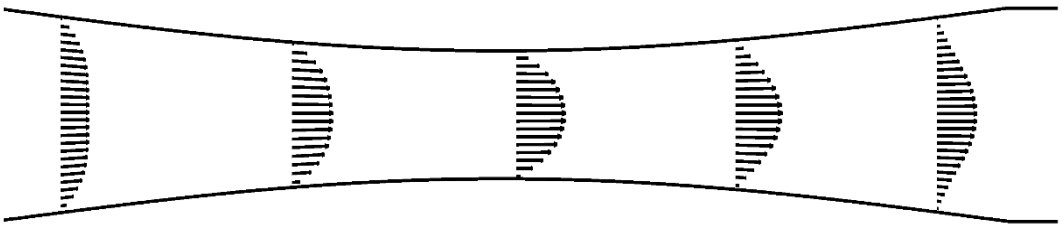
Figure 4.2C (b) Convergent–divergent heated section for different values of the shrinkage thickness parameter ($\delta_s = 0.6$, 0.8, and 1.0)

4.4C Effect of the shrinkage thickness parameter on velocity vectors and streamlines

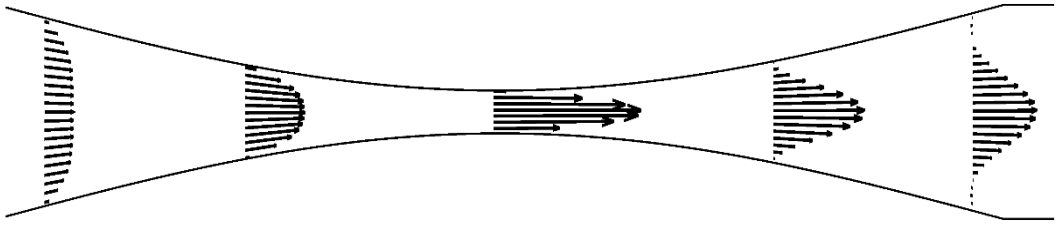
Figure 4.3C shows the velocity vectors for different values of δ at $Re = 400$ and $\varphi = 5\%$, illustrating the evolution of the velocity along the channel. The velocity reaches its maximum at the throat, while it decreases significantly in the divergent section. In the convergent regions of the channel, the velocity vectors exhibit higher intensity compared to other areas. Flow reversal is observed near the walls within the diverging section. These reversed flows create recirculation zones that disturb the overall flow, significantly affecting the temperature distribution.



δ_s=0.0



δ_s=0.4



δ_s=0.8

Figure 4.3C Effect of the shrinkage thickness parameter on velocity vectors at $Re = 400$

Figure 4.4C presents the streamlines for different values of δ_s at $Re = 400$ and $\varphi = 5\%$. As shown, flow reversal occurs near the diverging wall at $\delta_s = 0.8$. With increasing δ_s, the size of the recirculation zones also increases, causing greater disturbances in the flow pattern. In this section, the impact of these vortices on heat transfer, flow behavior, and entropy generation within the wavy channel will be analyzed.

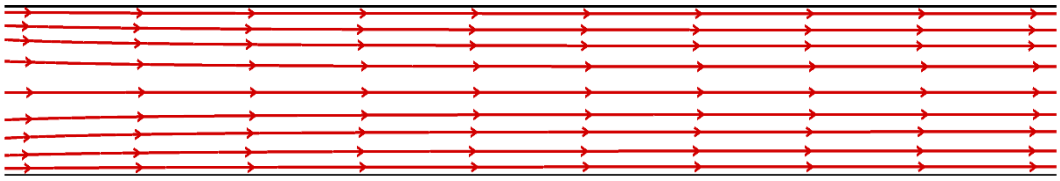
4.5C Effect of the Shrinkage Thickness Parameter on Velocity Magnitude and Isotherms

Figure 4.5C illustrates the velocity magnitude distribution for different values of δ_s at $Re = 400$ and $\varphi = 5\%$. As shown, two regions of low-velocity fluid are typically observed near the upper and lower walls. When $\delta_s = 0$, these low-velocity regions are completely uniform. As expected, the velocity increases in the convergent sections of the wavy wall. Increasing δ_s further enhances the velocity magnitude near the throat. Conversely, low velocities occur at the exit of the divergent sections due to fluid recirculation.

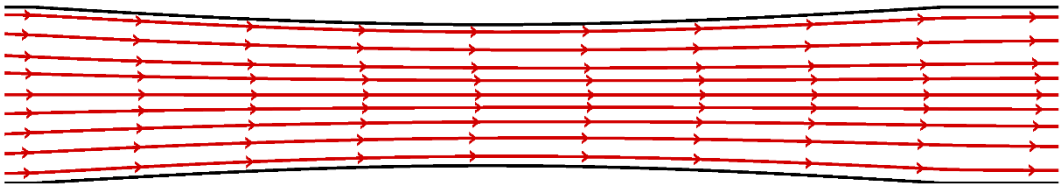
Figure 4.6C shows the isotherms for different values of δ_s at $Re = 400$ and $\varphi = 5\%$. The figure indicates that in the convergent region, the thermal boundary layer thickness decreases as the shrinkage thickness increases. Higher δ_s values lead to faster flow in the channel center, causing the isotherms to become more compact near the walls and thereby increasing the temperature gradients. In the diverging section, the fluid temperature near the walls is higher than in the convergent regions, due to the influence of vortices that induce flow reversal in these areas.

4.6C Effect of the shrinkage thickness parameter on local Nusselt number and entropy

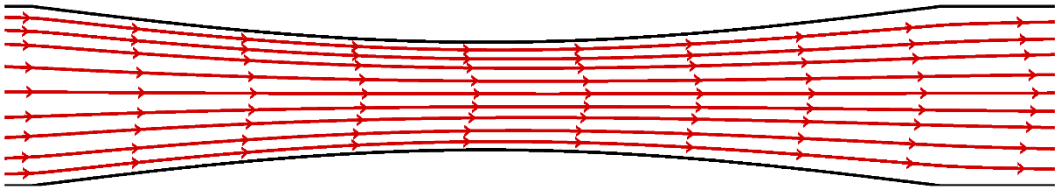
Figures 4.7C and 4.8C illustrate the effect of δs on the local Nusselt number (Nu) and entropy generation (S) along the length of the heated channel for two Reynolds numbers, $Re = 200$ and $Re = 500$. As shown, both Nu and S reach their maximum values at the throat of the channel, depending on the shrinkage thickness parameter, and attain their minimum values in the diverging sections. Additionally, Nu and S in the convergent regions increase with δ_s, indicating an enhanced heat transfer rate in these areas. This corresponds to a reduction in the thermal boundary layer thickness, which further promotes heat transfer. For a straight channel, it is observed that Nu and S are highest at the inlet and decrease gradually along the channel length.



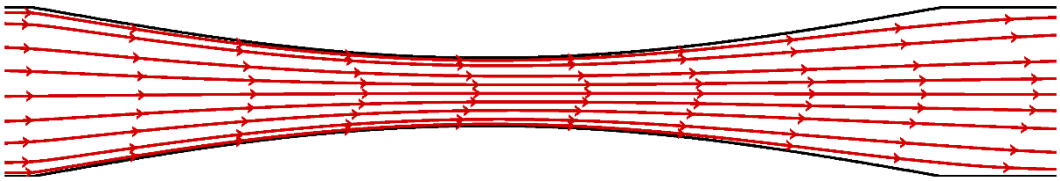
δ=0.0



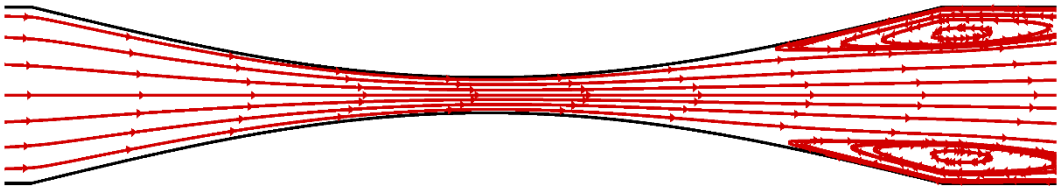
δ=0.2



δ=0.4



δ=0.6



δ=0.8

Figure 4.4C Effect of the shrinkage thickness parameter on streamlines at $Re = 400$

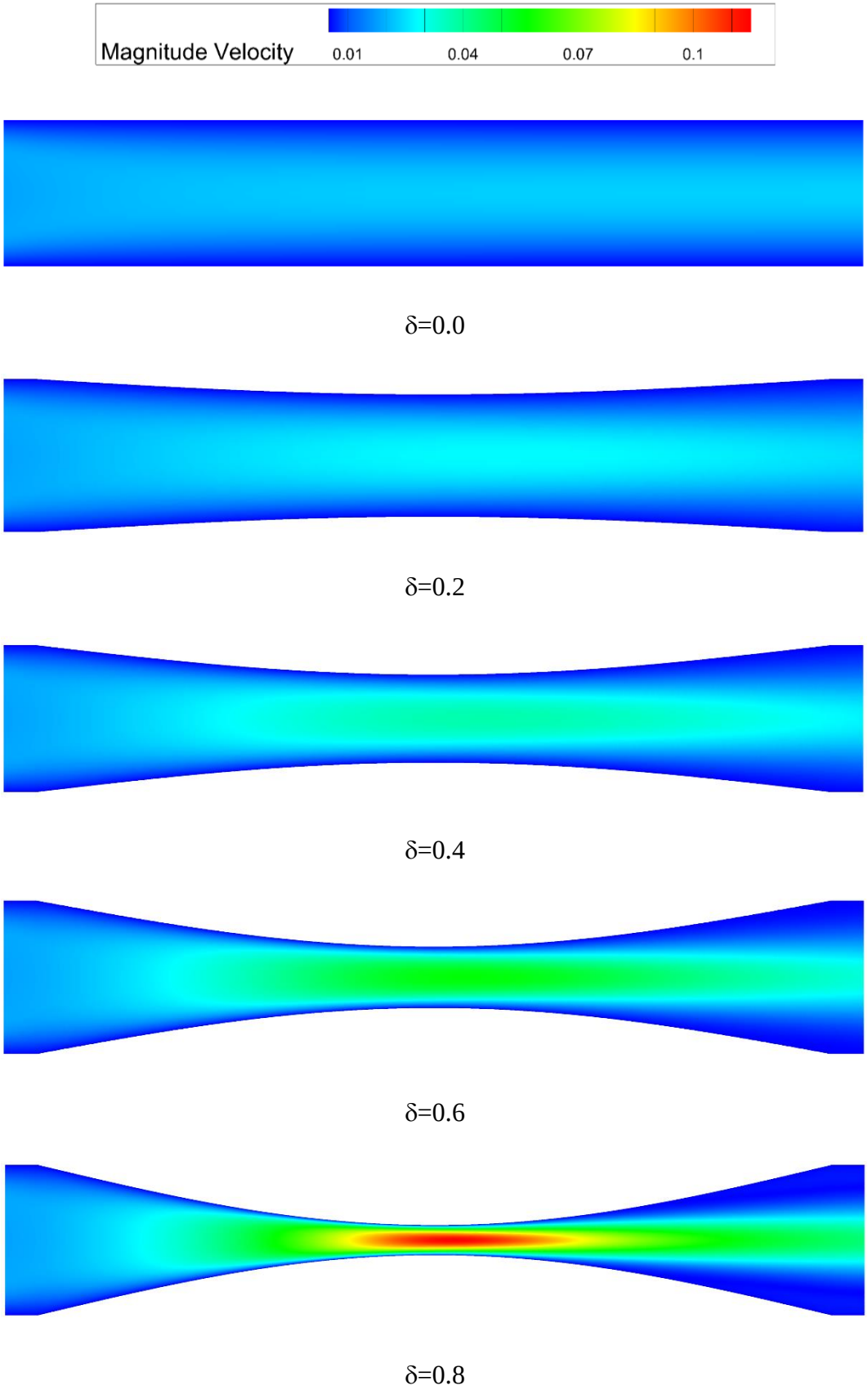


Figure 4.5C Effect of the shrinkage thickness parameter on velocity magnitude at Re = 400

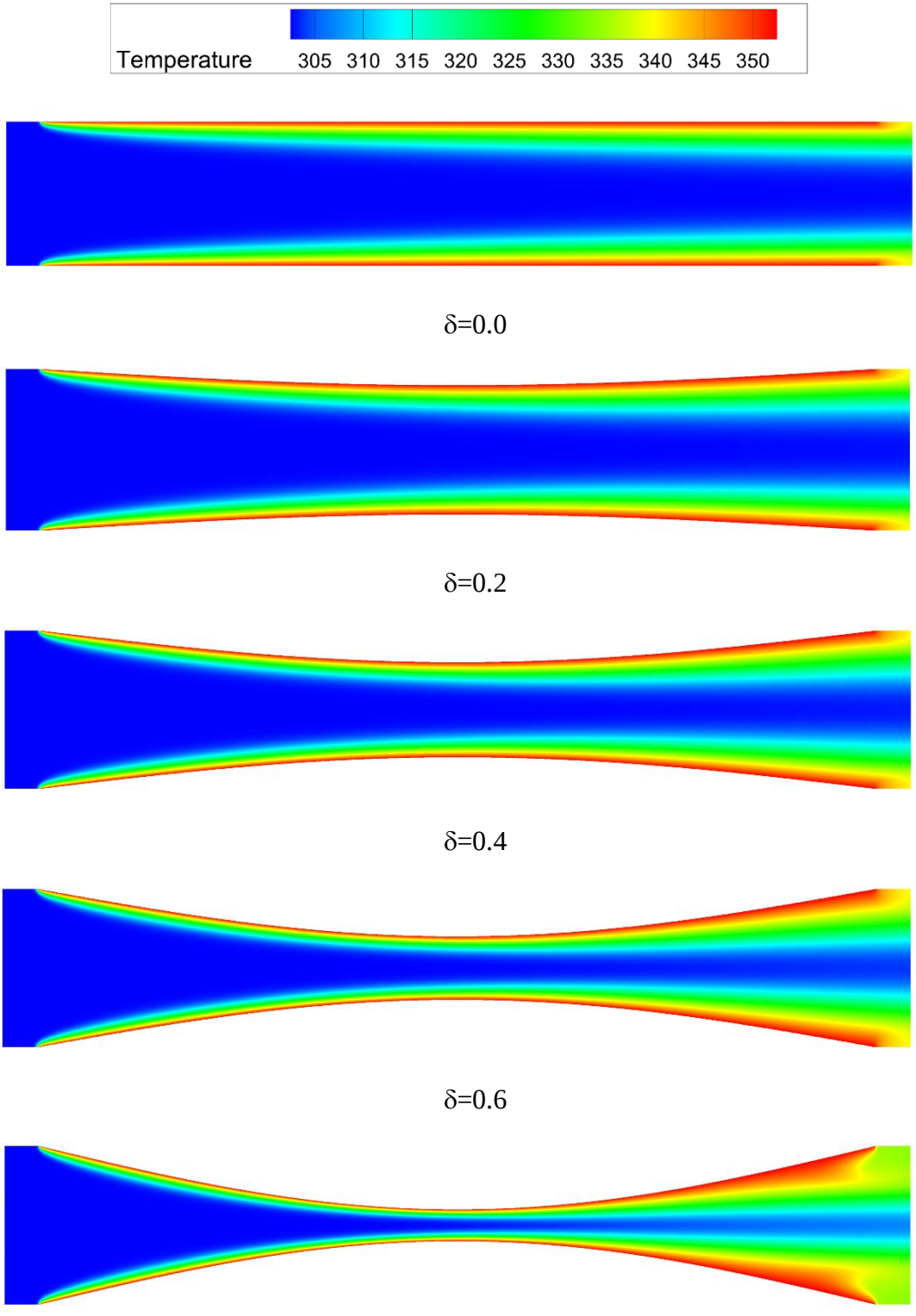
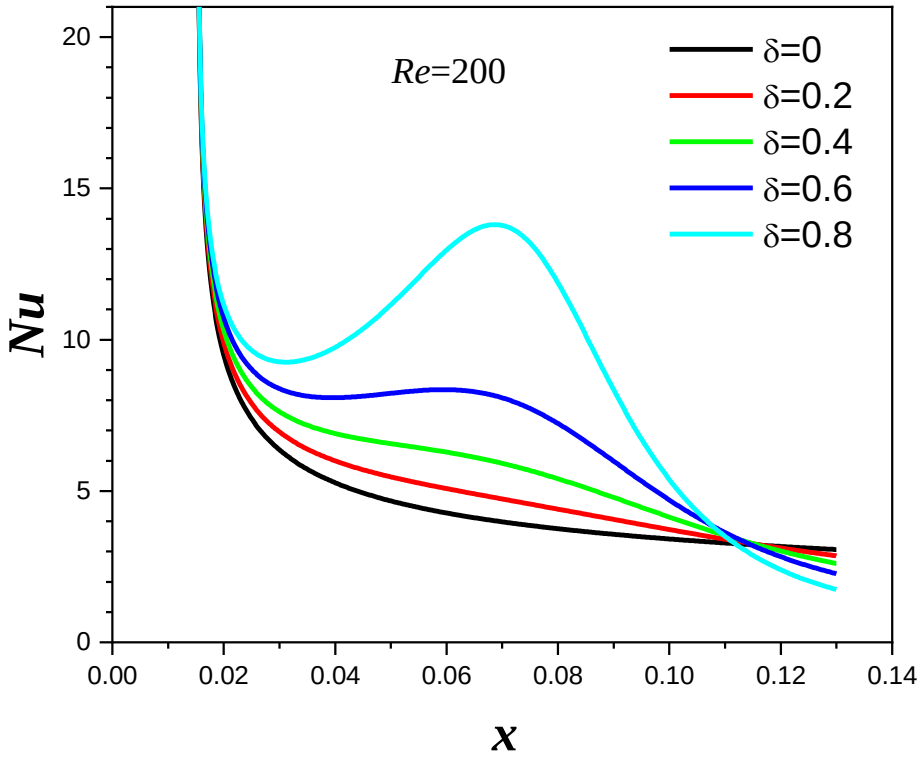


Figure 4.6C Effect of the shrinkage thickness parameter on isotherms at Re = 400



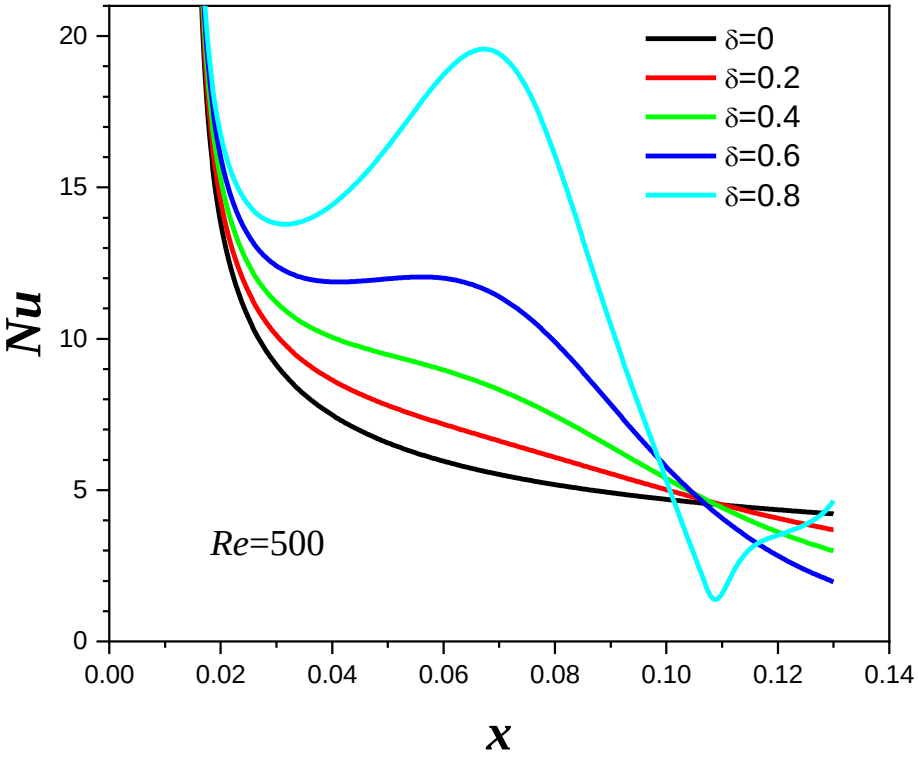
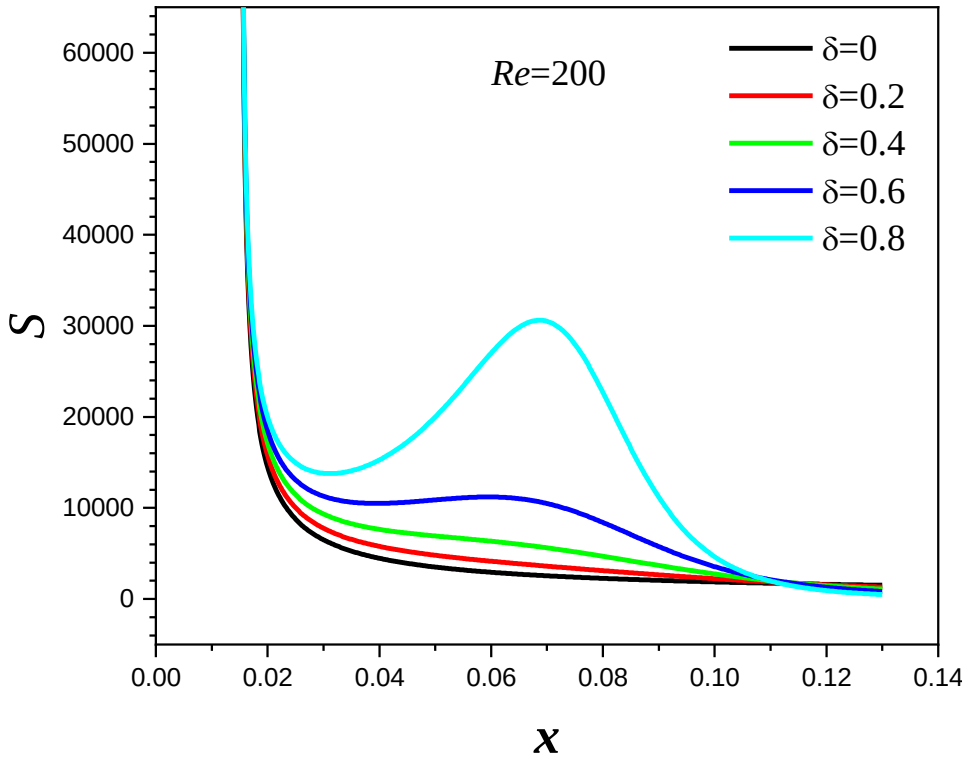


Figure 4.7C Effect of the shrinkage thickness parameter on the local Nusselt number for different Reynolds numbers: (a) $Re = 200$, (b) $Re = 500$



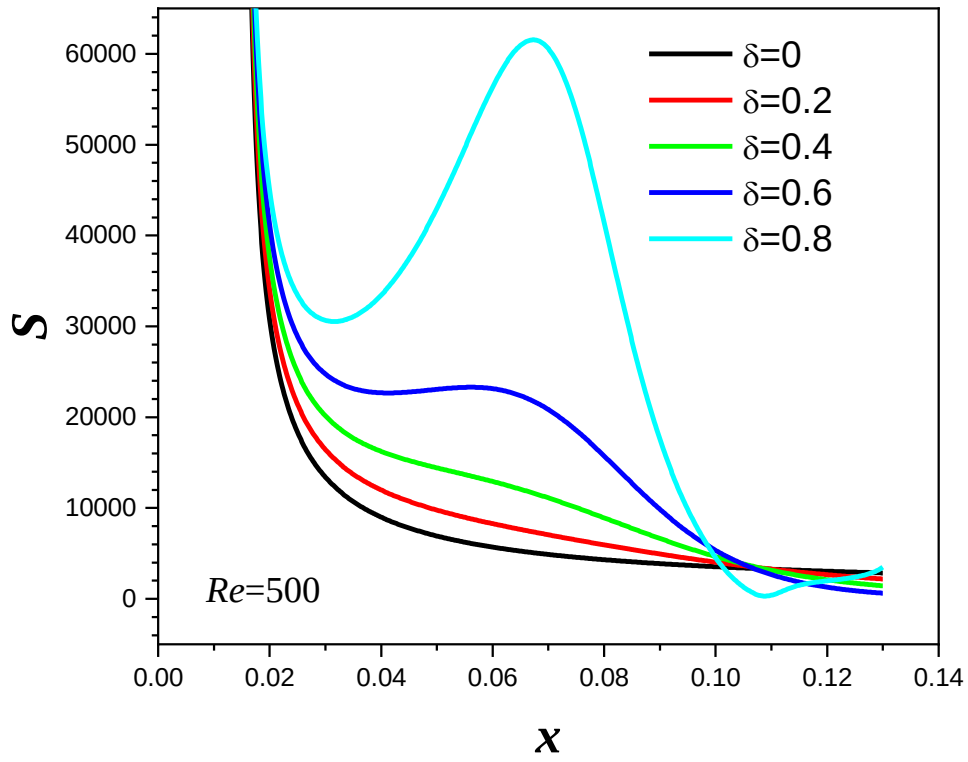


Figure 4.8C Effect of the shrinkage thickness parameter on local entropy for different Reynolds numbers: (a) $Re = 200$, (b) $Re = 500$

4.7C Effect of the shrinkage thickness parameter on average Nusselt number and entropy

Figures 4.9C, 4.10C, and Tables 4.2C and 4.3C present the effect of the shrinkage thickness parameter δ_s on the average Nusselt number ($\overline{Nu}$) and average entropy ($\bar{S}$) over the Reynolds number range 100–500. For all Reynolds numbers, both $\overline{Nu}$ and $\bar{S}$ increase with δ_s. As shown, for $\delta_s = 0.8$ and $Re = 500$, the average Nusselt number increases by approximately 82%, while the average entropy rises by 210% in the convergent-divergent channel compared to the straight duct.

For $Re = 400$, increasing the shrinkage thickness parameter from 0.2 to 0.8 leads to an enhancement of the average Nusselt number ($\overline{Nu}$) by 9.3%–82.2% and average entropy ($\bar{S}$) by 15.4%–212.1%. This observation underscores the critical role of the shrinkage thickness, which governs the velocity magnitude and vortex formation, thereby significantly enhancing heat transfer.

Table 4.2C: Effect of shrinkage thickness parameter on $\Delta\overline{Nu}/\overline{Nu}$ (%) for different Reynolds numbers, using straight channel as Reference

$\Delta\overline{Nu}/\overline{Nu}$ (%)					
δ	*Re*=100	*Re*=200	*Re*=300	*Re*=400	*Re*=500
0.2	9.20855671	9.4276954	9.39436137	9.33753652	9.27720673
0.4	21.8353625	22.4468431	22.1698122	21.8436131	21.5397027
0.6	40.7505316	42.6061275	41.7300082	40.6847922	39.786551
0.8	74.6744166	82.9917209	81.1204617	82.1994559	82.6999136

Table 4.3C: Effect of shrinkage thickness parameter on $\Delta\bar{S}/\bar{S}$ (%) for different Reynolds numbers, using straight channel as reference

$\Delta\bar{S}/\bar{S}$ (%)					
δ	*Re*=100	*Re*=200	*Re*=300	*Re*=400	*Re*=500
0.2	14.2869674	14.9261077	15.1938722	15.3761959	15.5215812
0.4	37.4436322	39.2813598	39.7473325	40.0653042	40.3498464
0.6	79.4421555	84.0025659	84.3163949	84.3800586	84.5568194
0.8	189.2627	210.594687	210.930495	212.143936	212.559728

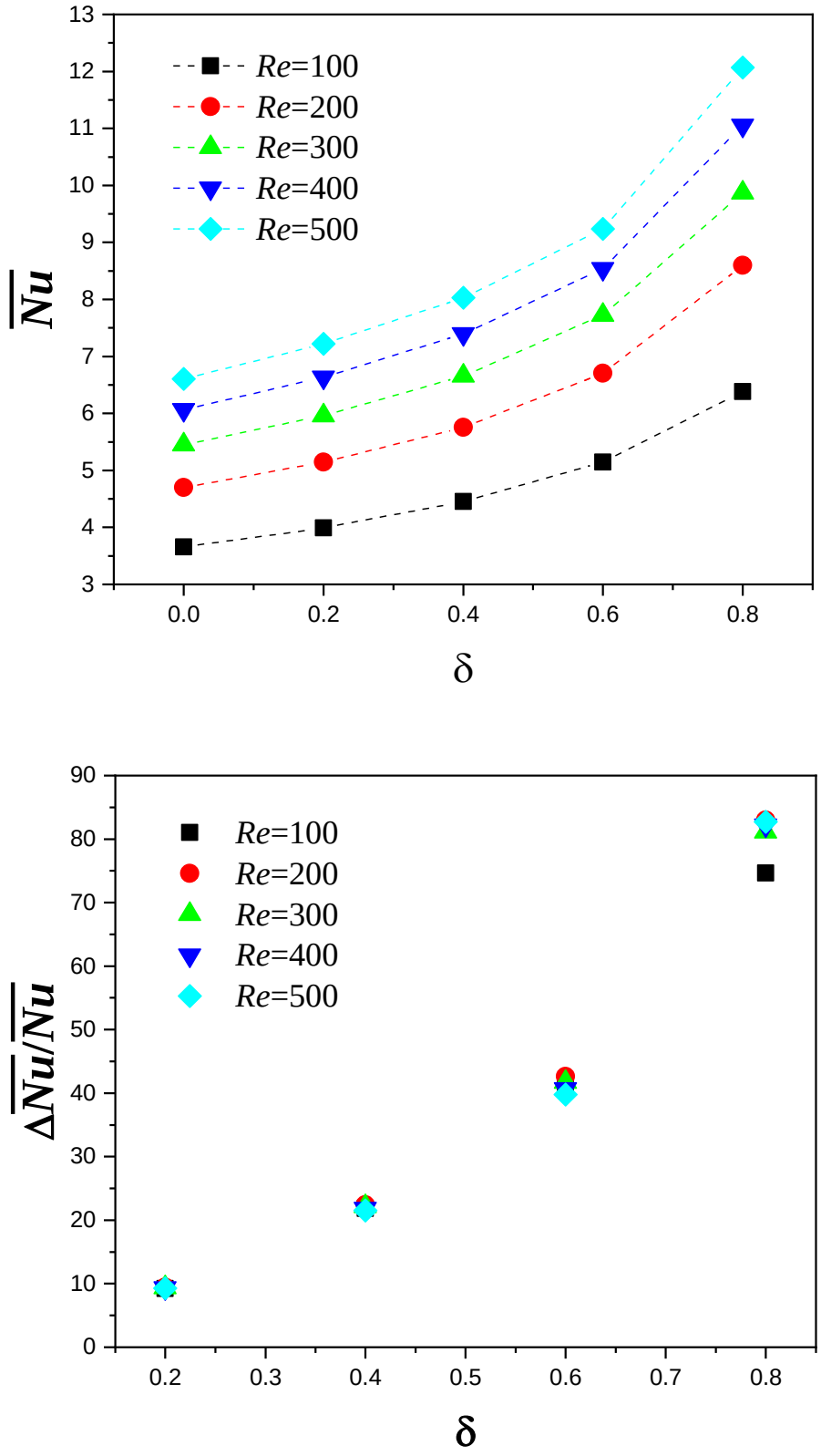
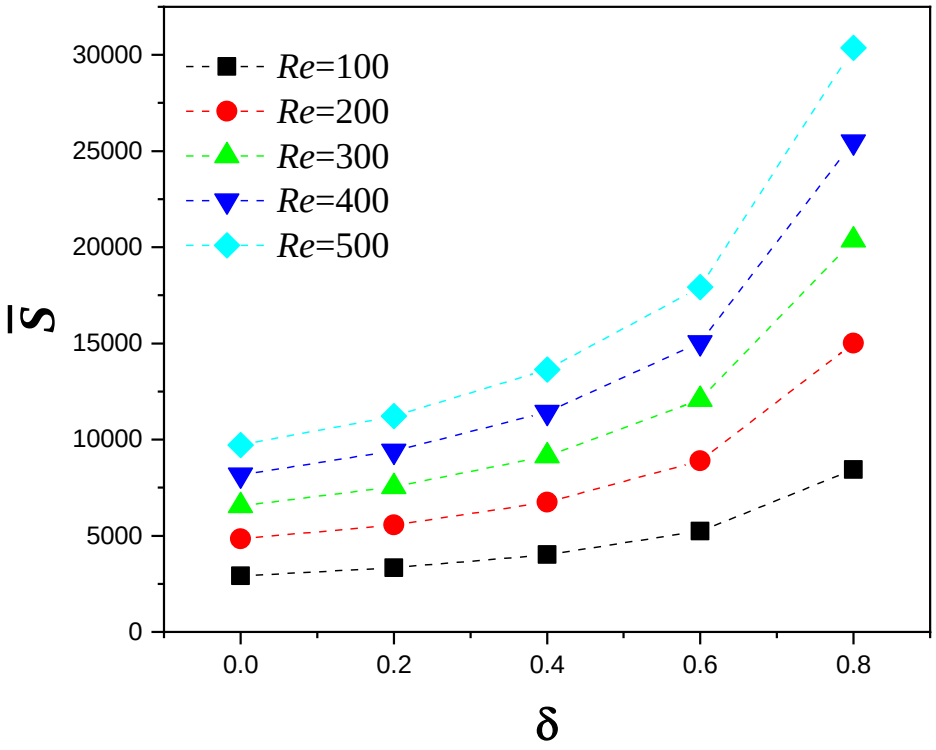


Figure 4.9C Effect of the shrinkage thickness parameter on the average Nusselt number for different Reynolds numbers



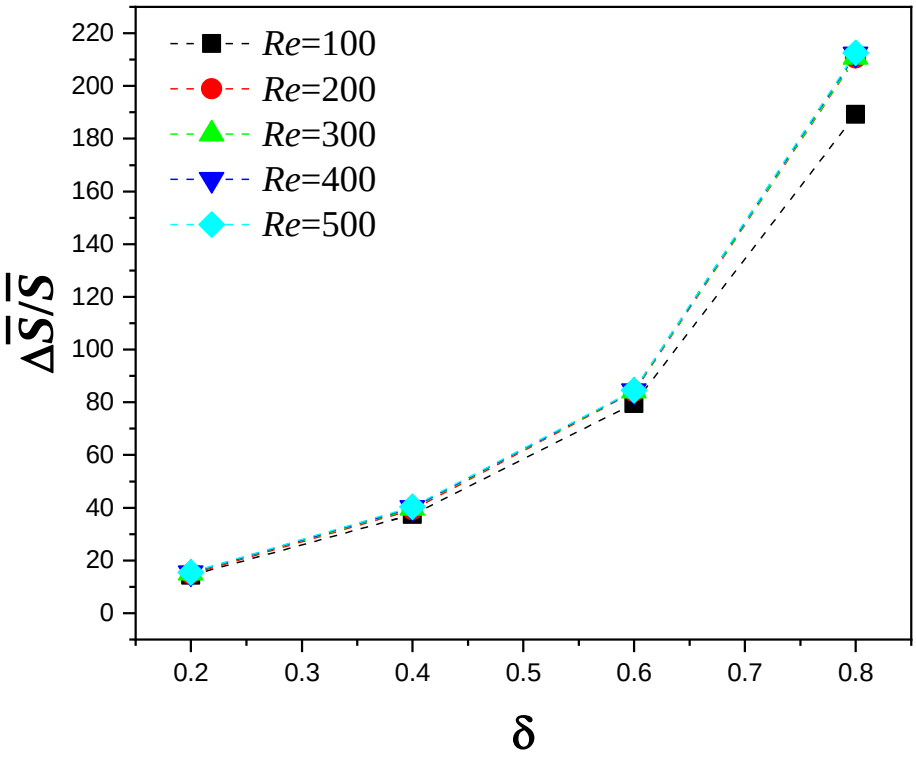


Figure 4.10C Effect of the shrinkage thickness parameter on the average entropy for different Reynolds numbers

4.8C Effect of the Reynolds number on average Nusselt number and entropy

Figures 4.11C–4.14C and Tables 4.4C–4.5C illustrate the variation of the average Nusselt number ($\overline{Nu}$) and average entropy ($\bar{S}$) with the Reynolds number for the convergent–divergent channel, considering shrinkage thickness parameter values in the range 0.2–1.0 and a nanoparticle volume fraction of $\varphi = 5\%$. As shown, both $\overline{Nu}$ and $\bar{S}$ increase with increasing Reynolds number. This increase is quasi-linear and becomes more pronounced at higher shrinkage thickness parameter values compared to the straight duct.

Compared with the straight duct, at $Re = 300$ and $\delta_s = 0.6$, the convergent–divergent channel exhibits increases of approximately 42% in $\overline{Nu}$ and 84% in $\bar{S}$. The enhancement becomes even more significant at higher shrinkage thickness parameters. For instance, at $Re = 300$ and $\delta_s = 0.8$, $\overline{Nu}$ increases by about 81%, while the entropy generation rises by approximately 211%.

Table 4.4C Effect of Reynolds number on $\Delta\overline{Nu}/\overline{Nu}$ (%) for different geometrical configurations, with the straight channel as the reference.

	$\Delta\overline{Nu}/\overline{Nu}$ (%)			
Re	**δ=0.2**	**δ=0.4**	**δ=0.6**	**δ=0.8**
100	9.20856	21.83536	40.75053	74.67442
200	9.4277	22.44684	42.60613	82.99172
300	9.39436	22.16981	41.73001	81.12046
400	9.33754	21.84361	40.68479	82.19946
500	9.27721	21.5397	39.78655	82.69991

Table 4.5C Effect of Reynolds number on $\Delta\bar{S}/\bar{S}$ (%) for different geometrical cases, with the straight channel as the reference.

	$\Delta\bar{S}/\bar{S}$ (%)			
Re	**δ=0.2**	**δ=0.4**	**δ=0.6**	**δ=0.8**
100	14.2869674	37.4436322	79.4421555	189.2627
200	14.9255521	39.2798976	83.9994392	210.586848
300	15.1938722	39.7473325	84.3163949	210.930495
400	15.3762	40.0653	84.38006	212.14394
500	15.5215812	40.3498464	84.5568194	212.559728

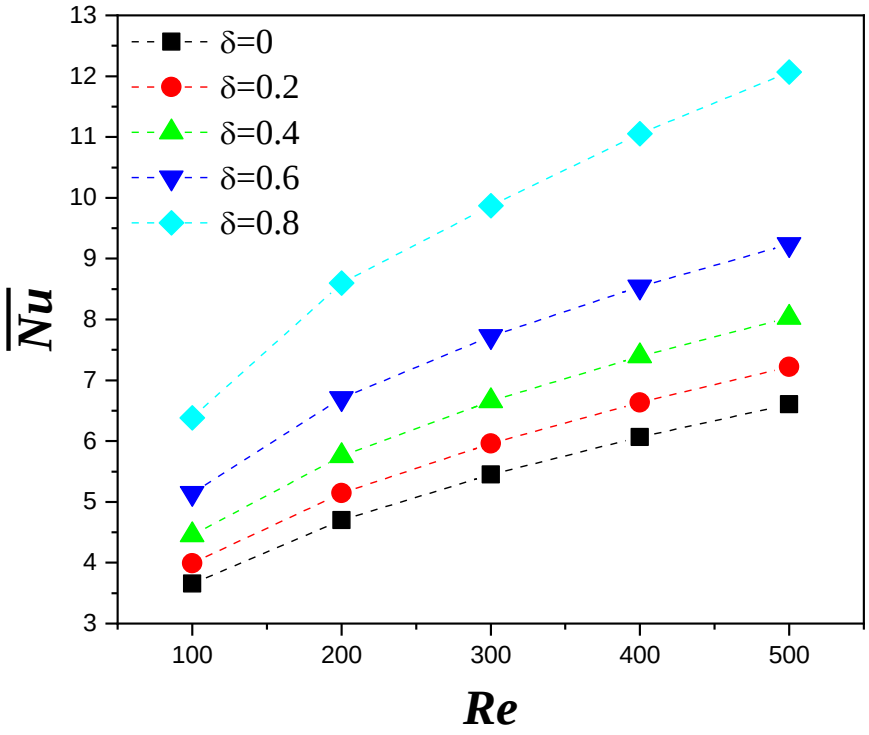


Figure 4.11C Effect of Reynolds number on the average Nusselt number for straight and convergent–divergent channels across different geometrical cases

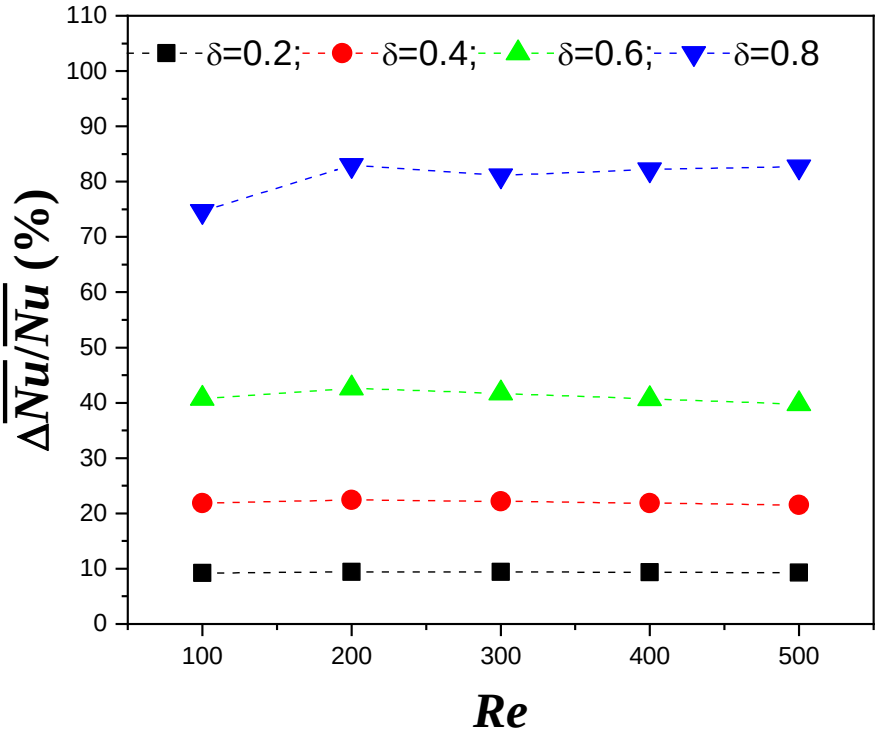


Figure 4.12C Effect of Reynolds number on the rate of change of the average Nusselt number for different geometrical cases

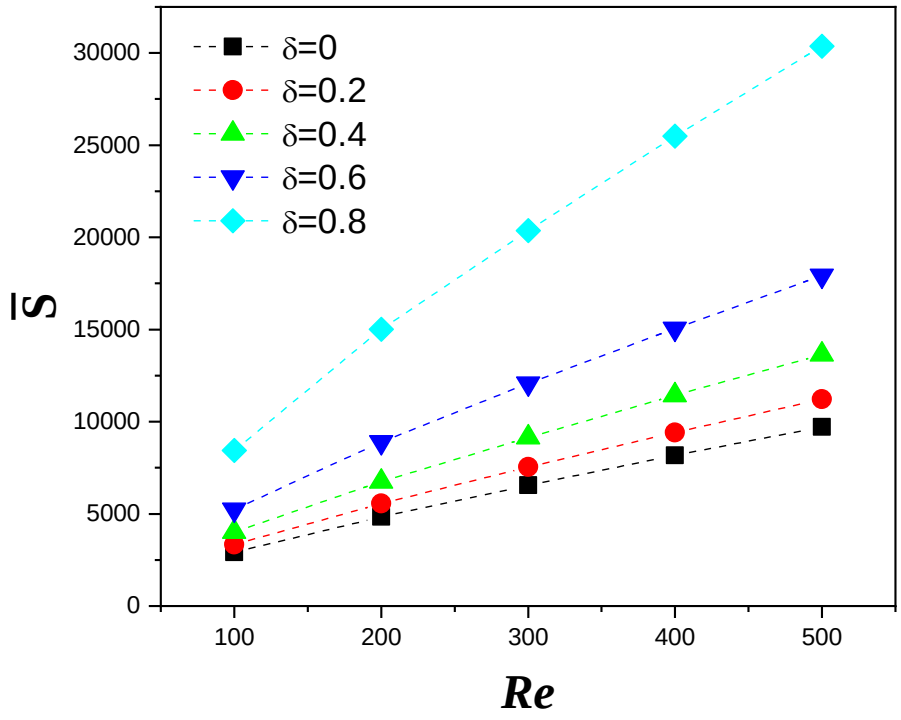


Figure 4.13C Effect of Reynolds number on the average entropy for straight and convergent–divergent channels across different geometrical cases

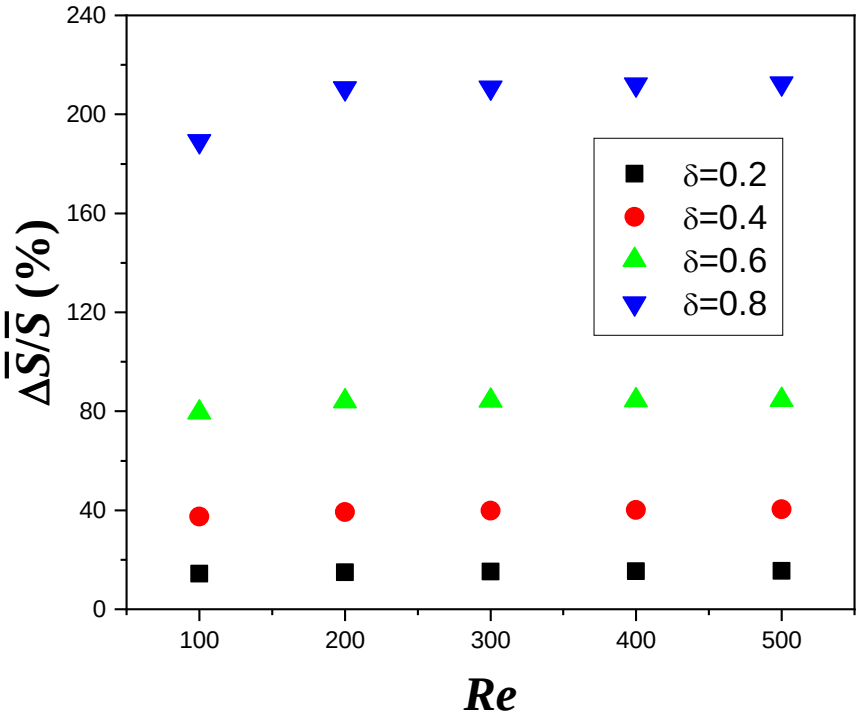


Figure 4.14C Effect of Reynolds number on the rate of change of average entropy for different geometrical cases

It is important to mention that the interaction between enhanced heat transfer and related thermodynamic irreversibility's can be used to explain the simultaneous increase of the Nusselt number (Nu) and total entropy generation (S_g) in a wavy channel, whether it is fully, partially, or not filled with porous material.

The increase of the Nusselt number is assigned principally to [3], [11], [90]:

- The geometry of a wavy channel that creates complex flow patterns like recirculation zones, flow separation, and vortices.
- In the presence of a porous medium (full or partially filled) where the solid matrix can also enhance effective thermal conductivity and induce additional flow resistance that modifies velocity and temperature profiles, frequently further increasing heat transfer. These effects also increase convective heat transfer by increasing fluid mixing and decreasing thermal boundary layer thickness, which results in an increase in the Nusselt number.

For an increase in entropy generation, there are two primary causes of entropy generation in these systems:

- Thermal irreversibility, or heat transfer, brought on by finite temperature differentials.
- Irreversible fluid friction (pressure drop) brought on by flow resistance and viscous effects.

The corresponding temperature gradients usually more pronounced as the Nusselt number rises (indicating higher heat transfer rates), which raises entropy generation because of thermal irreversibility. Furthermore, porous media and wavy channels increase flow resistance, which raises pressure drops and, consequently, entropy generation from fluid friction. Heat transfer and irreversibility are improved when porous media are used, particularly in partially filled configurations, where the flow may be restricted or redirected.

Also, it is important to point out that the relationship between the Nusselt number and the total entropy has been the subject of various scientific works. These references provide a

comprehensive understanding of how the Nusselt number and total entropy generation can increase simultaneously in corrugated channels, with or without porous media. Specifically:

Mahmud and Fraser [158] analyzed the laminar forced convection in a channel saturated with a porous medium using the second law. According to this research, better heat transfer performance is indicated by a rising Nusselt number in paire with an increasing Darcy number. However, because of the combined effects of viscous dissipation and irreversible heat transfer, this improvement comes at the expense of increased total entropy generation.

Bejan [159] was the first who presented the Entropy generation minimization (EGM) as a basic design technique in thermal system optimization. He highlighted the intrinsic trade-off between minimizing entropy generation and optimizing heat transfer, which is usually indicated by a higher Nusselt number. Bejan's analysis emphasizes how difficult it is to accomplish both goals at once because improving one frequently has a negative impact on the other.

The second-law properties of forced convection in porous media channels were also investigated by Al-Amiri [160]. His research showed that higher Nusselt numbers, which indicate better heat transfer, are caused by increases in both the Reynolds and Darcy numbers. However, this also leads to increased entropy generation, mainly due to steeper temperature gradients and increased viscous dissipation.

The impact of wave geometry on heat transfer and entropy generation in two-dimensional wavy ducts was examined by Nourani Zonouz [161]. According to his research, heat transfer is improved when wave amplitude increases because it raises the Nusselt number. The performance-irreversibility trade-off in thermofluid systems with complex geometries is highlighted by the fact that this geometric modification also results in increased total entropy generation because of increased frictional losses and thermal gradients.

To recapitulate, improved heat transfer is reflected in the increase in Nusselt number, but increased thermodynamic irreversibility from both heat transfer and viscous dissipation is indicated by the simultaneous rise in total entropy generation.

4.9C Conclusion

The numerical study examined the effects of the shrinkage thickness parameter and the Reynolds number on the main parameters characterizing heat transfer and entropy generation in a plate channel incorporating a sinusoidal heated convergent–divergent section. Based on the numerical results obtained using a CuO/water nanofluid, the primary conclusions of this investigation can be summarized as follows:

- The shrinkage thickness parameter has a significant impact on both heat transfer and entropy generation. The average Nusselt number ($\overline{Nu}$) and average entropy ($\bar{S}$) increase almost linearly with δ_s. At $Re = 500$, compared with the straight channel ($\delta_s = 0$), increasing the shrinkage thickness parameter to $\delta_s = 0.8$ results in enhancements of approximately 82.7% in $\overline{Nu}$ and 212.6% in $\bar{S}$.

- The average Nusselt number ($\overline{Nu}$) and average entropy ($\bar{S}$) increase with the Reynolds number. This increase is quasi-linear and is more pronounced at higher values of the shrinkage thickness parameter δ_s than in the straight duct.

- Within the investigated Reynolds number range of 100–500, the Reynolds number has a minor effect on the relative variation rates of the Nusselt number ($\Delta\overline{Nu}/\overline{Nu}$, %) and entropy ($\Delta\bar{S}/\bar{S}$, %).

General Conclusion

This research focuses on enhancing heat transfer performance in duct heat exchangers. The objective is achieved through passive enhancement techniques based on the combined use of nanofluids and the insertion of a porous layer. The channel geometry consists of three sections and is partially filled with a centrally located porous layer positioned within the corrugated middle section between the inlet and outlet. The entrance and outlet sections are smooth and adiabatic, whereas the intermediate sinusoidal section is maintained at a constant temperature.

This study provides valuable insights into compact heat exchanger design by evaluating the effects of wall geometry, porous inserts, and nanofluids on heat transfer efficiency. Although the advantages of these passive techniques are clearly demonstrated, potential limitations, such as increased manufacturing complexity, stability issues associated with nanofluids and porous inserts, and higher costs, must also be taken into account.

This work comprises four main contributions.

The first contribution involves conducting a comprehensive bibliographic review on the subject, with the aim of identifying the physical and geometric parameters characterizing the underlying phenomena, the existing modeling approaches and their limitations, as well as practical implementations and technological application areas. In this review, both wavy and straight duct heat exchangers, either fully or partially filled with a porous medium, are examined. Relevant analytical, numerical, and experimental studies are systematically summarized and classified.

The proposed classification, presented in ten tables, highlights the key physical parameters associated with tube and channel heat exchangers and clearly illustrates the differences among the available modeling approaches. The identified parameters include the interfacial heat transfer treatment between the porous structure and the fluid, based on either local thermal non-equilibrium (LTNE) or local thermal equilibrium (LTE) models, as well as the flow modeling

approach within the porous medium, described using the Darcy, Darcy–Brinkman, or Darcy–Brinkman–Forchheimer formulations. Furthermore, for nanofluid applications, both single-phase and two-phase mixture models are considered.

Additionally, the present review addresses the following aspects:

- The relationships between geometric, structural, and physical properties and the key characteristic parameters of porous media are analyzed.
- The characteristics of foam media and packed granular porous media are specified and compared.
- The numerical methods commonly employed in the literature are identified, including the finite volume method (FVM), finite element method (FEM), finite difference method (FDM), lattice Boltzmann method (LBM), control volume-based collocated grid method (CVCGM), *bvp4c*, Runge–Kutta methods (RKM), semi-analytical differential iteration method (SADIM), and variational variational method (VVM).
- Common configurations of wavy and porous heat exchangers used in industrial applications are presented.
- The effects of porous inserts in both straight and wavy ducts are discussed.
- Various configurations of porous material inserts in ducts are illustrated, including porous layers attached to the wall (PLAW), centered porous layers (CPL), porous ribs attached to the wall (PRAW), local porous layers (LPL), partially filled porous materials (PFPM), and porous square pillars attached to the wall (PSPAW), among others.

Finally, the characteristic parameters of the corrugated walls are examined, with particular emphasis on the wavelength and amplitude.

The second contribution involves numerical simulations of a forced laminar flow under an imposed constant temperature condition applied to the corrugated surface of a wavy channel, while the remaining surfaces are considered adiabatic. The simulations focus on investigating the effects of porous layer thickness, Reynolds number, and nanoparticle volume fraction on the main heat transfer performance parameters of a corrugated channel characterized by a sinusoidal wall with a dimensionless amplitude of 0.15 and a dimensionless corrugation wavelength of 2.

The adopted physical model is based on a two-dimensional, laminar Darcy–Brinkman–Forchheimer formulation for nanofluid flow within a porous medium, coupled with a local thermal equilibrium (LTE) energy model that accounts for viscous dissipation. The model is validated through theoretical, numerical, and experimental comparisons with results reported in the literature.

Based on the numerical results obtained for a CuO/water nanofluid and an AISI 304 porous layer insert, the main conclusions of this investigation can be summarized as follows:

- The insertion of a porous layer significantly enhances both heat transfer and entropy generation. The average Nusselt number $\overline{Nu}$ and the average entropy generation rate $\bar{S}$ increase almost linearly with the porous layer thickness δ. Compared with the clear channel ($\delta = 0$), increases of 176.9% in $\overline{Nu}$ and 771.9% in $\bar{S}$ are observed for $\delta = 0.6$.
- The influence of the Reynolds number is more pronounced in porous channels than in clear channels. For $\delta = 0.4$, and at $Re = 500$, the porous channel exhibits increases of 108.4% in $\overline{Nu}$ and 309.1% in $\bar{S}$ compared to the clear channel.
- The nanoparticle volume fraction has a similar effect in both clear and porous channels. For a volume fraction of $\phi = 5\%$, the average Nusselt number increases by approximately 9%, while the average entropy generation increases by about 5%.

- A significant enhancement in heat transfer results from the combined interaction between the Reynolds number and the porous layer thickness, indicating a strong coupling effect between flow intensity and porous medium characteristics.

The third contribution focuses on the following key aspects: (i) heat transfer analysis of laminar nanofluid flow in a wavy channel heat exchanger, considering a clear channel partially filled with either packed granular material or metal foam; (ii) evaluation of the effects of the porous layer thickness δ and the Reynolds number Re on the Nusselt number, entropy generation, performance evaluation criterion (PEC), and hydrodynamic–thermal characteristics; and (iii) comparison of the thermal performance of porous wavy channels partially filled with packed granular media and metal foam.

Based on numerical simulations conducted over a Reynolds number range of $100 \leq Re \leq 400$ and a porous layer thickness range of $0.2 \leq \delta \leq 0.5$, using a silver–water nanofluid with a nanoparticle volume fraction of $\phi = 5\%$ and copper porous materials, the main conclusions are drawn. The structural properties of the metal foam are characterized by a porosity of $\varepsilon = 0.8$ and a pore density of 10 PPI, while the packed granular medium has a porosity of $\varepsilon = 0.373$. All simulations are performed under isothermal wall heating conditions. The primary conclusions of this investigation can be summarized as follows:

- The numerical results are in good agreement with those reported in prior studies.
- The insertion of porous media significantly enhances heat transfer, entropy generation, and the friction factor.
- The structure of the porous material strongly influences the thermal performance of the porous channel, with this effect being more pronounced for packed granular media than for metal foam.

- For Re=400 and within the range $\delta \in [0.2-0.5]$, the average Nusselt number ($\overline{Nu}$) increases by 43.04–134.64 %, while the entropy generation ($\bar{S}$) rises by 97.68–437.06 % compared with the clear channel when packed granular material is used. In contrast, metal foam exhibits more moderate enhancements, with increases of 36.19–94.53 % in $\overline{Nu}$ and 70.83–197.90 % in $\bar{S}$.

- The relative variation of the friction factor is nearly independent of the Reynolds number and shows only a slight increase with increasing δ.

The fourth contribution presents a numerical investigation of heat transfer and entropy generation in a wavy plate channel heat exchanger, in which the heated section is replaced by a convergent–divergent section with a sinusoidal profile. This numerical study of the newly proposed convergent–divergent configuration focuses on the effects of the shrinkage thickness parameter and the nanofluid Reynolds number. Based on the simulation results obtained using a CuO–water nanofluid, the main conclusions of this investigation can be summarized as follows:

- The shrinkage thickness parameter significantly enhances both heat transfer and entropy generation. The average Nusselt number ($\overline{Nu}$) and the average entropy generation ($\bar{S}$) increase almost linearly with the shrinkage thickness parameter (δ_s). At $Re = 500$, compared with the straight channel ($\delta_s = 0$), the convergent–divergent channel with $\delta_s = 0.8$ exhibits an increase of 82.7% in the average Nusselt number and 212.6% in the average entropy generation.

- Both the average Nusselt number (Nu) and the average entropy generation (S) increase with the Reynolds number. This quasi-linear trend becomes more pronounced at higher values of the shrinkage thickness parameter compared to the straight channel.

- A significant enhancement in heat transfer and entropy generation arises from the coupled effects of the flow Reynolds number and the shrinkage thickness parameter.

These findings contribute to a deeper understanding of efficient heat exchanger design based on convergent–divergent geometries.

- Future work will focus on unsteady heat transfer and turbulent flow regimes in porous wavy channels.

References

[1] X. Y. Yu, W. S. Huang, X. L. Liu, P. T. Liu, G. H. Tang, and X. L. Li, Thermal-hydraulic performance and optimization for finned-tube heat exchanger in gas wall-hung boilers, Applied Thermal Engineering, 262, 125241 (2025). https://doi.org/10.1016/j.applthermaleng.2024.125241.

[2] Y. Peng, Y. Tao, Z. Zhou, Y. Wang, and J. Tu, Experimental investigation on thermo-hydraulic performance of Al2O3–water, CuO–water and MWCNT–water in a double-tube helically coiled heat exchanger, International Journal of Thermal Sciences, 210, 109628 (2025). https://doi.org/10.1016/j.ijthermalsci.2024.109628.

[3] X. Liang, M. Min, K. Bian, and J. Cheng, Study on the enhanced heat transfer and exergy performance of the finned tube heat exchanger with vortex generator, International Journal of Thermal Sciences, 210, 109639 (2025). https://doi.org/10.1016/j.ijthermalsci.2024.109639.

[4] N. DiReda, A. Saha, G. D'Orazio, and S. Sobhani, Integrating bio-inspired morphologies into porous media burners: Experimental and computational insights on interphase heat exchange, International Journal of Heat and Mass Transfer, 237, 126295 (2025). https://doi.org/10.1016/j.ijheatmasstransfer.2024.126295.

[5] D. Hu, Q. Zhang, K. Song, C. Gao, K. Zhang, M. Su, and L. Wang, Performance optimization of a wavy finned-tube heat exchanger with staggered curved vortex generators, International Journal of Thermal Sciences, 183, 107830 (2023). https://doi.org/10.1016/j.ijthermalsci.2022.107830.

[6] K. Jin, A. B. Krishna, Z. Wong, P. S. Ayyaswamy, I. Catton, and T. S. Fisher, Thermohydraulic experiments on a supercritical carbon dioxide–air microtube heat exchanger, International Journal of Heat and Mass Transfer, 203, 123840 (2023). https://doi.org/10.1016/j.ijheatmasstransfer.2022.123840.

[7] Y. Ren, R. Jiang, P. Wang, W. Wu, Y. Yang, and Q. Yang, Experimental study of a rectangular microchannel printed circuit heat exchanger using supercritical carbon dioxide and water cooling, Applied Thermal Engineering, 262, 125230 (2025). https://doi.org/10.1016/j.applthermaleng.2024.125230.

[8] Y. Han, Y.-G. Wu, F.-L. Meng, C.-C. Zhang, Y.-T. Wu, X.-H. Wu, and T.-X. Jin, Multi-objective optimization study on heat transfer performance of solar salt in non-circular twisted tube heat exchanger based on entropy generation number and NSGA II, International Journal of Thermal Sciences, 211, 109681 (2025). https://doi.org/10.1016/j.ijthermalsci.2025.109681.

[9] J. A. Crespo-Quintanilla, J. L. García-Castillo, J. I. Minchaca-Mojica, and M. Picón-Núñez, Enhancing heat exchanger performance with combined twisted tubes and twisted Tapes: Design and retrofit strategies, Thermal Science and Engineering Progress, 54, 102817 (2024). https://doi.org/10.1016/j.tsep.2024.102817.

[10] T. W. B. Riyadi, S. G. Herawan, A. Tirta, Y. J. Ee, A. L. Hananto, P. A. Paristiawan, A. A. Yusuf, H. Venu, Irianto, and I. Veza, Nanofluid heat transfer and machine learning: Insightful review of machine learning for nanofluid heat transfer enhancement in porous media and heat exchangers as sustainable and renewable energy solutions, Results in Engineering, 24, 103002 (2024). https://doi.org/10.1016/j.rineng.2024.103002.

[11] H. Roueintan, and A. Fattahi, On the pillow-plate heat exchanger with wavy walls and filled with a hybrid nanofluid: Numerical simulation and data-assisted prediction, Case Studies in Thermal Engineering, 64, 105495 (2024). https://doi.org/10.1016/j.csite.2024.105495.

[12] S. M. H. Hashemi, S. A. Fazeli, and H. Shokouhmand, Fully developed non-Darcian forced convection slip-flow in a micro-annulus filled with a porous medium: Analytical solution, Energy Conversion and Management, 52(2), 1054-1060 (2011). https://doi.org/10.1016/j.enconman.2010.08.034.

[13] O. D. Makinde, and E. Osalusi Second Law Analysis of Laminar Flow In A Channel Filled With Saturated Porous Media. Entropy, 2005. 7, 148-160 DOI: 10.3390/e7020148.

[14] T. W. Ting, Y. Hung, M. Osman, and P. Yek, Heat and Flow Characteristics of Nanofluid Flow in Porous Microchannels, International Journal of Automotive and Mechanical Engineering, 15, 5238-5250 (2018).10.15282/ijame.15.2.2018.7.0404.

[15] W. Lu, C. Y. Zhao, and S. A. Tassou, Thermal analysis on metal-foam filled heat exchangers. Part I: Metal-foam filled pipes, International Journal of Heat and Mass Transfer, 49(15), 2751-2761 (2006). https://doi.org/10.1016/j.ijheatmasstransfer.2005.12.012.

[16] K. Yang, W. Huang, X. Li, and J. Wang Analytical Analysis of Heat Transfer and Entropy Generation in a Tube Filled with Double-Layer Porous Media. Entropy, 2020. 22, DOI: 10.3390/e22111214.

[17] X. Bai, F. Kuwahara, M. Mobedi, and A. Nakayama, Forced Convective Heat Transfer in a Channel Filled With a Functionally Graded Metal Foam Matrix, Journal of Heat Transfer, 140(11), (2018).10.1115/1.4040613.

[18] M. Dehghan, M. T. Jamal-Abad, and S. Rashidi, Analytical interpretation of the local thermal non-equilibrium condition of porous media imbedded in tube heat exchangers, Energy Conversion and Management, 85, 264-271 (2014). https://doi.org/10.1016/j.enconman.2014.05.074.

[19] P. Li, J. Zhong, K. Wang, and C. Zhao, Analysis of thermally developing forced convection heat transfer in a porous medium under local thermal non-equilibrium condition: A circular tube with asymmetric entrance temperature, International Journal of Heat and Mass Transfer, 127, 880-889 (2018). https://doi.org/10.1016/j.ijheatmasstransfer.2018.08.081.

[20] O. H. Hassan, G. I. Sultan, M. N. Sabry, and A. A. Hegazi, Investigation of heat transfer and pressure drop in a porous media with internal heat generation, Case Studies in Thermal Engineering, 32, 101849 (2022). https://doi.org/10.1016/j.csite.2022.101849.

[21] P. X. Jiang, and X.-C. Lu, Numerical simulation of fluid flow and convection heat transfer in sintered porous plate channels, International Journal of Heat and Mass Transfer, 49(9), 1685-1695 (2006). https://doi.org/10.1016/j.ijheatmasstransfer.2005.10.026.

[22] P. X. Jiang, and Z.-P. Ren, Numerical investigation of forced convection heat transfer in porous media using a thermal non-equilibrium model, International Journal of Heat and Fluid Flow, 22(1), 102-110 (2001). https://doi.org/10.1016/S0142-727X(00)00066-7.

[23] C. Peng, T. Ming, and Y. Tao, Thermal and hydraulic performances of a tube filled with various thermal conductivities of porous media, International Journal of Heat and Mass Transfer, 81, 784-796 (2015). https://doi.org/10.1016/j.ijheatmasstransfer.2014.10.073.

[24] P. M. Kamath, C. Balaji, and S. P. Venkateshan, Experimental investigation of flow assisted mixed convection in high porosity foams in vertical channels, International Journal of Heat and Mass Transfer, 54(25), 5231-5241 (2011). https://doi.org/10.1016/j.ijheatmasstransfer.2011.08.020.

[25] M. Siavashi, H. R. Talesh Bahrami, and E. Aminian, Optimization of heat transfer enhancement and pumping power of a heat exchanger tube using nanofluid with

gradient and multi-layered porous foams, Applied Thermal Engineering, 138, 465-474 (2018). https://doi.org/10.1016/j.applthermaleng.2018.04.066.

[26] E. Aminian, H. Moghadasi, and H. Saffari, Magnetic field effects on forced convection flow of a hybrid nanofluid in a cylinder filled with porous media: a numerical study, Journal of Thermal Analysis and Calorimetry, 141(5), 2019-2031 (2020).10.1007/s10973-020-09257-y.

[27] Z. Alhajaj, A. M. Bayomy, M. Z. Saghir, and M. M. Rahman, Flow of nanofluid and hybrid fluid in porous channels: Experimental and numerical approach, International Journal of Thermofluids, 1-2, 100016 (2020). https://doi.org/10.1016/j.ijft.2020.100016.

[28] H. Moghadasi, E. Aminian, H. Saffari, M. Mahjoorghani, and A. Emamifar, Numerical analysis on laminar forced convection improvement of hybrid nanofluid within a U-bend pipe in porous media, International Journal of Mechanical Sciences, 179, 105659 (2020). https://doi.org/10.1016/j.ijmecsci.2020.105659.

[29] T. Fiedler, and N. Movahedi Compact Aluminium Foam Heat Exchangers. Metals, 2023. 13, DOI: 10.3390/met13081440.

[30] K. Wang, Q. Wang, and P. Li, Forced convection in a fully-filled bidisperse porous annular duct subject to asymmetric heat fluxes, Thermal Science and Engineering Progress, 32, 101328 (2022). https://doi.org/10.1016/j.tsep.2022.101328.

[31] D. Poulikakos, and M. Kazmierczak, Forced Convection in a Duct Partially Filled With a Porous Material, Journal of Heat Transfer, 109(3), 653-662 (1987).10.1115/1.3248138.

[32] A. A. Mohamad, Heat transfer enhancements in heat exchangers fitted with porous media Part I: constant wall temperature, International Journal of Thermal Sciences, 42(4), 385-395 (2003). https://doi.org/10.1016/S1290-0729(02)00039-X.

[33] T. V. Morosuk, Entropy generation in conduits filled with porous medium totally and partially, International Journal of Heat and Mass Transfer, 48(12), 2548-2560 (2005). https://doi.org/10.1016/j.ijheatmasstransfer.2005.01.018.

[34] K. T. Yang, and K. J. J. o. H. T.-t. o. T. A. Vafai, Restrictions on the Validity of the Thermal Conditions at the Porous-Fluid Interface - An Exact Solution, 133, 112601 (2011).

[35] C. Yang, A. Nakayama, and W. Liu, Heat transfer performance assessment for forced convection in a tube partially filled with a porous medium, International Journal of

Thermal Sciences, 54, 98-108 (2012). https://doi.org/10.1016/j.ijthermalsci.2011.10.023.

[36] Y. Mahmoudi, N. Karimi, and K. Mazaheri, Analytical investigation of heat transfer enhancement in a channel partially filled with a porous material under local thermal non-equilibrium condition: Effects of different thermal boundary conditions at the porous-fluid interface, International Journal of Heat and Mass Transfer, 70, 875-891 (2014). https://doi.org/10.1016/j.ijheatmasstransfer.2013.11.048.

[37] N. Karimi, D. Agbo, A. Talat Khan, and P. L. Younger, On the effects of exothermicity and endothermicity upon the temperature fields in a partially-filled porous channel, International Journal of Thermal Sciences, 96, 128-148 (2015). https://doi.org/10.1016/j.ijthermalsci.2015.05.002.

[38] M. Torabi, K. Zhang, G. Yang, J. Wang, and P. Wu, Heat transfer and entropy generation analyses in a channel partially filled with porous media using local thermal non-equilibrium model, Energy, 82, 922-938 (2015). https://doi.org/10.1016/j.energy.2015.01.102.

[39] M. Torabi, N. Karimi, and K. Zhang, Heat transfer and second law analyses of forced convection in a channel partially filled by porous media and featuring internal heat sources, Energy, 93, 106-127 (2015). https://doi.org/10.1016/j.energy.2015.09.010.

[40] M. Torabi, C. Dickson, and N. Karimi, Theoretical investigation of entropy generation and heat transfer by forced convection of copper–water nanofluid in a porous channel -Local thermal non-equilibrium and partial filling effects, Powder Technology, 301, 234-254 (2016). https://doi.org/10.1016/j.powtec.2016.06.017.

[41] C. Dickson, M. Torabi, and N. Karimi, First and second law analyses of nanofluid forced convection in a partially-filled porous channel – The effects of local thermal non-equilibrium and internal heat sources, Applied Thermal Engineering, 103, 459-480 (2016). https://doi.org/10.1016/j.applthermaleng.2016.04.095.

[42] M. F. Baig, G. M. Chen, and C. P. Tso The Thermal Performance Analysis of an Al2O3-Water Nanofluid Flow in a Composite Microchannel. Nanomaterials, 2022. 12, DOI: 10.3390/nano12213821.

[43] M. Hajipour, and A. Molaei Dehkordi, Mixed-convection flow of Al2O3–H2O nanofluid in a channel partially filled with porous metal foam: Experimental and numerical study, Experimental Thermal and Fluid Science, 53, 49-56 (2014). https://doi.org/10.1016/j.expthermflusci.2013.11.002.

[44] M. Torabi, M. Torabi, S. M. Ghiaasiaan, and G. P. Peterson, The effect of Al2O3-water nanofluid on the heat transfer and entropy generation of laminar forced convection through isotropic porous media, International Journal of Heat and Mass Transfer, 111, 804-816 (2017). https://doi.org/10.1016/j.ijheatmasstransfer.2017.04.041.

[45] M. Siavashi, H. R. Talesh Bahrami, and H. Saffari, Numerical investigation of flow characteristics, heat transfer and entropy generation of nanofluid flow inside an annular pipe partially or completely filled with porous media using two-phase mixture model, Energy, 93, 2451-2466 (2015). https://doi.org/10.1016/j.energy.2015.10.100.

[46] M. Siavashi, H. R. Talesh Bahrami, E. Aminian, and H. Saffari, Numerical analysis on forced convection enhancement in an annulus using porous ribs and nanoparticle addition to base fluid, Journal of Central South University, 26(5), 1089-1098 (2019).10.1007/s11771-019-4073-z.

[47] Z. Ying, B. He, L. Su, and Y. Kuang, Thermo-hydraulic analyses of the absorber tube with molten salt-based nanofluid and porous medium inserts, Solar Energy, 226, 20-30 (2021). https://doi.org/10.1016/j.solener.2021.08.021.

[48] B. I. Pavel, and A. A. Mohamad, An experimental and numerical study on heat transfer enhancement for gas heat exchangers fitted with porous media, International Journal of Heat and Mass Transfer, 47(23), 4939-4952 (2004). https://doi.org/10.1016/j.ijheatmasstransfer.2004.06.014.

[49] Z. F. Huang, A. Nakayama, K. Yang, C. Yang, and W. Liu, Enhancing heat transfer in the core flow by using porous medium insert in a tube, International Journal of Heat and Mass Transfer, 53(5), 1164-1174 (2010). https://doi.org/10.1016/j.ijheatmasstransfer.2009.10.038.

[50] J. Y. Jang, and J. L. Chen, Forced convection in a parallel plate channel partially filled with a high porosity medium, International Communications in Heat and Mass Transfer, 19(2), 263-273 (1992). https://doi.org/10.1016/0735-1933(92)90037-I.

[51] T.-C. Jen, and T. Z. Yan, Developing fluid flow and heat transfer in a channel partially filled with porous medium, International Journal of Heat and Mass Transfer, 48(19), 3995-4009 (2005). https://doi.org/10.1016/j.ijheatmasstransfer.2005.04.021.

[52] M. E. Nimvari, M. Maerefat, and M. K. El-Hossaini, Numerical simulation of turbulent flow and heat transfer in a channel partially filled with a porous media, International Journal of Thermal Sciences, 60, 131-141 (2012). https://doi.org/10.1016/j.ijthermalsci.2012.05.016.

[53] H. Shokouhmand, F. Jam, and M. R. Salimpour, The effect of porous insert position on the enhanced heat transfer in partially filled channels, International Communications in Heat and Mass Transfer, 38(8), 1162-1167 (2011). https://doi.org/10.1016/j.icheatmasstransfer.2011.04.027.

[54] Y. Mahmoudi, and N. Karimi, Numerical investigation of heat transfer enhancement in a pipe partially filled with a porous material under local thermal non-equilibrium condition, International Journal of Heat and Mass Transfer, 68, 161-173 (2014). https://doi.org/10.1016/j.ijheatmasstransfer.2013.09.020.

[55] M. A. Al-Nimr, and M. K. Alkam, Unsteady Non-Darcian Forced Convection Analysis in an Annulus Partially Filled With a Porous Material, Journal of Heat Transfer, 119(4), 799-804 (1997).10.1115/1.2824185.

[56] M. Mahdavi, M. Saffar-Avval, S. Tiari, and Z. Mansoori, Entropy generation and heat transfer numerical analysis in pipes partially filled with porous medium, International Journal of Heat and Mass Transfer, 79, 496-506 (2014). https://doi.org/10.1016/j.ijheatmasstransfer.2014.08.037.

[57] M. A. Teamah, W. M. El-Maghlany, and M. M. Khairat Dawood, Numerical simulation of laminar forced convection in horizontal pipe partially or completely filled with porous material, International Journal of Thermal Sciences, 50(8), 1512-1522 (2011). https://doi.org/10.1016/j.ijthermalsci.2011.03.003.

[58] C.-S. Wang, P.-Y. Shen, and T.-M. Liou, Evaluation of porous rib and flow pulsation on microchannel thermal performance using a novel thermal lattice Boltzmann method, International Journal of Thermal Sciences, 172, 107345 (2022). https://doi.org/10.1016/j.ijthermalsci.2021.107345.

[59] A. Iranmanesh, and S. A. Moshizi, Flow and Heat Transfer Study of an Annulus Partially Filled with Metallic Foam on Two Wall Surfaces Subject to Asymmetrical Heat Fluxes, Arabian Journal for Science and Engineering, 49(2), 1567-1584 (2024).10.1007/s13369-023-07895-6.

[60] R. M. K. Ali, and S. Lafta Ghashim, Numerical analysis of the heat transfer enhancement by using metal foam, Case Studies in Thermal Engineering, 49, 103336 (2023). https://doi.org/10.1016/j.csite.2023.103336.

[61] P. H. Jadhav, N. Gnanasekaran, D. A. Perumal, and M. Mobedi, Performance evaluation of partially filled high porosity metal foam configurations in a pipe, Applied

Thermal Engineering, 194, 117081 (2021). https://doi.org/10.1016/j.applthermaleng.2021.117081.

[62] C. C. Wang, and C. K. Chen, Forced convection in a wavy-wall channel, International Journal of Heat and Mass Transfer, 45(12), 2587-2595 (2002). https://doi.org/10.1016/S0017-9310(01)00335-0.

[63] E. Aslan, I. Taymaz, and Y. İslamoğlu, Finite volume simulation for convective heat transfer in wavy channels, Heat and Mass Transfer, 52, (2015).10.1007/s00231-015-1571-x.

[64] T. Ma, L.-x. Du, N. Sun, M. Zeng, B. Sundén, and Q.-w. Wang, Experimental and numerical study on heat transfer and pressure drop performance of Cross-Wavy primary surface channel, Energy Conversion and Management, 125, 80-90 (2016). https://doi.org/10.1016/j.enconman.2016.06.055.

[65] S. Pati, S. K. Mehta, and A. Borah, Numerical investigation of thermo-hydraulic transport characteristics in wavy channels: Comparison between raccoon and serpentine channels, International Communications in Heat and Mass Transfer, 88, 171-176 (2017). https://doi.org/10.1016/j.icheatmasstransfer.2017.09.001.

[66] L. Zhang, and D. Che, Influence of Corrugation Profile on the Thermalhydraulic Performance of Cross-Corrugated Plates, Numerical Heat Transfer, Part A: Applications, 59(4), 267-296 (2011).10.1080/10407782.2011.540963.

[67] H. A. Mohammed, P. Gunnasegaran, and N. H. Shuaib, Numerical simulation of heat transfer enhancement in wavy microchannel heat sink, International Communications in Heat and Mass Transfer, 38(1), 63-68 (2011). https://doi.org/10.1016/j.icheatmasstransfer.2010.09.012.

[68] P. Naphon, and K. Kornkumjayrit, Numerical analysis on the fluid flow and heat transfer in the channel with V-shaped wavy lower plate, International Communications in Heat and Mass Transfer, 35(7), 839-843 (2008). https://doi.org/10.1016/j.icheatmasstransfer.2008.03.010.

[69] L. Yang, K. Du, and Z. Zhang Heat transfer and flow optimization of a novel sinusoidal minitube filled with non-Newtonian SiC/EG-water nanofluids, International Journal of Mechanical Sciences, 168, 105310 (2020). https://doi.org/10.1016/j.ijmecsci.2019.105310.

[70] M. N. Fares, M. AL-Saad, H. H. J. Almutter, D. J. Jasim, M. A. Fazilati, S. Salahshour, Sh. Baghaei, Two-phase analysis of heat transfer of nanofluid flow in a wavy channel

heat exchanger: A numerical approach, International Journal of Thermofluids, 23, 100786, (2024). https://doi.org/10.1016/j.ijft.2024.100786

[71] R. Dormohammadi, M. Farzaneh-Gord, A. Ebrahimi-Moghadam, and M. H. Ahmadi, Heat transfer and entropy generation of the nanofluid flow inside sinusoidal wavy channels, Journal of Molecular Liquids, 269, 229-240 (2018). https://doi.org/10.1016/j.molliq.2018.07.119.

[72] J. A. Esfahani, M. Akbarzadeh, S. Rashidi, M. A. Rosen, and R. Ellahi, Influences of wavy wall and nanoparticles on entropy generation over heat exchanger plat, International Journal of Heat and Mass Transfer, 109, 1162-1171 (2017). https://doi.org/10.1016/j.ijheatmasstransfer.2017.03.006.

[73] P. Valinataj-Bahnemiri, A. Ramiar, S. A. Manavi, and A. Mozaffari, Heat transfer optimization of two phase modeling of nanofluid in a sinusoidal wavy channel using Artificial Bee Colony technique, Engineering Science and Technology, an International Journal, 18(4), 727-737 (2015). https://doi.org/10.1016/j.jestch.2015.05.005.

[74] J. Rostami, A. Abbassi, and J. Harting, Heat transfer by nanofluids in wavy microchannels, Advanced Powder Technology, 29(4), 925-933 (2018). https://doi.org/10.1016/j.apt.2018.01.010.

[75] S. Mirmasoumi, and A. Behzadmehr, Numerical study of laminar mixed convection of a nanofluid in a horizontal tube using two-phase mixture model, Applied Thermal Engineering, 28(7), 717-727 (2008). https://doi.org/10.1016/j.applthermaleng.2007.06.019.

[76] Y. Azizi, M. Bahramkhoo, and A. Kazemi, Influence of non-uniform magnetic field on the thermal efficiency hydrodynamic characteristics of nanofluid in double pipe heat exchanger, Scientific Reports, 13(1), 407 (2023).10.1038/s41598-022-26285-w.

[77] R. Hamid, and Z. Mehrdoost, Thermal performance enhancement of multiple tubes latent heat thermal energy storage system using sinusoidal wavy fins and tubes geometry modification, Applied Thermal Engineering, 245, 122750 (2024).n https://doi.org/10.1016/j.applthermaleng.2024.122750.

[78] A. Shahsavar, A. H. Majidzadeh, R. B. Mahani, and P. Talebizadehsardari, Entropy and thermal performance analysis of PCM melting and solidification mechanisms in a wavy channel triplex-tube heat exchanger, Renewable Energy, 165, 52-72 (2021). https://doi.org/10.1016/j.renene.2020.11.074.

[79] M. Akbarzadeh, and M. J. Maghrebi, Combined effects of corrugated walls and porous inserts on performance improvement in a heat exchanger channel, International Journal of Thermal Sciences, 127, 266-276 (2018). https://doi.org/10.1016/j.ijthermalsci.2018.01.010.

[80] M. Akbarzadeh, S. Rashidi, N. Karimi, and N. Omar, First and second laws of thermodynamics analysis of nanofluid flow inside a heat exchanger duct with wavy walls and a porous insert, Journal of Thermal Analysis and Calorimetry, 135(1), 177-194 (2019).10.1007/s10973-018-7044-y.

[81] E. Aminian, H. Moghadasi, H. Saffari, and A. M. Gheitaghy Investigation of Forced Convection Enhancement and Entropy Generation of Nanofluid Flow through a Corrugated Minichannel Filled with a Porous Media. Entropy, 2020. 22, DOI: 10.3390/e22091008.

[82] S. Nazari, and D. Toghraie, Numerical simulation of heat transfer and fluid flow of Water-CuO Nanofluid in a sinusoidal channel with a porous medium, Physica E: Low-dimensional Systems and Nanostructures, 87, 134-140 (2017). https://doi.org/10.1016/j.physe.2016.11.035.

[83] H. R. Ashorynejad, and A. Zarghami, Magnetohydrodynamics flow and heat transfer of Cu-water nanofluid through a partially porous wavy channel, International Journal of Heat and Mass Transfer, 119, 247-258 (2018). https://doi.org/10.1016/j.ijheatmasstransfer.2017.11.117.

[84] A. Mezaache, F. Mebarek-Oudinal, H. Vaidya, and K. Ramesh, Impact of nanofluids and porous structures on the thermal efficiency of wavy channel heat exchanger, International Journal of Thermal Sciences, 210, 109673 (2025). https://doi.org/10.1016/j.ijthermalsci.2024.109673.

[85] R. N. Konduru, O. Farges, V. Schick, P. Hairy, Y. Gaillard, and G. Parent, Experimental and numerical investigation of porous heat exchangers with Kelvin cell structured foam at high temperatures: Coupled conduction-convection and radiation heat transfer, International Journal of Heat and Mass Transfer, 224, 125253 (2024). https://doi.org/10.1016/j.ijheatmasstransfer.2024.125253.

[86] X.-s. Shang, W. Shao, R. Wang, Z. Miao, H.-q. Cao, B.-c. Wang, and Z. Cui, Numerical and thermal resistance analysis on the cryogenic porous medium heat exchanger with liquid channel, International Journal of Thermal Sciences, 204, 109217 (2024). https://doi.org/10.1016/j.ijthermalsci.2024.109217.

[87] N. Delalic, D. Mulahasanovic, and E. N. Ganic, Porous media compact heat exchanger unit - experiment and analysis, Experimental Thermal and Fluid Science, 28(2), 185-192 (2004). https://doi.org/10.1016/S0894-1777(03)00038-4.

[88] X.-W. Tian, S.-Z. Zhang, C. Sun, and W. Wang, Heat transfer enhancement in cold plates with wavy channels via free-shape modeling and optimization, International Journal of Thermal Sciences, 193, 108446 (2023). https://doi.org/10.1016/j.ijthermalsci.2023.108446.

[89] M. Qu, Y. Zhang, X. Zhang, H. Mu, W. Fan, X. Chen, and Q. Tan, Numerical analysis of the effect of wave amplitude on thermohydraulic performance in a heat exchanger with sinusoidal wavy channels, International Communications in Heat and Mass Transfer, 155, 107582 (2024). https://doi.org/10.1016/j.icheatmasstransfer.2024.107582.

[90] H. A. Amiri, F. Afsharpanah, S. Moshafi, and S. Asiaei, Thermal management of an asymmetrical wavy microchannel heat sink via Ag/water nanofluid, Case Studies in Thermal Engineering, 53, 103857 (2024). https://doi.org/10.1016/j.csite.2023.103857.

[91] T. a. Rush, T. a. Newell, and A. m. Jacobi, An experimental study of flow and heat transfer in sinusoidal wavy passages, International Journal of Heat and Mass Transfer, 42(9), 1541-1553 (1999). https://doi.org/10.1016/S0017-9310(98)00264-6.

[92] M. A. Said, H. Togun, A. M. Abed, N. Biswas, H. I. Mohammed, H. S. Sultan, J. M. Mahdi, and P. Talebizadehsardari, Evaluation of wavy wall configurations for accelerated heat recovery in triplex-tube energy storage units for building heating applications, Journal of Building Engineering, 94, 109762 (2024). https://doi.org/10.1016/j.jobe.2024.109762.

[93] F. Mebarek-Oudina, M. Bouselsal, N. Biswas, H. Vaidya, K. Ramesh, Heat transfer in a zigzag wall cavity and different obstacles filled with MgO-SWCNT/water hybrid nanofluids, Modern Physics Letters B, (2025) 2550163. https://doi.org/10.1142/S0217984925501635

[94] S. Marzougui, F. Mebarek-Oudina, A. Aissa, M. Magherbi, Z. Shah, K. Ramesh, Entropy Generation on Magneto-Convective Flow of Copper-Water Nanofluid in a Cavity with Chamfers, Journal of Thermal Analysis and Calorimetry, 143 (3) (2021) 2203-2214, https://doi.org/10.1007/s10973-020-09662-3

[95] S. Marzougui, F. Mebarek-Oudina, A. Mchirgui, and M. Magherbi, Entropy Generation and Heat transport of Cu-water Nanoliquid in Porous lid-driven Cavity through

Magnetic Field, International Journal of Numerical Methods for Heat & Fluid Flow, 32 (6), 2022, 2047-2069. https://doi.org/10.1108/HFF-04-2021-0288

[96] Ould Said, B., Mebarek-Oudina F. and Medebber, M. A. (2024) "Magneto-hydro-Convective Nanofluid flow in Porous Square Enclosure", Frontiers in Heat and Mass Transfer, 22(5): 1343-1360. https://doi.org/10.32604/fhmt.2024.054164

[97] F. Berrahil, A. Filali, F. Mebarek-Oudina, S. Benissaad, S. U. Khan, C. Abid, S. Saouli, Y. Demagh, Analysis of Enhanced Magnetohydrodynamic Natural Convection in a Non-Darcy Porous Cavity with Alumina-Water Fluid and Conductive Baffles, International Journal of Numerical Methods for Heat and Fluid Flow, 2025, https://doi.org/10.1108/HFF-01-2025-0026

[98] A.S. Warke, K. Ramesh, F. Mebarek-Oudina, and A. Abidi, Numerical investigation of the stagnation point flow of radiative magnetomicropolar liquid past a heated porous stretching sheet, Journal of Thermal Analysis and Calorimetry, 2022, 147(12), pp. 6901–6912 https://doi.org/10.1007/s10973-021-10976-z

[99] Dharmaiah, G.; Mebarek-Oudina, F.; Balamurugan, K.S.; Vedavathi, N. Numerical Analysis of the Magnetic Dipole Effect on a Radiative Ferromagnetic Liquid Flowing over a Porous Stretched Sheet. Fluid Dyn. Mater. Process. 20(2), 293–310 (2024). https://doi.org/10.32604/fdmp.2023.030325.

[100] R. Madan Kumar, R. Srinivasa Raju, F. Mebarek-Oudina, M. Anil Kumar, Vamsi Krishna Narla, Cross-Diffusion effects on a MHD Williamson Nanofluid flow past a nonlinear stretching sheet immersed in a permeable medium. Frontiers in Heat and Mass Transfer, 22 (1), 15-34 (2024). https://doi.org/10.32604/fhmt.2024.048045

[101] M. Anil kumar, F. Mebarek-Oudina, P. Mangathai, N. A. Shah, Ch. Vijayabhaskar, N. Venkatesh, Y. Fouad, The Impact of Soret Dufour and Radiation on the Laminar Flow of a Rotating liquid past a Porous plate via Chemical Reaction, Modern Physics Letters B, 39(10) (2025) 2450458, https://doi.org/10.1142/S021798492450458X

[102] Gangadharaiah Y. H., Manjunatha N., Mebarek-Oudina F. The variable viscosity and variable gravity field on the onset of convective motion in a porous layer with through flow. Mathematical Modeling and Computing, 11(1), 19–26 (2024). https://doi.org/10.23939/mmc2024.01.019

[103] F. Mebarek-Oudina, N. Keerthi Reddy and M. Sankar, Heat Source location Effects on Buoyant Convection of Nanofluids in an Annulus, Advances in Fluid Dynamics,

Lecture Notes in Mechanical Engineering, pp. 923-937, 2021. https://doi.org/10.1007/978-981-15-4308-1_70

[104] J. Raza, F. Mebarek-Oudina and L. Ali Lund, The flow of magnetised convective Casson liquid via a porous channel with shrinking and stationary walls, Pramana - Journal of Physics, 2022, 96, 229. https://doi.org/10.1007/s12043-022-02465-1

[105] M. A. Borhani, A. S. Shirani, M. Talebi, J. Mokhtari, Heat transfer evaluation of combined nanofluids in vertical annulus: An experimental and artificial neural network approach, Progress in Nuclear Energy, Volume 175, October 2024, 105339, https://doi.org/10.1016/j.pnucene.2024.105339

[106] F. Mebarek-Oudina, Convective Heat Transfer of Titania Nanofluids of different base fluids in Cylindrical Annulus with discrete Heat Source, Heat Transfer-Asian Research, 48(2019) 135-147. https://doi.org/10.1002/htj.21375

[107] J. L. R. Prasad, F. Mebarek-Oudina, G. Dharmaiah, P. B. Rao, H. Vaidya, Melting Flow Analyzation of Radiative Riga plate Two-Phase Nano-Fluid across non-Flatness plane with Chemical Reaction, Frontiers in Heat and Mass Transfer, 22(5), (2024) 1515-1532. https://doi.org/10.32604/fhmt.2024.057854

[108] T. Naseem, A. Shahzad, F. Mebarek-Oudina, and Shakil Shaiq, Entropy analysis of Al2O3/water nanofluid in viscous fluid flow with Joule heating and viscous dissipation over a permeable radiated stretching disk: a comparative study of nanoparticle shapes, CFD Simulation, 10 (2025) 261-287. https://doi.org/10.1515/9783111405094-010

[109] J. Raza, F. Mebarek-Oudina & O. D. Makinde, MHD Slip flow of Cu-Kerosene Nanofluid in a Channel with Stretching Walls using 3-stage Lobatto IIIA formula, Defect and Diffusion Forum, 387(2018) 51-62. http://dx.doi.org/10.4028/www.scientific.net/DDF.387.51

[110] B. Ould Said, F. Mebarek-Oudina, and H. Vaidya, Magnetized nanofluids flow in porous enclosures containing elliptical cylinder of varying aspect ratios, CFD Simulation, 12 (2025) 319-334. https://doi.org/10.1515/9783111405094-012

[111] G. Ramasekhar, F. Mebarek-Oudina, S. Suneetha, H. Vaidya, P. D. Selvi, Computational simulation of Casson hybrid nanofluid flow with Rosseland approximation and uneven heat source/sink, International Journal of Thermofluids, 24, (2024) 100893. https://doi.org/10.1016/j.ijft.2024.100893

[112] A. Ashique, U. Afzal, S. Abdal, S. Ullah, N. A. Shah, J. D. Chung, Optimization of thermal transfer in Casson hybrid nanofluids with magnetohydrodynamics and

activation energy effects, Alexandria Engineering Journal, Volume 122, May 2025, Pages 255-26, https://doi.org/10.1016/j.aej.2025.02.067

[113] F. Mebarek-Oudina, I. Chabani, H. Vaidya, A. I. Ismail, Hybrid nanofluid magneto-convective flow and porous media contribution to entropy generation, International Journal of Numerical Methods for Heat & Fluid Flow, 34(2), 809-836(2024). https://doi.org/10.1108/HFF-06-2023-0326

[114] R. Vidhya, B. S. Kumar, T. Balakrishnan, G. Navaneethakrishnan, R. Palanisamy, M. Alwetaishi, H. Fayaz, Q.M. Al-Mdallal, S. Dixit Heat transfer enhancement in cylindrical heat pipes with MgO-Al_2O_3 hybrid nanofluids in water-ethylene glycol mixture: An RSM approach, Case Studies in Thermal Engineering, Volume 63, November 2024, 105278, https://doi.org/10.1016/j.csite.2024.105278

[115] F. Mebarek-Oudina and A. Aissa, Convective Heat Transfer of Magneto flow of Fe3O4-MWCNT/H2O Hybrid Nanofluid in a Porous Space between Two Concentric Cylinders", De Gruyter Series on the Applications of Mathematics in Engineering and Information Sciences (DeGryter), 55-74, 2021, https://doi.org/10.1515/9783110696080-003

[116] Mourad, A. Aissa, A.M. Abed, D. Toghraie, O.A. Akbari, K. Guedri, O. Younis, R. Marzouki, MHD natural convection of Fe_3O_4- MWCNT/Water hybrid nanofluid filled in a porous annulus between a circular cylinder and Koch snowflake, Alexandria Engineering, Journal, Volume 65, 15 February 2023, Pages 367-382, https://doi.org/10.1016/j.aej.2022.09.035

[117] A.M. Alklaibi, L. S. Sundar, K.V.V.C. Mouli, Experimental investigation on the performance of hybrid Fe_3O_4 coated MWCNT/Water nanofluid as a coolant of a Plate heat exchanger, International Journal of Thermal Sciences, Volume 171, January 2022, 107249, https://doi.org/10.1016/j.ijthermalsci.2021.107249

[118] F. Mebarek-Oudina, R. Fares, R. Choudhari Convection Heat Transfer of MgO-Ag /Water Magneto-Hybrid Nanoliquid Flow into a Special Porous Enclosure. Algerian Journal of Renewable Energy and Sustainable Development, 2020, 2(2), 84-95. https://doi.org/10.46657/ajresd.2020.2.2.1

[119] N. S. Anuar, N. Bachok, I. Pop, Influence of buoyancy force on Ag-MgO/water hybrid nanofluid flow in an inclined permeable stretching/shrinking sheet, International Communications in Heat and Mass Transfer, Volume 123, April 2021, 105236, https://doi.org/10.1016/j.icheatmasstransfer.2021.105236

[120] F. A. Abood, Z. K. Radhi, A. K. Hadi, R. Z. Homod, H. I. Mohammed, MHD mixed convection of nanofluid flow Ag- Mgo/water in a channel contain a rotational cylinder, International Journal of Thermofluids, Volume 22, May 2024, 100713, https://doi.org/10.1016/j.ijft.2024.100713

[121] F. Mebarek-Oudina, A. K. Hussein, O. Younis, S. Rostami, R. Nikbakhti, Natural Convection Enhancement in the Annuli Between Two Homocentric Cylinders by using Ethylene Glycol / Water based Titania nanofluid, Journal of Advanced Research in Fluid Mechanics and Thermal Sciences, 80 (2) (2021) 56-73. https://doi.org/10.37934/arfmts.80.2.5673

[122] P. Zhao, L. Huang, J. Hou, Z. Ding, L Ma, J. Wu, D. Li, Y. Yao, Z. Chen, N. Hao, Microfluidic one-step and large-scale production of silica and titania nanofluids toward phase-change heat transfer intensification of power electronic devices, Chemical Engineering Journal, Volume 503, 2025, 158227, https://doi.org/10.1016/j.cej.2024.158227

[123] A. B. Mahfouz, A. Ali, M. Mubashir, A. S. Hanbazazah, M. Alsaady [a], P. L. Show, Optimization of viscosity of titania nanotubes ethylene glycol/water-based nanofluids using response surface methodology, Fuel, Volume 347, 2023, 128334, https://doi.org/10.1016/j.fuel.2023.128334

[124] F. Mebarek-Oudina, CFD Simulation: Thermo-Fluids and Nanofluids in Engineering and Biomedicine, 1st edition, De-Gruyter, 2025, https://doi.org/10.1515/9783111405094

[125] E.M.A. Elbashbeshy, A.M. Sedki, Bioconvective Marangoni flow of unsteady MHD hybrid Casson nanofluid containing gyrotactic microorganisms over stretching surface through Forchheimer porous mecdium, Progress in Engineering Science, Volume 2, Issue 2, June 2025, 100074, https://doi.org/10.1016/j.pes.2025.100074

[126] S. M. Abo-Dahab, M. A. Abdelhafez, F. Mebarek-Oudina and S. M. Bilal, MHD Casson Nanofluid Flow over Nonlinearly Heated Porous Medium in presence of Extending Surface effect with Suction/Injection, Indian Journal of Physics, 95 (2021) 2703–2717, https://doi.org/10.1007/s12648-020-01923-z

[127] J. Jayaprakash, V. Govindan, Impacts of diffusion and chemical reaction on heat transfer in Casson nanofluids flow over a flat plate with accretion, Case Studies in Thermal Engineering, Volume 72, 2025, 106309, https://doi.org/10.1016/j.csite.2025.106309

[128] A. Ashique, U. Afzal, S. Abdal, S. Ullah, N. A. Shah, J. D. Chung, Optimization of thermal transfer in Casson hybrid nanofluids with magnetohydrodynamics and activation energy effects, Alexandria Engineering Journal, Volume 122, May 2025, Pages 255-267, https://doi.org/10.1016/j.aej.2025.02.067

[129] H. Vaidya, K. V. Prasad, F. Mebarek Oudina, R. Choudhari, and Neelufer, Solar-powered magnetoelectrokinetic peristaltic transport of thermally radiative Jeffery nanofluids in asymmetric porous media, CFD Simulation, 11 (2025) 289-318. https://doi.org/10.1515/9783111405094-011

[130] N. Elboughdiri, C. S. Reddy, A. Alshehri, S. M. Eldin, T. Muhammad, A. Wakif, A passive control approach for simulating thermally enhanced Jeffery nanofluid flows nearby a sucked impermeable surface subjected to buoyancy and Lorentz forces, Case Studies in Thermal Engineering, Volume 47, July 2023, 103106, https://doi.org/10.1016/j.csite.2023.103106

[131] T. Naseem, F. Mebarek-Oudina, H. Vaidya, N. Bibi, K. Ramesh, S. U. Khan, Numerical Analysis of Entropy Generation in Joule Heated Radiative Viscous Fluid Flow over a Permeable Radially Stretching Disk, CMES-Computer Modeling in Engineering & Sciences, 143(1), 351-371, 2025, https://doi.org/10.32604/cmes.2025.063196

[132] M. Bouselsal, F. Mebarek-Oudina, N. Biswas, A.I. Ismail, Heat Transfer Enhancement Using Al2O3 -MWCNT Hybrid-Nanofluid inside a Tube/Shell Heat Exchanger with Different Tube Shapes. Micromachines 14 (5), 1072 (2023). https://doi.org/10.3390/mi14051072

[133] Preeti, Ojjela, O., Kambhatla, P.K. & Mebarek-Oudina, F. Shape effect of MoS2 nanoparticles on entropy generation and heat transport in viscoelastic boundary layer flow. Pramana - J Phys 95, 182 (2021). https://doi.org/10.1007/s12043-021-02195-w

[134] Y. Badri, G. Dodd, J. Cater, A. Hall, G. Schmid, G. Emms, and E. Calius, Review of granular material damping and sound absorption for possible application in the sound insulation of lightweight floors, Journal of Building Engineering, 97, 110881 (2024). https://doi.org/10.1016/j.jobe.2024.110881.

[135] M. Innocentini, V. Salvini, A. Macedo, and V. Pandolfelli, Prediction of Ceramic Foams Permeability Using Ergun's Equation, Materials Research, 2, (1999).10.1590/S1516-14391999000400008.

[136] S. Ergun. Fluid flow through packed columns. 1952.

[137] M. Abbas, Modeling Of Porosity Equation For Water Flow Through Packed Bed Of Monosize Spherical Packing, Journal of Engineering and Sustainable Development, 15, (2011).

[138] P. Ranut, E. Nobile, and L. Mancini, High resolution microtomography-based CFD simulation of flow and heat transfer in aluminum metal foams, Applied Thermal Engineering, 69(1), 230-240 (2014). https://doi.org/10.1016/j.applthermaleng.2013.11.056.

[139] P. Ranut, E. Nobile, and L. Mancini, High resolution X-ray microtomography-based CFD simulation for the characterization of flow permeability and effective thermal conductivity of aluminum metal foams, Experimental Thermal and Fluid Science, 67, 30-36 (2015). https://doi.org/10.1016/j.expthermflusci.2014.10.018.

[140] J. A. Hamzah, and M. A. Nima, Experimental Study of Heat Transfer Enhancement in Double-Pipe Heat Exchanger Integrated with Metal Foam Fins, Arabian Journal for Science and Engineering, 45(7), 5153-5167 (2020).10.1007/s13369-020-04371-3.

[141] E. Pourfarzad, A. Behrangzade, E. Houshfar, and M. Ashjaee, Thermal and Fluid-Flow Characteristics of Silver-Water Nanofluid in a Metal-Foam Filled Channel, Heat Transfer Engineering, 42(21), 1827-1845 (2021).10.1080/01457632.2020.1826741.

[142] P. M. Kamath, C. Balaji, and S. P. Venkateshan, Convection heat transfer from aluminium and copper foams in a vertical channel – An experimental study, International Journal of Thermal Sciences, 64, 1-10 (2013). https://doi.org/10.1016/j.ijthermalsci.2012.08.015.

[143] K. Borakhade, and A. Mahalle. Enhanced Forced Convection Cooling of Power Electronics Devices Exposed to Hot Climatıc Conditions by Copper Metal Foam. in Techno-Societal 2018. 2020. Cham: Springer International Publishing.

[144] V. V. Calmidi, and R. L. Mahajan, Forced Convection in High Porosity Metal Foams, Journal of Heat Transfer, 122(3), 557-565 (2000).10.1115/1.1287793.

[145] K. Vafai, Convective flow and heat transfer in variable-porosity media, Journal of Fluid Mechanics, 147, 233-259 (1984). DOI: 10.1017/S002211208400207X.

[146] M. Ghaneifar, H. Arasteh, R. Mashayekhi, A. Rahbari, R. Babaei Mahani, and P. Talebizadehsardari, Thermohydraulic analysis of hybrid nanofluid in a multilayered copper foam heat sink employing local thermal non-equilibrium condition: Optimization of layers thickness, Applied Thermal Engineering, 181, 115961 (2020). https://doi.org/10.1016/j.applthermaleng.2020.115961.

[147] H. A. Nooruddin, and M. E. Hossain, Modified Kozeny–Carmen correlation for enhanced hydraulic flow unit characterization, Journal of Petroleum Science and Engineering, 80(1), 107-115 (2011). https://doi.org/10.1016/j.petrol.2011.11.003.

[148] M. J. MacDonald, C.-F. Chu, P. P. Guilloit, and K. M. Ng, A generalized Blake-Kozeny equation for multisized spherical particles, AIChE Journal, 37(10), 1583-1588 (1991). https://doi.org/10.1002/aic.690371016.

[149] L. Tadrist, M. Miscevic, O. Rahli, and F. Topin, About the use of fibrous materials in compact heat exchangers, Experimental Thermal and Fluid Science, 28(2), 193-199 (2004). https://doi.org/10.1016/S0894-1777(03)00039-6.

[150] N. M. Jasim, E. M. Fayyadh, and M. Razoki Hasan. Numerical Analysis to Study the Effect of Foam Thickness on The Thermal-Hydraulic Performance of The Metal Foam Heat Exchanger. in ICPER 2020. 2023. Singapore: Springer Nature Singapore.

[151] M. Fallah Barzoki, M. Rahmani, A. Shahabi Nejad, and A. Kasaeian, Investigating the thermal performance of different nanofluids in a metal foam tube under laminar flow regime, Journal of Thermal Analysis and Calorimetry, 148(22), 12947-12959 (2023).10.1007/s10973-023-12553-y.

[152] P. Du Plessis, A. Montillet, J. Comiti, and J. Legrand, Pressure drop prediction for flow through high porosity metallic foams, Chemical Engineering Science, 49(21), 3545-3553 (1994). https://doi.org/10.1016/0009-2509(94)00170-7.

[153] X. Yang, T. J. Lu, and T. Kim, An analytical model for permeability of isotropic porous media, Physics Letters A, 378(30), 2308-2311 (2014). https://doi.org/10.1016/j.physleta.2014.06.002.

[154] K. Ramesh, F. Mebarek-Oudina, B. Souayeh, Mathematical Modelling of Fluid Dynamics and Nanofluids, 1st edition, CRC Press (Taylor & Francis); 2023. https://doi.org/10.1201/9781003299608

[155] F. Mebarek-Oudina, H. Laouira, A. K. Hussein, M. Omri, A. Aissa, L. Kolsi and U. Biswal, Mixed Convection inside a Duct with an Open Trapezoidal Cavity Equipped with Two Discrete Heat Sources and Moving Walls, Mathematics, 10(6)(2022)929; https://doi.org/10.3390/math10060929

[156] H. Laouira, F. Mebarek-Oudina, H. Vaidya, Mixed convection assessment in an unusual cavity with a heat source opened to a horizontal channel, Mathematical Modelling of Fluid Dynamics and Nanofluids, CRC Press (Taylor & Francis), 1-10, 2023. https://doi.org/10.1201/9781003299608-1

[157] A. Mezaache, F. Mebarek-Oudina, H. Vaidya, and Y. Fouad, Heat transfer analysis of nanofluid flow with entropy generation in a corrugated heat exchanger channel partially filled with porous medium, Heat Transfer, Volume 53, Issue 8, pp. 4625-4647 (2024). https://doi.org/10.1002/htj.23149

[158] S. Mahmud, R.A. Fraser, Thermodynamic analysis of flow and heat transfer inside a channel filled with a porous medium, International Journal of Thermal Sciences, 41(11), 1011–1020 (2002). https://doi.org/10.1016/S1290-0729(02)01397-3

[159] A. Bejan (1996), Entropy Generation Minimization: The Method of Thermodynamic Optimization of Finite-Size Systems and Finite-Time Processes, CRC Press (1996).

[160] A.M. Al-Amiri, K.M. Khanafer, I. Pop (2009), Entropy generation due to heat and fluid flow in porous media. International Journal of Heat and Mass Transfer, 52(21-22), 5130–5140 (2009). https://doi.org/10.1016/j.ijheatmasstransfer.2009.04.023

[161] M. Nourani Zonouz (2012), Numerical analysis of flow field and heat transfer of 2D wavy ducts and optimization by entropy generation minimization method, Journal of Thermodynamics, 574596 (2012), https://doi.org/10.1155/2012/574596Wiley Online Library

AUTHOR'S PUBLICATIONS

International publications

- A. Mezaache, F. Mebarek-Oudina, H. Vaidya, and Y. Fouad, Heat transfer analysis of nanofluid flow with entropy generation in a corrugated heat exchanger channel partially filled with porous medium, Heat Transfer, Volume 53, Issue 8, pp. 4625-4647 **(2024)**. https://doi.org/10.1002/htj.23149
- A. Mezaache, F. Mebarek-Oudina, H. Vaidya, and K. Ramesh, Impact of nanofluids and porous structures on the thermal efficiency of wavy channel heat exchanger, International Journal of Thermal Sciences, 210, 109673 **(2025)**. https://doi.org/10.1016/j.ijthermalsci. 2024. 109673.

International communications

- A. Mezaache, F. Mebarek-Oudina, Heat transfer in fluid flow between parallel plates porous channel, International Conference on Energy and Material Sciences, EMS2022, University of Skikda, Algeria **(2022)**. doi: 10.13140/RG.2.2.22686.82246
- A. Mezaache, F. Mebarek-Oudina, Effect of wavy wall and metal foam insert on the thermal performance of channel heat exchanger, The Third International Conference on Materials, Energy & Environment, MEE'2025, April 21-22, **(2025**), El-Oued, Algeria. https://mee2025.sciencesconf.org/
- Abderrahmane Mezaache, Fateh Mebarek-Oudina, Thermal performance of channel heat exchanger filled with packed granular material, 1st International Conference on Engineering and Advanced Technologies, ICEAT 2025, April 27–29, **(2025)**, Mila, Algeria. https://sites.google.com/centre-univ-mila.dz/iceat2025
- Abderrahmane Mezaache, Fateh Mebarek-Oudina, Flow, Heat transfer and Entropy generation in a Wavy channel, International Scientific Conference on "Theoretical and Applied Problems of Convective Heat and Mass Transfer", **(2025)**.
- Abderrahmane Mezaache, Fateh Mebarek-Oudina, Comparative Analysis of Thermal Performance in Packed Granular and Foam Wavy Porous Channel Heat Exchangers, International Scientific Conference on "Theoretical and Applied Problems of Convective Heat and Mass Transfer", **(2025)**.

National communications

- A. Mezaache, F. Mebarek-Oudina, Hydrodynamic study of a wavy porous channel heat exchanger, The First National Conference on Mechanical Engineering NCME, University of Constantine 1, November, 6-7, (**2024)**. https://fac.umc.edu.dz/ista/NCME2024/ index.html
- A.Mezaache, F. Mebarek-Oudina, Thermal performance of wavy channel heat exchanger, National Conference on Green Energy, Boumerdes, Algeria, December, 15-16, (**2024)**. https://ncge.univ-boumerdes.dz/